

UC Irvine

UC Irvine Previously Published Works

Title

Interface chemistry of two-dimensional heterostructures – fundamentals to applications

Permalink

<https://escholarship.org/uc/item/3x3591fw>

Journal

Chemical Society Reviews, 50(7)

ISSN

0306-0012

Authors

Gbadamasi, Sharafadeen
Mohiuddin, Md
Krishnamurthi, Vaishnavi
[et al.](#)

Publication Date

2021-04-07

DOI

10.1039/d0cs01070g

Copyright Information





This work is made available under the terms of a Creative Commons Attribution License, available at <https://creativecommons.org/licenses/by/4.0/>

Peer reviewed



Cite this: *Chem. Soc. Rev.*, 2021, **50**, 4684

Interface chemistry of two-dimensional heterostructures – fundamentals to applications

Sharafadeen Gbadamasi,  †^{ab} Md Mohiuddin,  †^a Vaishnavi Krishnamurthi,^a Rajni Verma,^{ac} Muhammad Waqas Khan,^{ad} Saurabh Pathak,^{ae} Kourosh Kalantar-Zadeh  *^f and Nasir Mahmood  *^a

Two-dimensional heterostructures (2D HSs) have emerged as a new class of materials where dissimilar 2D materials are combined to synergise their advantages and alleviate shortcomings. Such a combination of dissimilar components into 2D HSs offers fascinating properties and intriguing functionalities attributed to the newly formed heterointerface of constituent components. Understanding the nature of the surface and the complex heterointerface of HSs at the atomic level is crucial for realising the desired properties, designing innovative 2D HSs, and ultimately unlocking their full potential for practical applications. Therefore, this review provides the recent progress in the field of 2D HSs with a focus on the discussion of the fundamentals and the chemistry of heterointerfaces based on van der Waals (vdW) and covalent interactions. It also explains the challenges associated with the scalable synthesis and introduces possible methodologies to produce large quantities with good control over the heterointerface. Subsequently, it highlights the specialised characterisation techniques to reveal the heterointerface formation, chemistry and nature. Afterwards, we give an overview of the role of 2D HSs in various emerging applications, particularly in high-power batteries, bifunctional catalysts, electronics, and sensors. In the end, we present conclusions with the possible solutions to the associated challenges with the heterointerfaces and potential opportunities that can be adopted for innovative applications.

Received 15th November 2020

DOI: 10.1039/d0cs01070g

rsc.li/chem-soc-rev

^a School of Engineering, RMIT University, Melbourne, Victoria 3001, Australia. E-mail: nasir.mahmood@rmit.edu.au

^b Petrochemicals and Allied Department, National Research Institute for Chemical Technology (NARICT), Basawa, Zaria, Kaduna State, Nigeria

^c School of Physics, The University of Melbourne, Parkville, Victoria 3010, Australia

^d Manufacturing, CSIRO, Clayton, Victoria 3168, Australia

^e Department of Mechanical Engineering, The University of Melbourne, Parkville, Victoria 3052, Australia

^f School of Chemical Engineering, University of New South Wales, Kensington, NSW 2033, Australia. E-mail: k.kalantar-zadeh@unsw.edu.au

† These authors contributed equally.



Sharafadeen Gbadamasi

Sharafadeen Gbadamasi obtained his BEng degree in Chemical Engineering in 2010 from Ahmadu Bello University, Nigeria. He obtained his MPhil degree in Chemical Engineering (Energy) from the University of Malaya, Malaysia, in 2016. He worked at NARICT, Nigeria, on several projects in the area of catalysis and applications before joining RMIT University, Australia, for his PhD degree in 2020 under the supervision of Dr Nasir Mahmood.

His research focuses on the synthesis of two-dimensional heterostructures for applications in electrochemical energy storage and conversion.



Md Mohiuddin

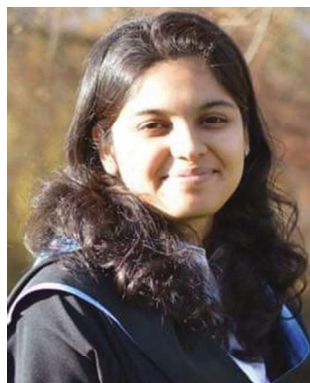
Md Mohiuddin received his PhD degree in 2020 from RMIT University, Australia. He obtained his MEng degree from Inha University, South Korea, in 2015 and BSc degree from Bangladesh University of Engineering and Technology, Bangladesh, in 2009. He is currently working as a Research Fellow at RMIT University, Australia. His current research interest is focused on the design and synthesis of two-dimensional materials and their applications in electronics, energy storage and conversion.

1. Introduction

The concept of two-dimensional heterostructures (2D HSs) arises when performance of currently available 2D materials reaches the limit. The incorporation of 2D HSs becomes inevitable to meet the requirements of future devices and systems, as different engineering strategies applied in tuning the structure, composition, and surface of 2D materials fail to attain the desired outcomes. In general, 2D HSs are formed by combining different 2D materials, and such combination provides a viable solution to overcome the intrinsic limitations of individual 2D materials while availing the unique characteristics of different components.^{1–3} When combined, the dissimilar 2D materials meet and interact intimately at a common boundary known as the ‘interface’, which we refer to herein as the ‘hetero-interface’.³ The interaction between the constituent 2D materials

at the heterointerface brings tremendous possibilities, as it not only creates new functional 2D materials but also enables unprecedented tailoring of material properties for practical applications.^{4–6} More specifically, the formation of heterointerfaces is remarkable, especially for atomically thin materials where electrons are exposed and consequently facilitate the band alignment,^{7,8} surface reconstruction,^{1,9} charge transfer and delocalisation between neighbouring materials,^{10–13} and enhance overall redox ability^{12,14} and ion storage.^{15–17} The heterointerface formed by the 2D materials in 2D HSs is often complex and remains poorly understood, even though the fundamental and applied research of 2D materials has made remarkable progress. Hence, an in-depth understanding of the fundamentals, formation, and factors affecting the heterointerface is crucial for the targeted applications.

Various types of heterointerfaces can be designed by integrating 2D materials with 2D materials or non-2D materials



Vaishnavi Krishnamurthi

Vaishnavi Krishnamurthi is a final year PhD candidate at RMIT University, Australia. Prior to her PhD candidature, she received her Master of Science (Nanoelectronics and nanotechnology) from the University of Southampton, England, and Bachelor of Engineering (Electrical and electronics) from Anna University, India. Her research work focuses on the synthesis of large area two-dimensional semiconductors for optoelectronic and neuromorphic applications.



Rajni Verma

Rajni Verma received her PhD in 2018 from the CSIR-National Physical Laboratory, India, for her research on synthesis and applications of various nanomaterials. As a postdoctoral researcher, she worked at Indian Institute of Technology Delhi in the area of metal–organic framework for photocatalytic applications. After that, she was awarded the prestigious McKenzie fellowship in 2019 and currently her research interest is focused on the nano-bio interface at the School of Physics, University of Melbourne, Australia.



Kourosh Kalantar-Zadeh

Kourosh Kalantar-Zadeh is a professor of Chemical Engineering at UNSW and one of the Australian Research Council Laureate Fellows of 2018. Prof. Kalantar-Zadeh is involved in research in the fields of materials sciences and sensors, has co-authored ~450 scientific papers and is also a member of the editorial boards of journals including ACS Sensors, ACS Applied Nano Materials, Advanced Materials Technologies, and ACS Nano. He has received many international awards including the 2017 IEEE Sensor Council Achievement, 2018 ACS Advances in Measurement Science Lectureship awards and 2020 Robert Boyle Prize of RSC. He has also appeared in the Clarivate Analytics most highly cited list since 2018.



Nasir Mahmood

Nasir Mahmood received his PhD from Peking University, China, in 2015. He worked at the University of Wollongong, Australia (2015–2016), and Tianjin University, China (2016–2017), as a research fellow and co-founded the Center of Micro–Nano Functional Materials and Devices, University of Electronic Science and Technology of China. Currently, he is working as a Vice-Chancellor Fellow at RMIT University, Australia. He has been awarded several international awards including “2018 Beijing Science and Technology Award”. He is also serving as an associate editor for Frontiers in Chemistry. Mahmood’s research interest includes the synthesis of nanomaterials and 2D heterostructures for electronics, catalysis, energy conversion and storage devices.

(*e.g.* 0D, 1D, 3D).^{2,18–20} However, 2D HSs (2D/2D) are the most demanding morphology for electronics,^{21,22} optoelectronics,^{23,24} catalysis,^{25,26} and energy storage^{17,27,28} due to the relatively large heterointerface contact. The heterointerface contact region of 2D HSs can either be in the vertical or lateral direction having either van der Waals (vdW) or covalent interactions.^{5,29–31} Heterointerfaces formed by face-to-face stacking of layers through manual stacking or epitaxial growth in the vertical direction are commonly known as vertical 2D HSs,^{10,30} whereas lateral 2D HSs are formed through the construction of heterointerfaces along the in-plane direction.^{32,33} Vertical 2D HSs formed by weak vdW force provide great flexibility in the synthesis process, sometimes without fulfilling the requirements of lattice matching.^{10,34} On the other hand, covalent cross-linking by chemical coupling of layers in the vertical direction is proven effective in creating ladder-like assemblies which are not possible in vdW 2D HSs.^{31,35,36} The large heterointerface contact area and tunable interlayer chemistry of vertical 2D HSs allow easy ion storage and transport,^{37,38} reduce the diffusion barrier,^{38,39} and improve conductivity¹⁶ to boost the electrochemical activity, especially for energy storage and conversions. Unlike vertical 2D HSs, lateral 2D HSs often offer easy modification of electronic properties owing to the gap-free heterointerface, but complications associated with the synthesis process and creation of perfect heterointerfaces are considered primary hurdles for the advancement of this type.^{33,40–42}

Irrespective of the type of 2D HSs, the quality of a heterointerface is predominantly driven by the synthesis procedure; hence the choice of synthesis methods is crucial depending on the targeted applications. Physical and direct growth synthesis techniques such as mechanical transfer,⁴³ chemical vapour deposition (CVD),⁴⁴ epitaxial growth,⁴⁵ and atomic layer deposition (ALD)⁴⁶ are suitable for large-scale electronic grade products but are restricted in terms of volume scale-up. Large quantities of 2D HSs are a prerequisite for energy storage and conversion applications; thus, strategies like electrostatic self-assembly,⁴⁷ layer-by-layer (LbL) assembly⁴⁸ and interface assisted growth⁴⁹ can be possible ways to meet the scalable demand. Hence, an in-depth understanding of the relationship between synthesis strategies and a heterointerface is imperative to develop integrated synthesis approaches for fine control over the chemistry of the heterointerface at large-scale. There have been several excellent reviews on 2D HSs,^{3,21,26,50,51} however, most efforts have been directed to either synthesis or applications of specific combinations of materials such as graphene-based 2D HSs. Moreover, most of these articles are missing the fundamental chemistry of heterointerfaces and suitable synthesis techniques for scalable production, which is the main driving force behind this review article.

This review article explains the chemistry of heterointerfaces, specialised characterisation, and recent progress in the synthesis and application of 2D HSs. Initially, we provide in brief the inherent limitations of 2D materials to answer the need for expanding into 2D HSs followed by the principles and chemistry of vdW and covalent heterointerfaces at the nano-scale. Afterward, the latest progress in the synthesis of 2D HSs

on a large-area as well as the possible scale-up methods with fine control over the heterointerface is introduced. Then, we emphasise the evaluation of the recent progress in technologies for high power energy storage, bifunctional catalysts, electronics, and sensors. Finally, the challenges associated with different synthesis techniques and suitable solutions that can be adopted to devise high-performing 2D HSs are proposed. We believe that an in-depth understanding of the nature and chemistry of a heterointerface will better expedite the quest for the exploration of efficient new 2D HSs.

2. Limitations of 2D materials

2D materials host a rich set of intriguing, unique properties which have proven promising for versatile applications such as electronics, optoelectronics, energy storage and conversion. The uniqueness of 2D materials is based on how they are arranged in their structure and whether they are composed of a single element, are binary in nature or are made of multiple elements. For example, graphene, silicene, borophene, antimonene, and black phosphorus (BP) consist of only one element, and therefore, mostly cause surface neutrality and instability; however, their patterned arrangement introduces several key characteristics which makes them promising over many other materials. On the other hand, binary 2D materials such as transition/post-transition metal chalcogenides, oxides, carbides, and nitrides (*e.g.* ZnO, MoS₂, GaN, Ti₃C₂, *etc.*) are amongst the most enriched and diversified class of 2D materials because of their unique structure composed of electropositive and electronegative elements, introducing properties which are generally missing in the single element-based 2D materials. Taking advantage of variable elements in the framework of 2D materials, a more complex class of 2D materials can be introduced, which are composed of multiple elements, *e.g.* MXenes. However, despite enormous opportunities and substantial progress, the requirements of basic thermodynamic stability of 2D materials limit their further modification, which imposed the emergence of 2D HSs.

Undoubtedly, the invention of various 2D materials has revolutionised many industrial sectors. However, individual 2D materials suffer from a certain degree of limitations due to their inherent properties, mainly originating from their thermodynamically satisfied basal plane atoms. Especially, these basal planes are considered neutral for electrochemical applications which then required further engineering and/or modifications.^{52,53} For example, despite high electrical conductivity, graphene demonstrates moderate charge storage and redox activity due to its surface neutrality.^{17,54} Besides, the absence of a suitable bandgap in graphene limits its use in bandgap electronics. Unlike graphene, a large portion of the 2D transition metal dichalcogenides (TMDs) and transition metal oxides (TMOs) offer tunable bandgaps which are favourable for electronic and optical devices.^{28,55–57} Furthermore, high redox activities due to layered structure,^{58,59} abundant active sites at the edges,^{28,60} short diffusion path and large surface area^{61,62} of these materials offer great benefits for energy storage and energy conversion. However, possible low

electrical conductivity, poor structural stability during large ion intercalation and de-intercalation/redox reactions, restacking possibilities and reduction of the active sites, in the long run, are considered major obstacles of 2D TMDs and TMOs.^{17,63}

The intrinsic limitations of 2D materials cannot be overcome on their own without any structural modifications. Occasionally, they can be mitigated by breaking their basal plane neutrality or enhancing the conductivity such as by surface functionalisation,^{64,65} doping,^{66,67} inducing defects,^{68,69} strains,^{70,71} and hybridisation.^{72,73} However, the reproducibility and precise control of these parameters remain challenging for a wide range of applications. In another convenient strategy, two or more dissimilar 2D materials can be integrated into one structure which is known as the 2D HS, and such integration forms a bridge between individual constituents through a heterointerface. For example, 2D HSs of MXenes/TMDs utilise the superior conductivity of MXenes and the high redox activity of TMDs, and therefore, they exhibit superior performance compared to MXenes or TMDs.³⁸ In 2D HSs, a heterointerface is considered the most important component, as it influences the enhancement of overall properties. Therefore, to attain the true benefits of 2D HSs, in-depth understanding of the nature and chemistry of the resultant heterointerface is a prerequisite, as explained in Section 3.

3. Chemistry of heterointerfaces in 2D HSs

It is well-known that 2D HSs can offer tunable heterointerfaces between layers of dissimilar 2D materials, enhanced charge carrier mobility, high specific surface area, electron-hole (e^-h^+) pair separation, low power consumption, quick mass transport and fine-tuning of properties for prospective applications. However, limited understanding of heterointerface chemistry, especially, when dissimilar atoms are strongly bonded in a different environment at heterointerfaces, limits the actual engineering and full utilisation of such structures for various applications.

3.1 van der Waals heterointerface

The vdW 2D HSs are constructed *via* vdW forces such as dipole-dipole, dipole-induced dipole and instantaneous dipole-induced dipole interactions due to the interplanar interaction among basal or edge planes.^{50,74} The vdW 2D HSs offer high anisotropy between the vertical (out-of-plane) and lateral (in-plane) directions,³ and are free of the requirement of exact lattice matching and processing compatibility.^{50,74-77} In fact, the lattice mismatch or rotation angle difference of 2D HSs produces Moiré patterns, which help in tuning the local structural and electronic properties.^{78,79} However, for the stable stacked vdW 2D HSs the lattice mismatch should be <5% (without any instability like polycrystalline phase creation).⁸⁰ Moreover, large mismatch often leads to misfit dislocations at the heterointerface and beyond, which are good for ionic conduction but can impede the electronic properties of 2D HSs. The vdW interactions at the heterointerface is a low energy integration method which does not require strong face-to-face chemical

bonds, thus eliminating chemical processing.⁷⁴ Moreover, free assembly of different 2D sheets in vertical vdW 2D HSs allows large tunable interlayer spacing that makes these 2D HSs unique with enhanced features, especially for mass transport.

In-depth knowledge of physics behind the heterointerface can help in understanding the mechanism of improving/introducing new properties. For example, interface coupling between two dissimilar layers results in band alignment or work function, as suggested by Anderson (semiconductor-semiconductor heterointerface, S-S) or Schottky-Mott (Metal-Semiconductor heterointerface, M-S) rules.⁸¹⁻⁸³ To explore the changes that occur at heterointerfaces, the understanding of electronic band structures of S-S and M-S heterointerfaces is crucial. The band alignments of S-S heterointerfaces are classified into three types: type-I straddling gap (Fig. 1a), type-II staggered gap (Fig. 1b) and type-III broken gap (Fig. 1c) at the heterointerfaces.^{84,85} In type-I, the valence band (VB) and conduction band (CB) of material S2 lie in between the bands of material S1 leading to hole and electron accumulation and transfer towards the VB and CB of material S2.⁸⁶ The fast recombination of holes and electrons in this type indicates the capability towards luminescent devices like light-emitting diodes.⁸⁷ In type-II, the CB and VB of material S1 are at higher levels as compared to the corresponding bands of material S2. In this type, the tendency of electron transfer is towards material S2 and the hole accumulation is towards material S1.⁸⁸ The effective spatial charge separation and modulation of the transition energy at the heterointerface due to different work functions allow extended time for interlayer optical excitons in type-II configuration, making it a good option for electron-hole separators and optoelectronic devices.^{84,89,90} The type-I and type-II heterointerfaces also offer the possibility to modify the redox power of active sites even at zero bias.⁸⁵ In type-III, the VB and CB of material S1 are higher than the CB of material S2, and also lack the space charge zone.⁸⁵ The high-speed transfer of holes and electrons in different layers of type-III 2D HSs creates a strong electric field due to the semi-metallic behaviour at the heterointerface, thus making them a perfect candidate for photovoltaic cells.⁸⁴ Hence, by constructing heterointerfaces carefully, a set of new materials can be designed based on their band alignment for various applications. Moreover, adding dopants at a heterointerface or combining different semiconductors introduces a unique p-n junction (Fig. 1d), with an interfacial potential difference even in the absence of an external bias.⁸⁵ Furthermore, the M-S heterointerfaces can also be developed among the p or n-type semiconductors and metal or semi-metals,^{21,91} where the electron flow and electronic interaction are influenced by the Schottky effect at the heterointerface. The electron flow induces a change in the Fermi level and electron density and hence increases the chemical reactivity of the M-S heterointerfaces (Fig. 1e and f).⁹¹⁻⁹³

2D HSs not only help in electronic coupling but also tune the electron transfer at the heterointerface through an appropriate combination of materials.^{85,94} For example, in the C_3N_4/MoS_2 2D HS, C_3N_4 has a higher Fermi level position and a low energy barrier for migration of electrons from C_3N_4 to MoS_2 , which promotes the flow of charges to achieve conductive 2D HSs.⁹⁴

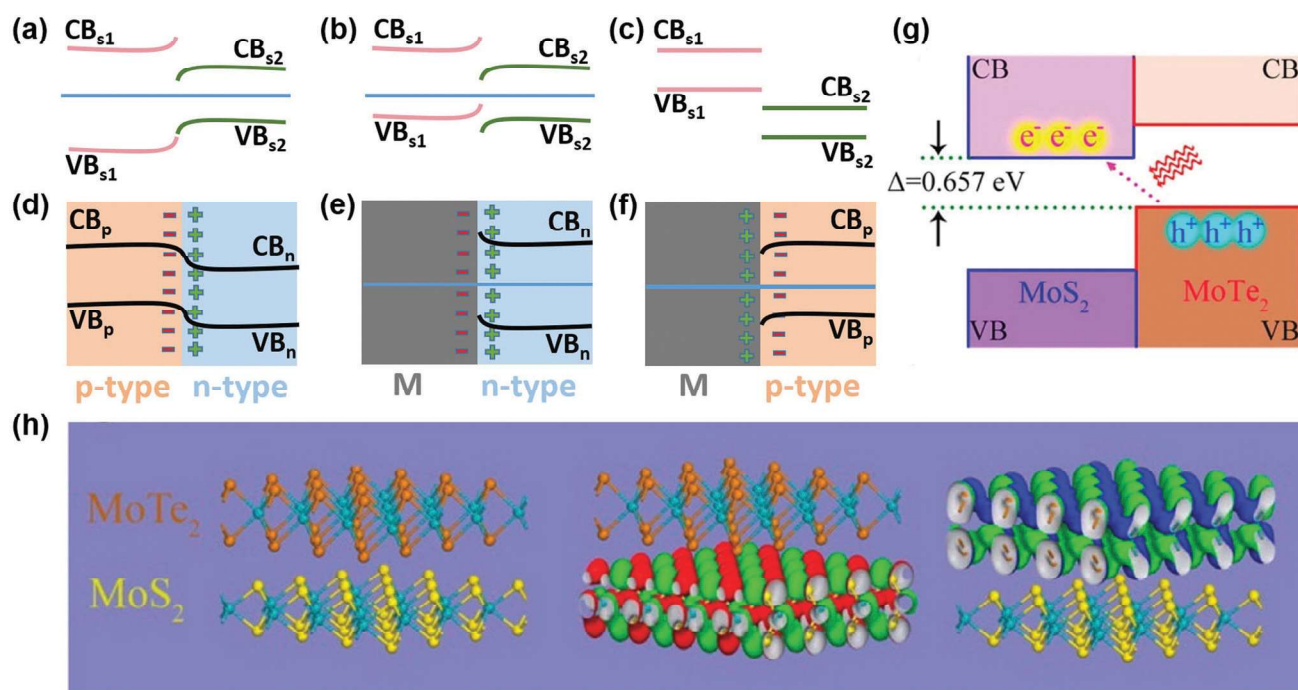


Fig. 1 (a–f) Schematic illustration of electronic band structures of typical S–S heterointerfaces and M–S heterointerfaces. (g) Schematic illustrations of type-II interband excitation processes in MoTe₂/MoS₂ vdW 2D HSs. The value of the inter bandgap (Δ) is obtained by theoretical calculations. (h) The cross-sectional view of the atomic structures and the calculated bonding charge densities of MoTe₂/MoS₂ 2D HSs. The orange, yellow, and blue spheres represent Te, S, and Mo, respectively. Red/green and blue/green represent the distributions of negative and positive charges, respectively. (g and h) Reproduced with permission from ref. 89, copyrights reserved to American Chemical Society 2016.

Similarly, the coupling strength at the heterointerface can influence the charge transfer exciton dynamics as well and provide photoluminescence (PL) characteristics to 2D HSs. Interestingly exciton dynamics and PL characteristics can be further tuned by inserting dielectric layers at the heterointerface. For example, creating a heterointerface between MoS₂ and WSe₂, reduces the PL response of HS significantly compared to the individual materials.⁹⁵ Such a change occurs because of the recombination process of charge transfer excitons, which couple the electrons of MoS₂ and holes of WSe₂ in their CB and VB, respectively.⁹⁵ On the other hand, the introduction of various layers ($N = 0, 1, 2, 3$) of h-BN weakens the newly emerged PL peak showing its dependency on the heterointerface of MoS₂/WSe₂ and tuning of the bandgap with the assistance of dielectric materials. Likewise, 2D MoS₂ and MoTe₂ individually have a cut-off wavelength of 700 nm and 1200 nm, respectively, and with the creation of a heterointerface among them a bandgap of about ~ 0.66 eV (~ 1880 nm) can be observed between the VB maximum of MoTe₂ and the CB minimum of MoS₂. Interlayer coupling and injection of electrons from MoTe₂ to MoS₂ lower the work function with charge separation. Thus, the interlayer coupling permits the 2D HS to exhibit transition between the VB (MoTe₂) and the CB (MoS₂) in the infrared region beyond 1200 nm (Fig. 1g).⁸⁹ Here the density functional theory (DFT) demonstrates that the localised electrons are present in MoS₂ and holes in MoTe₂, inducing charge separation at the heterointerface (Fig. 1h).

The vdW interactions can tune the adsorption energies at the heterointerface, thus decreasing the diffusion barrier for ions,

and allow multilayer adsorption of ions with slight or no expansion for superior cycling stability.⁵⁰ In fact, the weak vdW interactions between the basal planes allow energetically stable 2D HSs with a tunable interlayer distance to ensure the rapid diffusion of ions, even for the larger ionic radius ions (Na⁺ and K⁺) and polarised ions (Mg²⁺).^{39,50,96} These properties of vdW 2D HSs can further be tuned in the presence of different functional groups and by the stacking order of individual sheets. In the case of MXene/G-based 2D HSs, the first-principles investigations indicated that the intercalation of the alkali metal ions is energetically favourable and thermally stable in V₂CO₂/G and Ti₂CO₂/G (having O terminated) but not in Sc₂C(OH)₂/G (having OH terminated).⁹⁷ This is because Sc₂C(OH)₂/G shows a positive or very small binding energy value per alkali atom. Thus, tuning the surface chemistry at the heterointerface made such 2D HSs highly functional for energy storage applications and can reduce the diffusion energy barrier to almost half compared to that of the bilayer MXenes.

Moreover, vertical stacking of dissimilar sheets provides opportunities for different structural arrangements having variable lattice mismatch. For example, there are three stacking possibilities of GeSe/BP: (i) Ge or Se atom above the centre of the BP hexagon (Fig. 2a), (ii) both the monolayers are perfectly on each other (Fig. 2b) and (iii) Ge or Se atom located above the centre-point of the P–P bond (Fig. 2c).⁹⁸ The structural optimisation disclosed that among these different structures, structure (i) is the most stable pattern for the stacking of GeSe over BP as the total energy is 0.028 eV, which is 0.029 eV lower compared to other

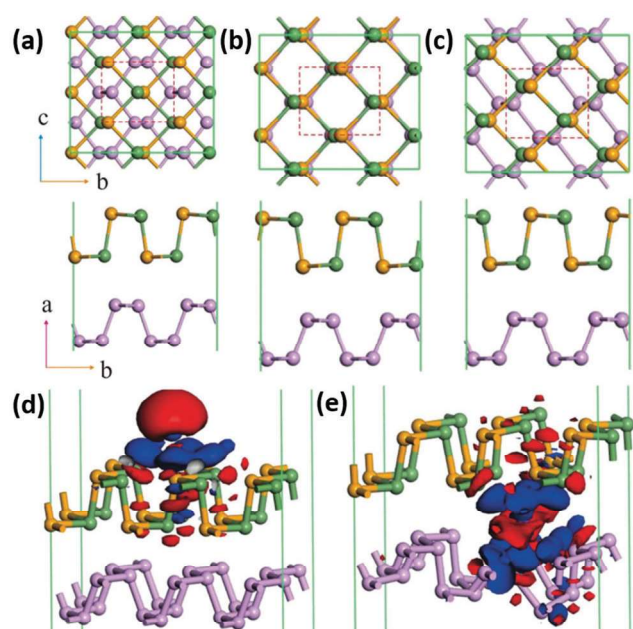


Fig. 2 Top and side views of the three non-equivalent stacking patterns of the GeSe/BP interface. (a) Ge or Se atom above the centre of the BP hexagon, (b) both the monolayers are perfectly on each other and (c) Ge or Se atom located above the centre-point of the P–P bond present in BP. Differential charge densities of K adsorbed (d) on the surface and (e) in the interlayer of GeSe/BP. Blue and red colours indicate electron accumulation and depletion, respectively. Reproduced with permission from ref. 98, copyrights reserved to American Chemical Society 2019.

possible stackings, shown in Fig. 2b and c, respectively. The lattice mismatch in structure (i) is $\sim 5\%$; however, the binding energy value of -0.346 eV ensures a stable structure accredited to the flexible puckered design of the monolayers of GeSe and BP.⁹⁹ Further, the adsorption of K atoms was found to be identical on the surface (K/GeSe/BP) and between the layers (GeSe/K/BP) of 2D HSs, as presented in Fig. 2d and e.⁹⁸

Fig. 2d shows the gain and loss of electronic charge on the adjacent layers of GeSe and K atoms for the K/GeSe/BP system because of the electronegative difference between the Ge and K atoms; consequently, ionic bonds are formed in the system. In contrast, there is no electron accumulation on the BP layer due to the long distance from K atoms. Fig. 2e illustrates the transfer of electrons from K atoms to both Ge and P atoms in the case of GeSe/K/BP because of electronegativity difference which results in a stronger ionic bond compared to the K/GeSe/BP system. In the case of GeSe/BP, the state close to the Fermi level is flat having a slightly lesser indirect bandgap (0.347 eV) as compared to GeSe (1.100 eV) and BP (1.042 eV), which ensures high conductivity. Further, with the adsorption of K atoms (potassiation process), there is no bandgap in the 2D HS showing the successful conversion of the system from semi-conducting to metallic. Similar phenomena are also observed in the case of the MoS₂/G 2D HS after the lithiation process, which witnesses the advantages of constructing heterointerfaces.¹⁰⁰

Besides band modulation, controlling the number of layers and interlayer spacing can also boost electron and ion transport,

leading to improved electrochemical performance.^{77,101} The large interlayer spacing allows direct electrolyte penetration at the heterointerface; thus, ions only need to diffuse in close proximity or a few Å distance.¹⁷ The interlayer spacing can be tuned in 2D HSs, and different interlayer distances can be achieved as compared to pristine 2D layered materials, which can facilitate the diffusion of even large radii ions to develop energy storage systems beyond the lithium technology. For example, the interlayer distance in nitrogen-doped G/MoS₂ is 0.99 nm whereas the pure MoS₂ interlayer distance is 0.62 nm demonstrating the better chance of diffusion of ions in the case of 2D HSs, where even Na⁺ and K⁺ can diffuse easily.¹⁰² Further, an optimised volume change can be achieved by selecting 2D materials having opposite volume changing behaviours in 2D HSs and/or by constructing pillared 2D HSs to increase the electrode life.

In summary, vdW 2D HSs provide great flexibility in choosing any desired combination of materials to harvest the interface-induced new physical and chemical features as they do not require exact lattice matching to produce the integrated 2D HSs. The high-quality dangling bond free 2D surfaces can be attained without complex experimental processes and expensive methodologies in vdW 2D HSs; thus, vdW 2D HSs are more popular for electronics and optoelectronics applications. Although with heterointerface engineering, 2D HSs show superior electrochemical properties as compared to their individual counterparts, there are certain limitations. Moreover, the credibility and stability of these 2D HSs, due to weak physical interactions and charge transfer, are still challenging and suggest the construction of 2D HSs with strong chemical bonds to attain more stable structures, fast charge transport and a controlled interlayer gap like covalent 2D HSs, which are discussed in the following section.

3.2 Covalent heterointerface

Certain limitations of vdW heterointerfaces and the requirement of high structural stability along with tunable characteristics at heterointerfaces for enhanced performance gave birth to a new class of 2D HSs which are covalently bonded. For instance, a direct covalent bond through Ti–O–N in TiO₂/g-C₃N₄ facilitates ultrafast electron migration and separation of charge carriers through band bending while vdW forces cause no significant change in the bandgap.¹⁰³ The covalent connections can occur directly or with the assistance of a linker between dissimilar materials like EDC (1-ethyl-3-(3-dimethylaminopropyl) carbodiimide) and Sonogashira couplings to develop a stable structure.³¹ Such strong and direct connections not only hold the different materials together, even under harsh conditions, but also allow the ultrafast flow of charges using covalent bonds as direct highways between two materials.

Normally, the 2D materials are free of dangling bonds or have clean interfaces, so require linkers to develop covalently bonded 2D HSs. Fortunately, covalent 2D HSs with the assistance of linkers do not require any lattice matching; thus, they provide great flexibility in choosing any combination of materials to construct 2D HSs. Such modifications can extend their applications to various fields beyond electronics like photo- and electrochemical energy

conversion and storage. However, difficulty in attaining well-controlled covalently bonded 2D HSs limits the understanding of the role of heterointerfaces in improving various material characteristics. Therefore, the findings from theoretical studies have been used to understand the role of heterointerfaces and selection of materials of various combinations. For example, the wave function plots of covalently linked C_3N_4/MoS_2 (Fig. 3a) and $C_3N_4/N-rGO$ (nitrogen-doped reduced graphene oxide) (Fig. 3b) were obtained through the EDC coupling by calculating the energy orbitals of the cross-linked 2D HSs using DFT.¹⁰⁴

The wave function plot of the $C_3N_4/N-rGO$ 2D HS displayed the possibility of the transfer of the charge from the highest occupied molecular orbital (HOMO) on N-rGO towards the lowest unoccupied molecular orbital (LUMO+1) on C_3N_4 . On the other hand, in the case of C_3N_4/MoS_2 , the possibility of charge transfer was from the HOMO-3 on C_3N_4 to the LUMO on MoS_2 . It was found that the charge transfer took place *via* space and bonds among the covalently cross-linked heterointerfaces.

Further, cross-linking also produces planarity, which contributes to effective charge transfer in 2D HSs, owing to orbital overlapping.¹⁰⁴ Owing to photo-induced charge transfer upon photoexcitation, electrons are transferred from the higher energy LUMO of C_3N_4 to the LUMO of N-rGO or MoS_2 . Though the formation of 2D HSs is expected to bring about new properties, it should be noted that not every combination of two different materials will bring advancement in the field. For example, electron transfer is boosted when C_3N_4 is combined with N-rGO or MoS_2 . However, when using both 2D HSs as the catalyst for hydrogen evolution reaction (HER), $C_3N_4/N-rGO$ did not show a good performance like C_3N_4/MoS_2 as electron transfer in $C_3N_4/N-rGO$ does not play any role in HER because the CB minima of N-rGO is below the water reduction potential.¹⁰⁴

The covalent linkages at heterointerfaces not only help in improving the charge transfer (to the catalytic sites) between heterointerfaces but also offer a large interfacial surface area to speed up the electrochemical reactions.³⁵ Besides simply tuning the charge movements, functionalisation of 2D materials to construct covalently bonded 2D HSs creates defects which entirely change the properties of the resultant 2D HSs. For example, in the synthesis of covalently bonded rGO and MoS_2 composites through Sonogashira coupling, iodobenzene functionalised MoS_2 shows the transition from 1T \rightarrow 2H due to defect creation (Fig. 3c).³⁶ This, entirely changes the characteristics of MoS_2 in 2D HSs and makes it functional for various applications. Moreover, covalent pillaring between MoS_2 and rGO provides the opportunity to control the interlayer distance and results in a porous structure with a large pore volume, along with improved functionality attributed to the defects of MoS_2 and π -electron cloud due to aromatic molecules between the layers.³⁶ The selection of materials and the type of linkers such as linkers with a conjugated system that can work as a metallic bond is very crucial to develop beneficial heterointerfaces for any targeted application.¹⁰⁵

As discussed above the type and the length of the linker can induce different functionalities; thus, the availability of a variety of functional groups opens great opportunity to develop 2D HSs with large versatility.¹⁰⁵ For example, to enhance the performance of batteries and extend their life, strong covalent connections with long linkers can be highly useful to stabilise the structure with large interlayer spaces. Hence, it allows quick storage by direct penetration of the electrolyte into the layers of 2D HSs where ions can simply become stored over the surface of each sheet. Moreover, incorporating redox-active linkers increases the number of active sites and charge transfer can

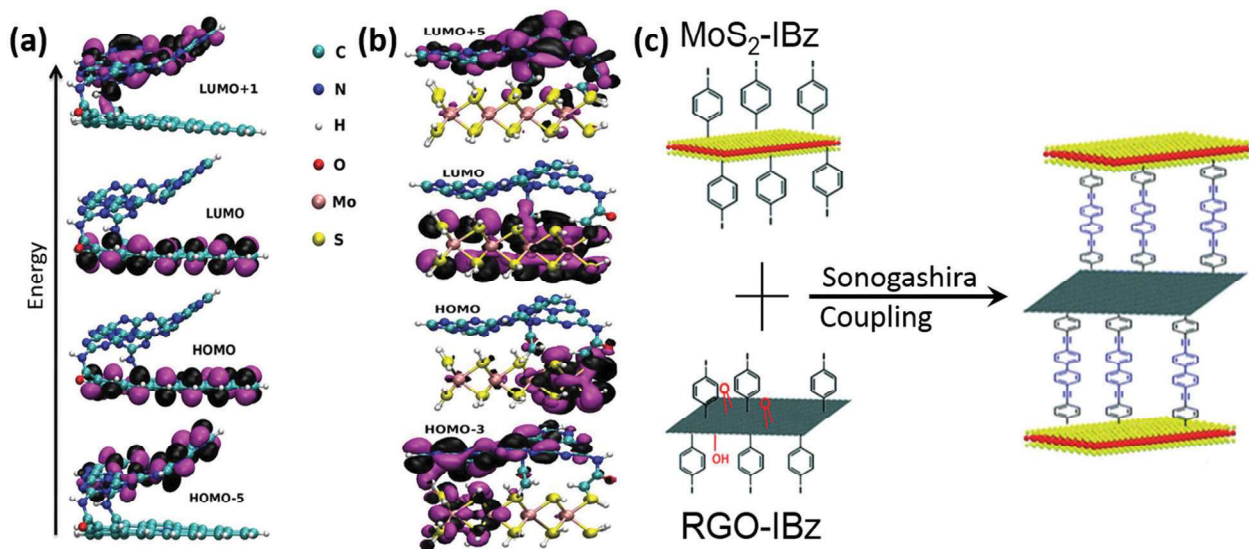


Fig. 3 Wave function plots of (a) $C_3N_4/N-rGO$ and (b) C_3N_4/MoS_2 , where the upper layer is C_3N_4 for both the cases (interlayer spacings in $C_3N_4/N-rGO$ and C_3N_4/MoS_2 are 0.30 and 0.73 nm, respectively, which are comparable with the experimentally observed values). Reproduced with permission from ref. 104, copyrights reserved to American Chemical Society 2017. (c) Synthesis of covalently bonded MoS_2/rGO through Sonogashira coupling. Diazotisation of MoS_2 and rGO with the 4-iodobenzenediazonium chloride salt formed iodobenzene (IBz) functionalised MoS_2 and rGO which ultimately enabled the construction of MoS_2/rGO assemblies. Reproduced with permission from ref. 36, copyrights reserved to Royal Society of Chemistry 2016.

be further manipulated, which is difficult to achieve in traditional vdW 2D HSs. But keep in mind that the increase in the length of the interlayer distance by longer linkers is always not a guarantee for improvement in the properties such as improved charge transfer within 2D HSs. For example, the hydrogen evolution activity of covalently linked 2D HSs decreases with the increase of interlayer separation.¹⁰⁶ In fact, the charge distribution with the increase in the linker length starts confining near the contact and decreases from the heterointerface to reduce the charge flow. This can be tuned by having different electronegativity atoms in the linker; however, more experimental and theoretical efforts are needed to understand their mechanism of action.

4. Synthesis of 2D heterostructures

The synthesis of 2D HSs is achieved by the rational design of the assembled 2D materials in an oriented heterointerface of specific order with notable differences from the random mixing of 2D materials.^{107,108} 2D HSs provide an opportunity to combine the desired properties of individual 2D materials while eradicating their inadequacies. The qualities of 2D HSs like the layer number, degree of defect, interlayer spacing and uniformity of the heterointerface significantly affect their properties.⁵¹ Different methods are implemented for the synthesis of 2D HSs, but the majority of them are restricted only to the small area/volume synthesis.^{109,110} Large-scale synthesis of 2D HSs poses a significant challenge as the stacking up of 2D monolayers in vertical assemblies into rationally engineered complex multilayer systems is not straightforward.⁵¹ Therefore, the major challenge in the material to device transition remains the requirement of large-scale production of 2D HSs.²¹

The assembly strategies of 2D heterointerfaces have been extended to design individual 2D monolayers in vertically stacked 2D HSs by physical and chemical means.¹¹¹ The conventional synthesis methods of 2D HSs involving physical methods such as mechanical transfer are limited to only several monolayers due to microscopic impurities and residues on the exposed surfaces.¹¹² On the other hand, direct growth techniques such as CVD,¹¹³ molecular beam epitaxy (MBE),¹¹⁴ ALD,¹¹⁵ hydro-/solvo-thermal synthesis¹¹¹ and electrochemical deposition (ECD)¹¹⁶ provide adequate control over the heterointerface, but are restricted due to low volume production. To overcome these challenges, new hybrid synthesis techniques are proposed like electrostatic self-assembly,¹¹⁷ LbL deposition/growth,¹¹⁸ and interface-assisted synthesis¹¹⁹ which can potentially overcome the challenges posed by the conventional methods and can be used satisfactorily for large-volume fabrication of 2D HSs.

One key component that contributes to the exceptional properties of 2D HSs is the nature of the heterointerface and the type of interactions (vdW or covalent).³ Owing to the absence of dangling bonds in most 2D materials, creation of covalent bonds has been a major challenge; thus, most of the focus has been towards vdW 2D HSs.¹²⁰ However, covalent functionalisation of individual layers in 2D HSs can be attained by the introduction of ligands at the edge or basal plane defects. Covalent functionalisation typically causes more significant perturbation to the properties of 2D HSs

compared to vdW one.¹²¹ In addition, vdW 2D HSs grown heteroepitaxially are highly dependent on the substrate crystal structure and orientation.¹²² Thus, surface tension and strain strongly impact the properties of vdW 2D HSs grown by heteroepitaxial deposition mode (*e.g.* Stranski-Krastonov).¹²³ Therefore, introducing covalent functionalisation between the layered materials and/or substrate can potentially help in obtaining high quality 2D HSs.

Heterointerface engineering at the entire basal plane still remains a challenge.¹¹⁰ In addition, current synthesis strategies are limited to the stacking of just a few sheets as vdW 2D HSs result in heteroepitaxial growth for the large-scale fabrication due to the absence of any strong interaction between the layers and covalently bonded HSs are restricted due to the severe lattice mismatch condition or otherwise required linkers. This limits the potential scaling-up of 2D HSs for commercial applications. The integrated synthesis approaches have possibilities to be scaled-up with fine control over the chemistry of heterointerfaces which will be explained in this section. In the rest of this discussion, the focus will be given to the scalability of proposed techniques with their advantages, bottlenecks and shortcomings. Also, we will emphasise the surface functionalisation and bonding between the individual 2D layers. Moreover, we will discuss covalently bonded 2D HSs on entire basal plane epitaxial interfaces, along with the vdW 2D HSs that can be deposited by each of the proposed techniques.

Note: Mechanical transfer methods are one of the most conventional techniques for the fabrication of 2D HSs that involve the mechanical transfer of arbitrary 2D nanosheets onto a substrate one by one. This technique is most straightforward for the fabrication of vdW 2D HSs as most of the layered materials can be mechanically exfoliated from their bulk crystals. Direct mechanical assembly is a facile technique to attain high-quality vdW HSs at the laboratory scale with a controlled stacking order that typically involves mechanical exfoliation of a 2D crystal followed by vertically stacking it on another 2D layer. Even though it is important for fundamental research, this technique is not further discussed here, due to its low yield.

4.1 Chemical vapour deposition

CVD is a powerful method to fabricate high-quality large-area 2D HSs with better control over the number of layers. For example, by employing low-pressure CVD (LPCVD) MoS₂ can be grown on top of graphene sheets in a stacked manner to achieve vertical 2D HSs as shown in Fig. 4a.¹¹³ The heterointerface produced by LPCVD is atomically clean with better properties than mechanically transferred layers, thus highlighting the advantages of this method in producing high-quality 2D HSs. The emergence of new properties at the heterointerface has resulted in a huge interest in developing a variety of 2D HSs utilising the CVD approach.³⁰ However, the cleavage-and-transfer method of as-grown layers through the conventional CVD approach results in unwanted cracks, wrinkles and interfacial contamination.

Considering these demerits, a direct synthesis approach was introduced for the growth of 2D HSs of MoS₂/WSe₂ and WSe₂/MoSe₂ on graphene through the combination of oxide powder

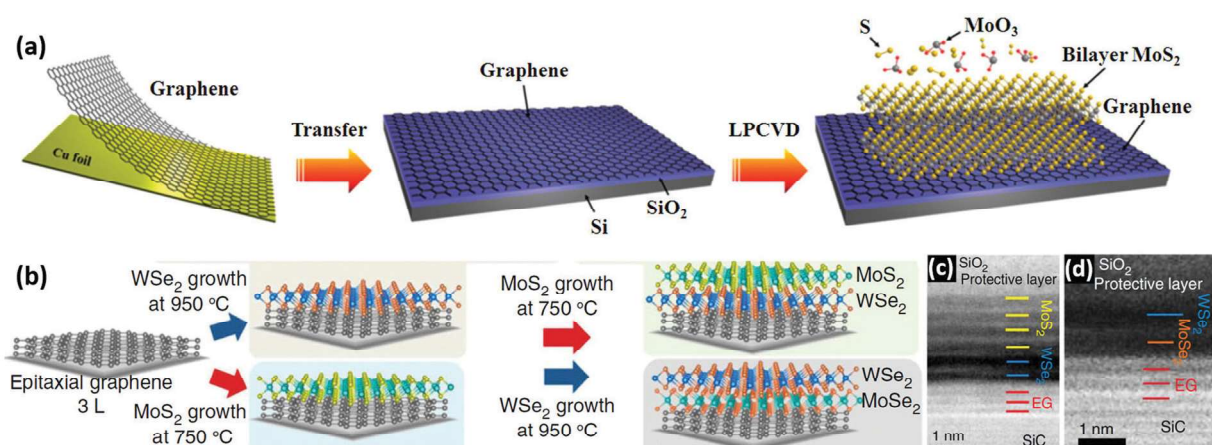


Fig. 4 (a) Schematic illustration of the synthesis of the MoS₂/G HS by growing MoS₂ on graphene. Reproduced with permission from ref. 113, copyrights reserved to American Chemical Society 2016. (b) The synthesis process of MoS₂/WSe₂ and WSe₂/MoSe₂ vdW HSs on the epitaxial graphene substrate. The cross-section STEM of MoS₂/WSe₂ and WSe₂/MoSe₂ shown in (c) and (d), respectively confirms that the stacked structures exhibit perfect heterointerfaces, with no intermixing of Mo–W or S–Se after synthesis. Reproduced with permission from ref. 124 copyrights reserved to Springer Nature 2015.

vaporisation and metal–organic chemical vapour deposition (MOCVD).¹²⁴ By controlling the growth temperature and other parameters, alternative layers of MoS₂ and WSe₂ or MoSe₂ and WSe₂ can be designed in vertical 2D HSs as shown in Fig. 4b.¹²⁴ The formation of high-quality heterointerfaces was confirmed by scanning transmission electron microscopy (STEM) analysis (Fig. 4c and d). The nucleation and interfacial reaction phenomena to construct 2D HSs in CVD can be controlled and modified through tuning the various growth parameters such as temperature, pressure, nature of the substrate and the gas flow rate.^{125,126} For example, highly crystalline and atomically sharp WS₂/MoS₂ HSs with vertical and lateral heterointerfaces were synthesised using the vapour phase growth process by simply varying the growth temperature.³⁰ The formation of MoS₂ occurred first at a low temperature of 650 °C, followed by nucleation and growth of WS₂ because of the low vapour pressure of W between 650 and 850 °C. The difference in the nucleation and growth rates produced MoS₂ and WS₂ in the form of vertically stacked bilayers at a precise reaction temperature of 850 °C and the lateral HS at 650 °C.

Furthermore, controlling carrier gas composition and flow can also play an important role in constructing the desired heterointerface. For example, Sahoo *et al.* proposed the use of two different carrier gases, *i.e.* N₂ + H₂O_(g) and Ar + H₂ (5%), to construct the 2D HSs of MoX₂/WX₂ (X: S, Se), where N₂ + H₂O_(g) helps the growth of MoX₂ and Ar + H₂ (5%) promotes the growth of WX₂, and by switching carrier gases back and forth cyclically, a 2D HS can be generated.¹²⁶ Simply, N₂ + H₂O_(g) allows evaporation of oxides and hydroxides of both Mo and W precursors, while the volatile nature of gaseous W precursors allows only the deposition of Mo precursors. On suddenly switching the carrier gas to Ar + H_{2(g)}, the supply of the Mo precursor reduces while the deposition of the existing volatile W precursor leads to the formation of WX₂. This method provides continuous growth of TMD-based 2D HSs with multi-heterointerfaces. The formation of several heterointerfaces is

controlled by the number of switching cycles, and the lateral size of each domain depends on the growth time of each cycle; thus, by controlling these factors the desired size of 2D HSs can be obtained.

The substrate also plays a key role in producing 2D HSs in this method. For example, the nature of Bi₂Te₃/Sb₂Te₃ heterointerfaces changes significantly by varying the substrate from SiO₂/Si to h-BN.¹²⁷ In the case of the SiO₂/Si substrate, Bi₂Te₃/Sb₂Te₃ grows into a triangular geometry where Bi₂Te₃ grows first followed by the nucleation of Sb₂Te₃ layers at the edge of Bi₂Te₃. On the h-BN substrate, growth of Bi₂Te₃/Sb₂Te₃ is propagated in a layer-by-layer fashion. The effect of diffusion, surface roughness and dangling bonds was mentioned as the reason for variation in their morphologies on changing the substrate. Thus, we believe that by controlling the aforementioned parameters, a well-controlled heterointerface can be produced on a large scale.

4.2 Atomic layer deposition

Compared to CVD, ALD techniques offer more control over thickness at the atomic level.^{128,129} ALD comprises of successive alternating pulses of precursors in the gaseous form which react with the substrate, and each of these gas-surface reactions is referred to as a half-reaction.¹²⁹ Each half-reaction includes purging of the precursor pulse in the vacuum chamber for a specified time that allows the precursor to completely react with the substrate surface as illustrated in Fig. 5.^{115,129} The thickness of the film is controlled by the number of ALD cycles. Usually, the ALD growth is carried out in a modest temperature range which is one of the major advantages of this method.^{130,131} Further, the self-saturating reaction mechanism of this method allows control over the growth of the film at the atomic level with excellent conformality.¹²⁹

A wide range of 2D HSs have been grown by ALD; for instance, Ga₂O₃/WO₃ 2D vdW HSs have been grown by ALD at the wafer-scale in the thickness range below 10 nm with 1.5 nm

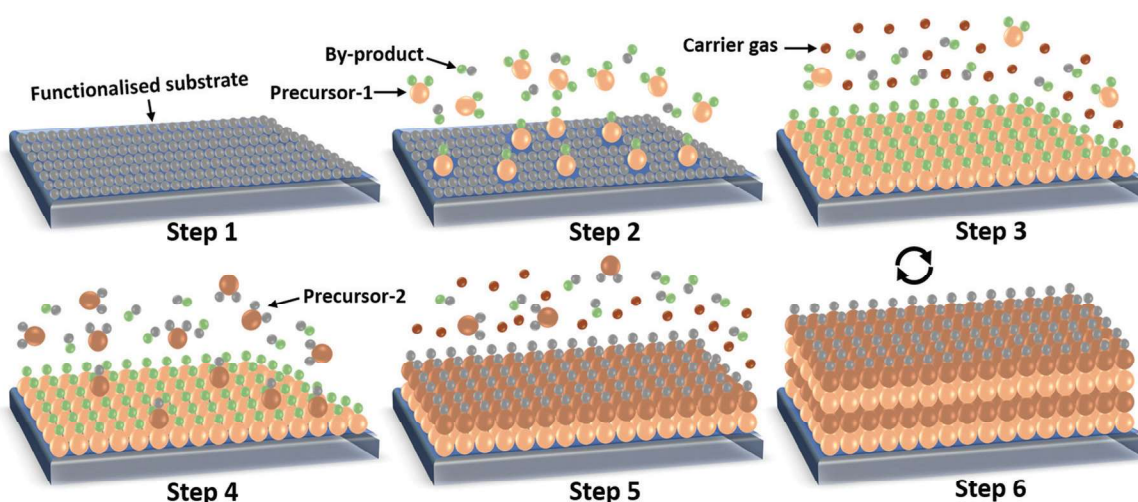


Fig. 5 Schematic of the ALD process for the formation of 2D HSs. Step 1: surface functionalised substrate ready for the next step. Step 2: precursor-1 is introduced, which reacts with the surface of the substrate. Step 3: formation of the self-limiting layer of one material and excess items (precursor and by-product) are purged with a carrier gas. Step 4: precursor-2 is introduced. Step 5: formation of the layer of another material. Step 6: step 2 to 5 can be repeated to get the multiple stacking of 2D HSs.

Ga₂O₃ film over 6.5 nm thick WO₃ film.⁴⁶ ALD has also been proven effective for the synthesis of several other oxide-based 2D HSs such as WO₃/TiO₂ and¹³² TiO₂/Ga₂O₃ HSs.¹³³ Other than oxides, the ALD technique has also been investigated for the synthesis of 2D HSs of TMDs. In a typical example, MoS₂/G and MoS₂/WSe₂ were prepared through integrated ALD where the selection of a precursor salt played a critical role as MoS₂ can only be deposited on graphene by MoF₆, not MoCl₅.¹³⁴ The etching nature of the fluoride precursor made it inappropriate to develop WSe₂/MoS₂, whereas chloride can help overcome this issue.

However, large-scale synthesis using the ALD method is restricted to a few layers of each 2D sheet due to precursor decomposition at the surface of the already deposited 2D sheet which hampers the individual layer, hence, causing subsequent heteroepitaxial growth. Thus, to obtain a uniform and sharp heterointerface between the two individual layers, covalent functionalisation is vital because the absence of any strong interaction between the interfaces restricts the growth to a few layers thickness. Despite its advantages, the ALD growth process is highly surface dependent; therefore maintaining a uniform substrate condition all over the surface is highly desired, and any minute variability even at the ppm level may affect the quality adversely. Moreover, slow reaction kinetics, low-temperature precursor condensation and high-temperature rapid distortion or precursor decomposition need to be addressed for high-quality uniform growth of 2D HSs. More efforts need to be put forward to make ALD an effective technique for the large-scale synthesis of 2D HSs by modifying the existing methods.

4.3 Physical vapour deposition

PVD provides a great level of control over the stoichiometry and the number of monolayers.^{135,136} PVD includes various film deposition methods such as sputtering, pulsed laser deposition (PLD) and molecular beam epitaxy (MBE), in which growth of

the films is proceeded at ultrahigh vacuum (UHV). In the PLD technique, the deposition of large-area continuous crystalline materials can be effectively regulated by controlling the laser pulse duration and exposure cycle, power density and rotation speed, substrate temperature and cooling rate.^{137,138} 2D HSs of MoS₂,¹³⁹ MoSe₂,¹⁴⁰ WSe₂,¹³⁹ ZnO¹⁴¹ and SnSe₂¹⁴² using PLD have been reported; however, most of the 2D HSs are restricted to only a few layers due to structural instability at large stacking. Moreover, the PLD technique is mostly used for the growth of vdW 2D HSs as the formation of a covalent bond restricts the growth due to strain and lattice mismatch conditions. However, a few reports on covalently bonded lateral HSs have also been presented recently.¹⁴³ For example, a high-quality MoSe₂/WSe₂ 2D HS with a sharp heterointerface is fabricated by the PLD-assisted selenisation method as shown in Fig. 6a.¹⁴⁰ The initial morphological observation using a field emission SEM (FE-SEM) presented in Fig. 6b shows the growth of two distinct regions and detailed characterisation validated the formation of the inner triangle MoSe₂ and outer WSe₂. Moreover, the sharp lateral heterointerface between MoSe₂ and WSe₂ occurred within ~2 nm, as observed by high-angle annular dark-field (HAADF)-STEM (Fig. 6c and d). The vdW epitaxy by MBE has also been successfully used to construct a very sharp heterointerface between MoSe₂ and hBN on the Ru(0001) surface to tune their properties.¹⁴⁴ However, the large-area fabrication of MoSe₂/hBN by vertical stacking is inexplicable due to the lack of strong interaction among the individual layers. MBE requires a close lattice matching condition to satisfy the individual sheets, thus restricting the large-scale growth of 2D HSs. To overcome this issue, hybrid MBE has been devised where a suitable substrate Ni/MgO(111) was designed to allow the formation of stacked h-BN/G 2D HSs.¹⁴⁵

MBE has proven very effective in fabricating more than two layers and superlattice 2D vdW HS; for example, Vishwanath *et al.* have grown the 2D HS of MoTe₂/MoSe₂ and four different

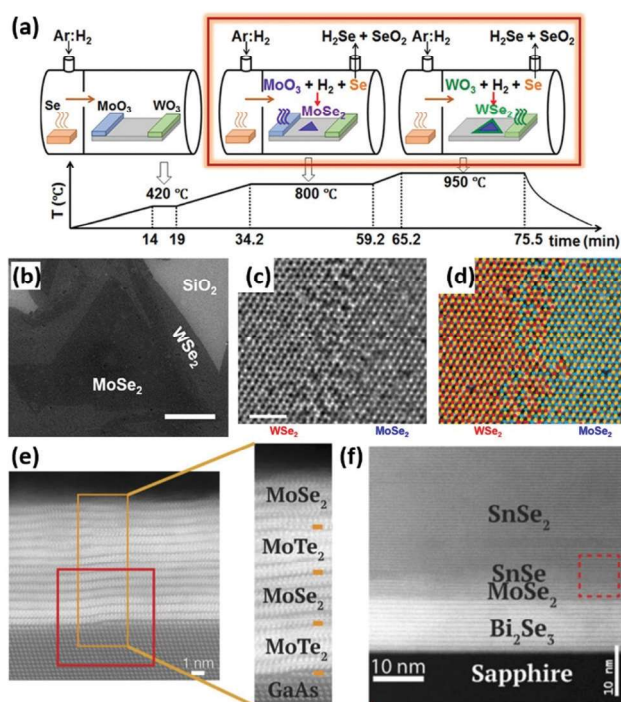


Fig. 6 (a) Schematic representation of the experimental setup of the PLD-assisted growth mechanism for monolayer MoSe_2 - WSe_2 lateral HSS. (b) FE-SEM image of a lateral HSS; the slightly dark inner triangle is MoSe_2 surrounded by WSe_2 (the scale bar is 5 μm). (c) HAADF-STEM image near the $\text{WSe}_2/\text{MoSe}_2$ heterointerface (the scale bar is 2 nm). (d) STEM image with atomic overlay. Reproduced with permission from ref. 140, copyrights reserved to American Chemical Society 2017. (e) The growth of a $\text{MoTe}_2/\text{MoSe}_2$ HS via MBE. (f) The growth of a $\text{Bi}_2\text{Se}_3/\text{MoSe}_2/\text{SnSe}/\text{SnSe}_2$ HS via MBE. Reproduced with permission from ref. 146, copyrights reserved to Materials Research Society 2016.

layers ($\text{Bi}_2\text{Se}_3/\text{MoSe}_2/\text{SnSe}/\text{SnSe}_2$) with an abrupt heterointerface on the GaAs and sapphire substrate, respectively (Fig. 6e and f).¹⁴⁶ Besides, a significant number of other vdW 2D HSSs such as $\text{WSe}_2/\text{Bi}_2\text{Se}_3$,¹⁴⁷ $\text{SnSe}_2/\text{Bi}_2\text{Se}_3$,¹⁴⁷ $\text{HfSe}_2/\text{TaSe}_2$,¹⁴⁸ and $\text{MoTe}_2/\text{MoSe}_2$ ¹⁴⁹ have also been synthesised by MBE, which indicates that the growth of vdW HSSs is more preferred in MBE.

There are only a handful of reports of successful development of centimetre-scale 2D HSSs due to the challenges associated with lattice mismatch and strain conditions. Moreover, the growth of the material in MBE is carried out at ultrahigh vacuum, which hampers the economic aspects of the devices as well.^{114,145} Besides several advantages of PVD, large-scale fabrication needed for industrial applications and standards is still challenging and poses many inexplicable concerns of necessity to improve the grain size, film continuity, abrupt interfaces, uniform structure and atomic scale thickness control at rather lower synthesis temperatures. Moreover, the requirement of highly sophisticated setups and ultrahigh vacuum is another shortcoming of PVD techniques.

4.4 Electrochemical deposition

ECD is a promising and facile technique in which the deposition of elements occurs *via* redox reactions, and the composition of the material can be controlled fairly.¹⁵⁰ The deposition of

materials using this technique can be controlled easily by varying the process parameters such as deposition time, potential and composition of the electrolyte. Various factors affect the coating thickness and morphology of materials such as the bath chemistry, applied potential and temperature.^{151,152} The ions associated with deposited elements/compounds are dissolved in an electrolyte. Based on the nature of materials to be deposited, the ECD process can be of two types: cathodic or anodic.¹⁵³ For example, in a typical ECD synthesis of MoS_2/G , a monolayer graphene deposited by CVD on a SiO_2/Si substrate acted as an anode and a carbon resistant rod or another graphene sheet worked as a cathode. An aqueous solution of ammonium tetrathiomolybdate ($(\text{NH}_4)_2\text{MoS}_4$) was used as an electrolyte.¹¹⁶ Through the redox reaction on corresponding electrodes, the material is deposited; thus, there is no need for any transfer or other processing steps. Subsequently, high-quality large-area and highly economical vertical MoS_2/G 2D HSSs can be obtained.¹¹⁶ Moreover, crystallinity and the atomic arrangements can be controlled by increasing electrolyte concentration and current density on the anode to construct desired 2D HSSs.

Large-area and high-quality 2D HSSs can be achieved using this method, but creating perfect heterointerfaces across the entire basal plane still requires significant attention. Unfortunately, creating wafer-scale homogeneous 2D HSSs using ECD is also a great challenge. Moreover, the multilayer film stacking in the vertical direction presents many challenges due to the strain between the layers and abrupt interfaces. ECD is an emerging process, and only a few reports are found in the literature; therefore, more research is needed to explore this technique for the desired applications.

4.5 Hydro-/solvo-thermal synthesis

Hydro-/solvo-thermal methods are most convenient approaches for the scalable synthesis of 2D HSSs. These methods have been used to create well-defined heterointerfaces between two nanosystems through covalent linkages. For instance, the strong heterointerfacial contact between Ti_3C_2 and Bi_2WO_6 has been achieved to tune their electronic properties and charge transfer properties through the hydrothermal process.¹⁵⁴ Simply, Bi^{3+} cations were introduced into the Ti_3C_2 containing solution followed by hydrothermal treatment to construct ultrathin $\text{Ti}_3\text{C}_2/\text{Bi}_2\text{WO}_6$ nanosheets. Similarly, the hydrothermal treatment was also used to construct $\text{Ti}_3\text{C}_2/\text{MoS}_2$ 2D HSSs to obtain enhanced electrochemical performance through shortening the ionic diffusion and increasing active sites and various valence states.¹⁵⁵ Interestingly, the hydrothermal approach is also useful to construct 2D HSSs of multiple materials, *e.g.* $\text{Ti}_3\text{C}_2/\text{TiO}_2/\text{MoS}_2$.¹⁵⁶

In brief, TiO_2 nanosheets were deposited on Ti_3C_2 , and then MoS_2 was grown on the (101) facets of TiO_2 . The results confirmed that the covalent heterointerface facilitates the charge transfer successfully among the three materials through interfacial connections, hence giving entirely new properties to the $\text{Ti}_3\text{C}_2/\text{TiO}_2/\text{MoS}_2$ 2D HS. Moreover, the hydrothermal approach was also utilised to obtain stable perovskite-based 2D HSSs with $\text{g-C}_3\text{N}_4$ nanosheets.¹⁵⁷ Fig. 7a shows the growth of the $\text{K}^+\text{Ca}_2\text{Nb}_3\text{O}_{10}^-/\text{g-C}_3\text{N}_4$ 2D HS, where $\text{K}^+\text{Ca}_2\text{Nb}_3\text{O}_{10}^-$ was obtained by exfoliating the $\text{HCa}_2\text{Nb}_3\text{O}_{10}$ powder using tetrabutylammonium hydroxide solution followed by hydrothermal reaction in the presence of $\text{g-C}_3\text{N}_4$.

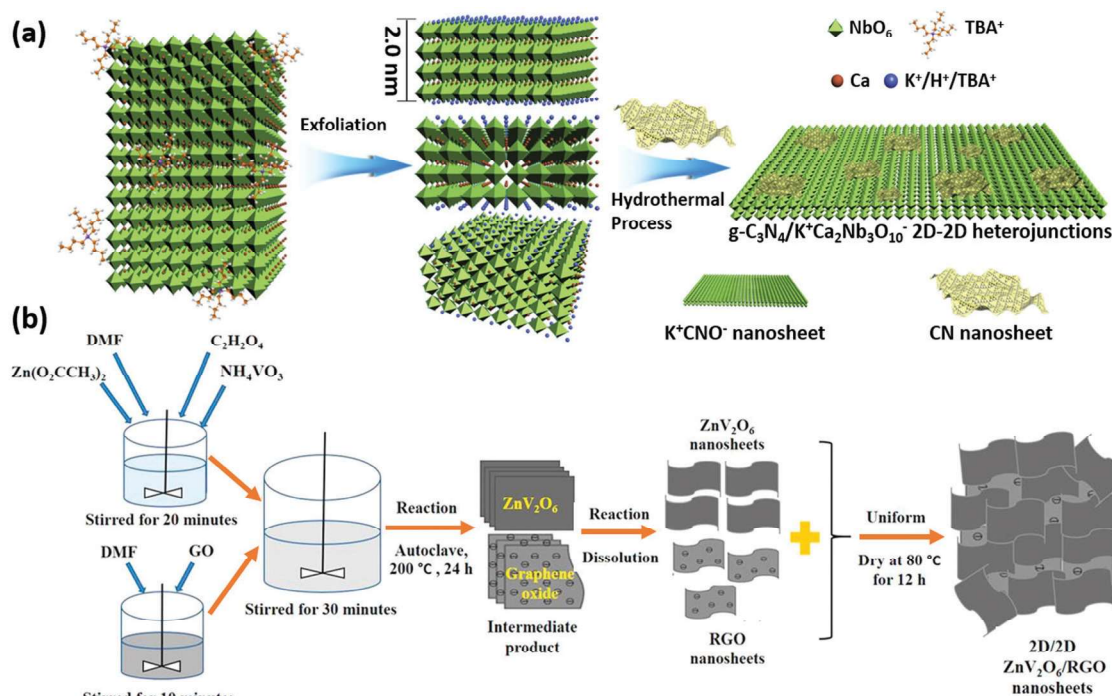


Fig. 7 Solution based synthetic process of 2D HSs. (a) Illustration of the CN/ K^+CNO^- nanosheet heterointerface. Reproduced with permission from ref. 157, copyrights reserved to Elsevier 2017. (b) Solvothermal synthesis of ZnV_2O_6/rGO . Reproduced with permission from ref. 158, copyrights reserved to Elsevier 2018.

Besides hydrothermal methods, solvothermal methods have also been used to fabricate covalently bonded 2D HSs such as oxidised graphitic C_3N_4/TiO_2 (O-g- C_3N_4/TiO_2).¹⁵⁹ The covalent linkages of N-O-Ti formed at the heterointerface between O-g- C_3N_4 and TiO_2 nanosheets were evidenced with various experimental and theoretical techniques. Bafaqeer *et al.* fabricated the ZnV_2O_6/rGO 2D HS by a facile solvothermal method (Fig. 7b).¹⁵⁸ Initially, ammonium metavanadate (NH_4VO_3) was dispersed in *N,N*-dimethyl formamide (DMF) and zinc acetate with continuous stirring to obtain a homogeneous solution, and then oxalic acid was added to NH_4VO_3 . A certain amount of graphene oxide was added to the solution. Then the resulting solution was heat treated to obtain ZnV_2O_6/rGO . Solution-based approaches are favourable for growing 2D HSs on a large-scale due to the low cost of the methods and do not require sophisticated equipment; however, one of the major drawbacks is that the heterointerfaces obtained are not atomically sharp and are non-uniform. Further, lack of control over the thickness and the appearance of large impurity sites in 2D HSs are also some of the key shortcomings of these techniques. However, overcoming these shortcomings can make solution-based methods effective and attractive techniques for growing 2D HSs on a large scale.

4.6 Layer-by-layer assembly

To overcome the challenges associated with the afore-mentioned synthesis approaches, the LbL assembly method, which is a versatile, robust, simple, and inexpensive technique, is being investigated. It can be used for the synthesis of highly ordered

multilayer 2D HSs with controlled composition from all kinds of 2D materials.^{160–162} In general, to synthesise 2D HSs *via* LbL, alternate adsorption of different 2D sheets that exhibit attractive forces between each other is carried out. These attractive forces may include vdW forces, hydrogen bonding, and electrostatic interactions.^{163,164} Typically, substrates are dipped in solutions containing desired materials alternately for a specific time, followed by rinsing intermittently to help remove the disordered and excess component. Repetition of the process results in the formation of multi-layered ordered structures.¹⁶⁴

One of the major drawbacks of the traditional LbL assembly technique is time consumption particularly for thin layers. To address the time challenge, the addition of DMMF into the layering solution as a dewetting agent has been reported to eliminate the rinsing requirements.¹⁶⁵ On the other hand, in another study, stirring was introduced for mixing to reduce the synthesis time by 15 min without impacting the quality of 2D HSs, which was named the ‘agitated-dipping (AD) LbL technique’.¹⁶⁶

Moreover, widely recognised high-speed spin and spray assisted LbL approaches can be employed for the quick and large production of uniform 2D HSs at low cost.^{167–169} The spin assisted LbL method can generate strong interactions at the heterointerface because of the presence of strong forces such as centrifugal force and air-shear force, thus improving the quality of 2D HSs. Furthermore, the LbL self-assembly method can be sub-divided into two methods: (i) Langmuir–Blodgett and (ii) electrostatic LbL self-assembly. The Langmuir–Blodgett assembly method is used for the synthesis of uniform and densely packed 2D HSs with high-quality heterointerfaces.¹⁷⁰

This method involves the deposition and assembly of charged monolayers absorbed at the water interface onto a solid substrate by a dipping process. Furthermore, the material packing density and arrangement are modified by the applied pressure.¹⁷¹ MoS₂/G¹⁷² with a uniform interface is one of the 2D HSs synthesised using this technique. One major challenge associated with this technique is its slow rate of production, thereby, hindering its full scalability potential. On the other hand, the electrostatic LbL self-assembly method (discussed in Section 4.7) is a faster method that ensures heterointerface uniformity at the nanoscale level.

Another challenge is the difficulty in maintaining the intrinsic properties of the constituent 2D materials during large-scale assembly; thus, only proof of concept at the small-scale level existed.^{43,48,173,174} A programmed vacuum stack (PVS) assisted LbL assembly was reported to address the large-scale synthesis of MoSe₂/MoS₂/WS₂ 2D HSs with high uniformity according to the following steps:⁴⁸ (I) individual synthesis of the wafer-scale monolayer of the constituent 2D TMDs; (II) spin-coating of the initial layer with polymer adhesive film and subsequent peeling using thermal tape; (III) first layer stacking of the constituent 2D

TMD monolayer in a vacuum; (IV) substrate removal by peeling using thermal tape; (V) repeating of steps (III) and (IV) until the desired number of layers is achieved (Fig. 8a). Fig. 8b shows the stacked layers of MoS₂, with a circular region of L0 (5 cm diameter) after initial peeling (left), and a further three layer films (right) upon stacking of 2.5 cm wide-square monolayers (L1 and L2). Fig. 8b (left) further shows that each layer remained uniform up to 5 layers, which is further confirmed by the Raman spectra and mapping (Fig. 8c–e). Furthermore, the XRD analysis shows a diffraction peak at $2\theta = 14^\circ$ (Fig. 8f), and the peak intensity was reported to be five-times higher than that of the non-PVS process. In addition, the cross-section STEM image of the MoSe₂/MoS₂/WS₂ film (Fig. 8g) shows a successful vertical stacking. The results demonstrate that with a suitable strategy, the PVS process can be used for large-scale production of 2D HSs with clean interfaces and pure interlayers.

4.7 Electrostatic self-assembly

The electrostatic self-assembly method is a bottom-up technique used for the synthesis of 2D HSs by directly stacking 2D sheets over one another. This technique requires the successive

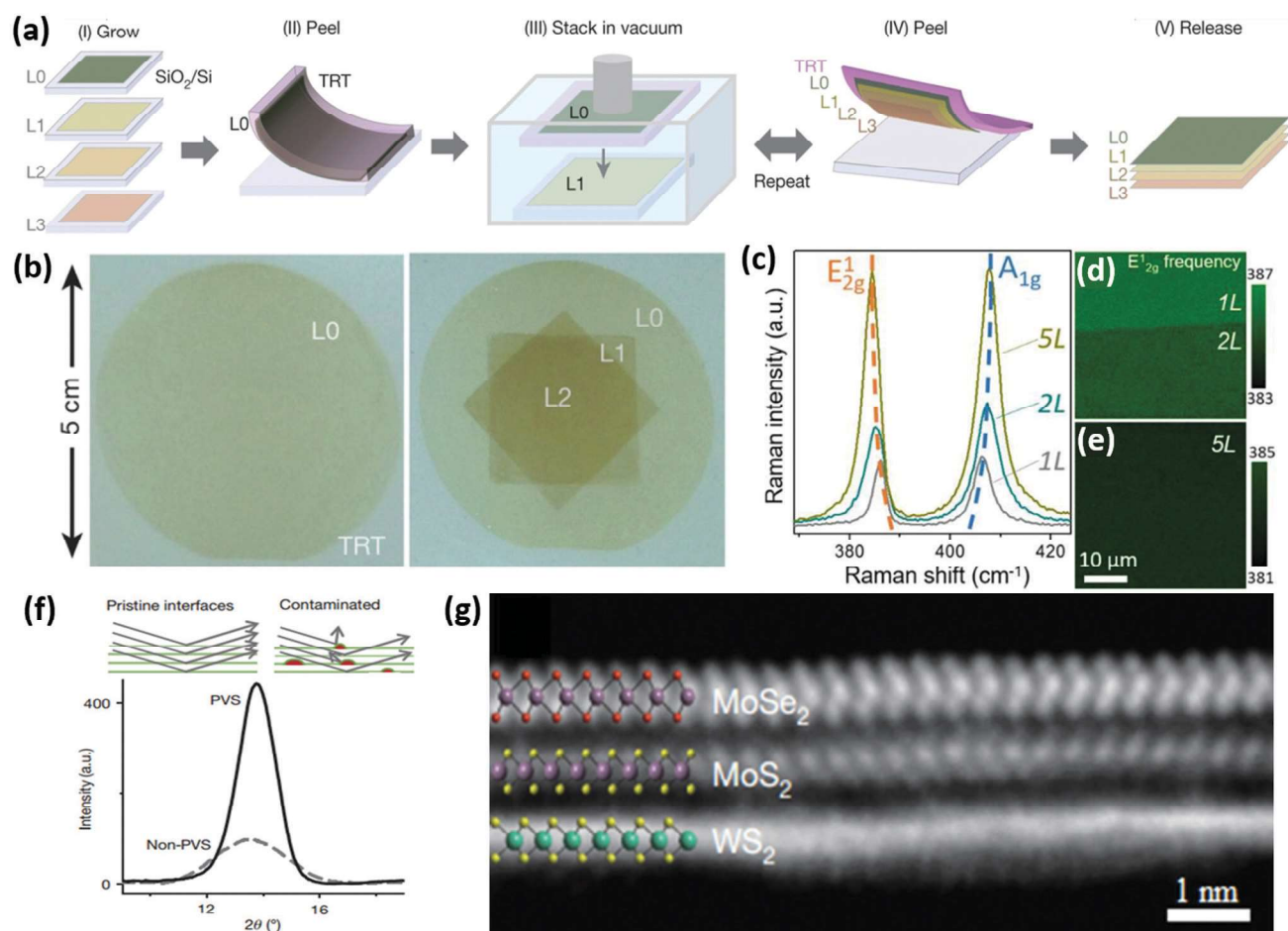


Fig. 8 (a) Schematic description of the PVS process. (b) Images of wafer-scale MoS₂ films after steps (II) and (IV) in the scheme. (c) Raman spectra and (d) Raman frequency mapping of peak E_{2g}¹ across 1L- and 2L-MoS₂ films and (e) Raman frequency mapping of peak E_{2g}¹ at 5L-MoS₂. (f) XRD pattern of MoS₂ and (g) the cross-section STEM image of MoSe₂/MoS₂/WS₂. Reproduced with permission from ref. 48, copyrights reserved to Springer Nature 2017.

constituent 2D materials to be oppositely charged. This technique is a versatile method that has been used for the stacking of any electrochemically active 2D materials.^{175–177} One major drawback with this technique is that most electrochemically active 2D materials are negatively charged, and thus, it requires surface charge modification to ensure electrostatic attraction. For example, Xiong *et al.* utilised poly-(diallyldimethylammonium chloride) (PDDA) as a surface charge modifier to develop $\text{Ti}_{0.87}\text{O}_2/\text{NG}$ using the electrostatic self-assembly method as shown in Fig. 9a.⁴⁷ The high-resolution transmission electron microscopy (HRTEM) image shows alternate stacking (lattice fringes ~ 0.4 nm and ~ 0.7 nm) of the constituent 2D materials (Fig. 9a) and the d -spacing in the XRD pattern, ~ 1.1 nm, (Fig. 9b) is consistent with that of the HRTEM (Fig. 9c). These results confirm the formation of 2D HSSs with an ordered structure and alternate stacking of oppositely charged 2D monolayers. Similarly, PDDA was employed as a surface charge modifier for rGO nanosheets to synthesise $\text{Ti}_3\text{C}_2\text{T}_x/\text{rGO}$ using the

electrostatic self-assembly technique.¹⁷⁸ Ong *et al.* reported another alternative surface charge modification strategy to produce $\text{rGO}/\text{g-C}_3\text{N}_4$ by protonating $\text{g-C}_3\text{N}_4$ using HCl, thus making its surface positively charged.¹¹⁷ The resultant $\text{rGO}/\text{g-C}_3\text{N}_4$ heterointerface was obtained by electrostatic attraction and π - π stacking of the oppositely charged rGO (negatively charged) and $\text{g-C}_3\text{N}_4$ (positively charged) 2D nanosheets. This strategy has also been extended for the synthesis of $\text{Ti}_3\text{C}_2/\text{g-C}_3\text{N}_4$,¹⁷⁹ $\text{Ni}_2\text{P}/\text{CdS}$,¹⁸⁰ and many other materials.

In general, the LbL assembly and electrostatic self-assembly methods can be used for the synthesis of any kind of 2D vdW HSSs. However, material modification is needed for synthesising covalently bonded 2D HSSs, especially in the case of the electrostatic self-assembly method. As suggested by Marcus, in bond formation, transferring a huge amount of electronic-charge is governed by two rules:¹⁸¹ the constituent materials must have a (i) difference in Fermi levels and (ii) large density of state

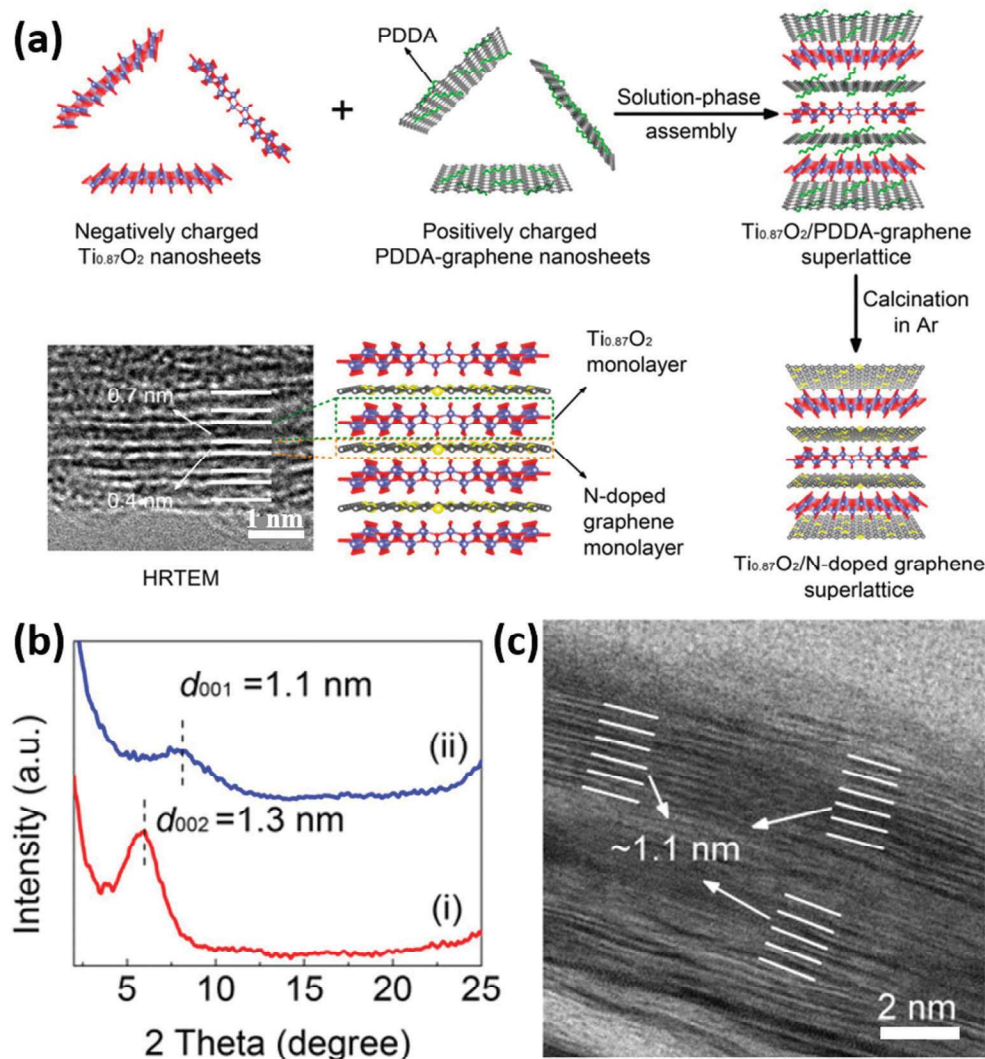


Fig. 9 (a) Schematic illustration of the synthesis of the $\text{Ti}_{0.87}\text{O}_2/\text{NG}$ superlattice. (b) The XRD patterns of the (i) $\text{Ti}_{0.87}\text{O}_2/\text{PDDA}$ graphene superlattice and (ii) $\text{Ti}_{0.87}\text{O}_2/\text{NG}$ superlattice. (c) HRTEM image of the $\text{Ti}_{0.87}\text{O}_2/\text{NG}$ superlattice. Reproduced with permission from ref. 47, copyrights reserved to American Chemical Society 2018.

between the two Fermi levels. In 2D HSs, only the first rule is fulfilled and thus the ease of synthesising vdW based 2D HSs, as no bond is formed. To achieve covalent based 2D HSs, the two rules must be fulfilled, as there must be a transfer of a large amount of electronic charge between the constituent 2D materials. Adopting the strategy of surface charge modification using a polyelectrolyte (cationic and anionic), sufficient opposite charges might be created, strong enough to reduce the interlayer spacing between 2D materials in 2D HSs. Therefore, the electrostatic self-assembly method might be the key in actualising covalently bonded 2D HSs.

4.8 Interface-assisted synthesis

The interface-assisted synthesis method has been introduced recently for the fabrication of 2D HSs, which has great potential for large-scale production. 2D HSs are fabricated by employing a well-constructed interface as an in-plane template to direct the growth by limiting the main reaction at the interface.¹⁸² Interfaces generally used can be broadly categorised into four types: liquid–solid, gas–solid, gas–liquid and liquid–liquid interfaces, and a general process for each type is shown in Fig. 10a.⁴⁹ The liquid/solid interface synthesis method involves an already grown 2D sheet/single-crystal solid surface that works as an atomically perfect flat interface to propagate polymerisation in liquid media and at the same time supports the deposited sheet.^{183,184} On the other hand, in gas–solid interface synthesis, polymerisation or reaction on the solid substrate is directed by the kinetic process involving nucleation, diffusion, and growth.¹⁸⁵ Further, in liquid–liquid and gas–liquid interfacial synthesis techniques, the chemical reactions take place at the liquid interface with unique characteristics which differ from the bulk solution.^{182,186} The interface is more dynamic for reactions at the phase boundaries compared to the bulk allowing straight assembly of the precursors in a limited 2D space to obtain well-defined 2D HSs.^{175,182} Moreover, the liquid interface region provides lateral mobility of the monomers that enables the growth of large-area 2D HSs. On the other hand, the solid interface having a fixed substrate allows only terraces and grain boundaries which usually lead to the creation of short-range ordered networks on the sheets.¹⁸²

Interface-assisted synthesis provides several advantages such as high mobility of monomers/precursors (enhances reaction efficiency), slow polymerisation rates (helps in the formation of well-ordered structures), atomically flat interfaces and confined spaces for the easy lateral mobility of the monomers that can allow the growth of large-area 2D HSs.¹⁸⁶

Moreover, this technique provides better control over the heterointerface as growth is carried out on already fabricated 2D sheets or as both the sheets are grown by the monomers at the interface by taking advantages of bottom-up synthesis. The manipulation of 2D HSs can be effectively achieved by tuning the heterointerface between the individual sheets due to its thinness or covalent nature.⁴⁹ The presence of the covalent bond between the 2D sheets reduces the electronic conduction pathway between the sheets that results in excellent electrochemical and electronic properties. Different factors such as

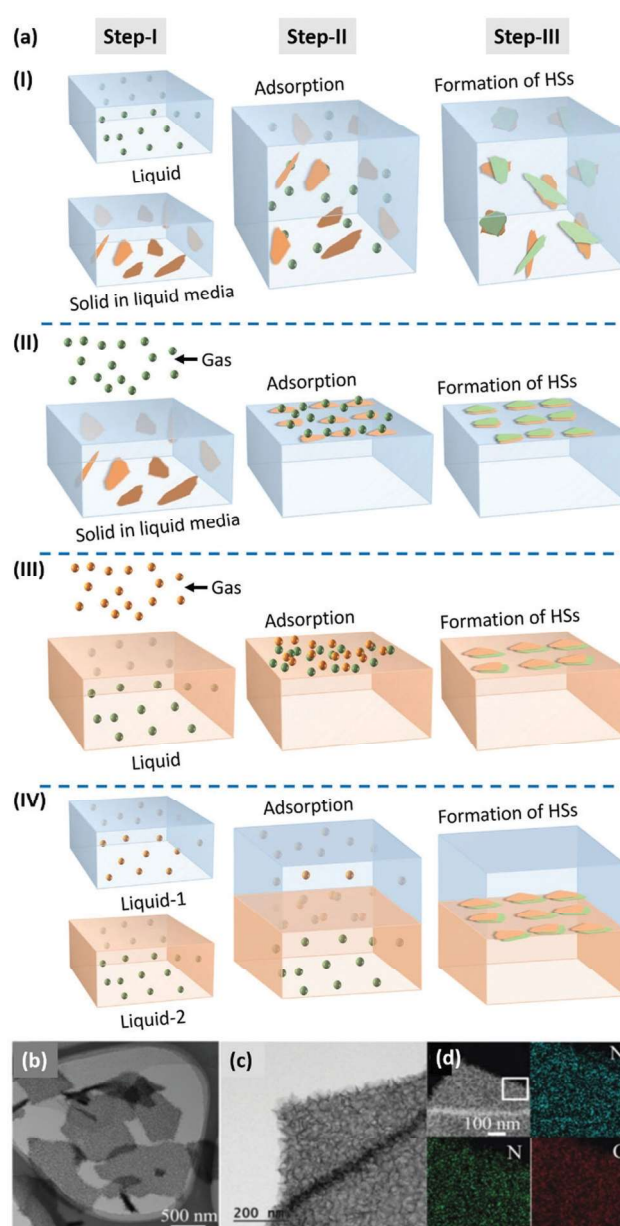


Fig. 10 (a) Schematic illustration of different types of interface-assisted synthesis; (I) liquid–solid, (II) gas–solid, (III) gas–liquid and (IV) liquid–liquid interfaces. Step I – the creation of two different media. Step II – diffusion/adsorption of different materials at the in-plane interface of two different media. Step III – formation of 2D HSs by limiting the growth direction. (b) TEM and (c and d) STEM and elemental mapping images of Ni-ZIF@rGO-F. (b–d) Reproduced with permission from ref. 119, copyrights reserved to Wiley 2020.

surface roughness, molecular orientation, chemical reactivity and selectivity of the interface play key roles in controlling the ordered orientation of the heterointerface.^{186,187}

Many 2D ultrathin films of inorganic, organic, and organo-metallic materials have been successfully deposited in the past; however, only a few have successfully implemented the technique for the growth of 2D HSs.¹⁸⁸ More recently, the interface-assisted direct growth technique is utilised to fabricate metal–organic framework (MOF) nanosheets on rGO.¹¹⁹ A low concentration

assisted heterogeneous nucleation strategy is implemented for the direct growth of a 2D MOF on the rGO surface with controlled orientations. In this process, already grown rGO sheets were used as the solid interface as well as the nucleation site for the MOF constituents dissolved in an appropriate solution. By controlling the time, ultrathin MOF sheets were grown on large rGO sheets in bulk amount. Fig. 10b–d shows the growth on Ni-MOF/rGO; by simply changing the MOF constituents any type of MOF can be grown on rGO (note: here the MOF represents all kinds of frameworks, including zeolites).

No doubt, this method can be used effectively for the large-scale synthesis of 2D HSs with covalent bonding and provides an opportunity for easy heterointerface tuning.¹⁸² However, the low crystalline quality and control over the crystalline phases, grain size, grain boundaries, and edge structures are the major concerns.^{49,188} Further, critical understanding is required regarding the interface-assisted synthesis such as the role of the interface in the preorganisation of precursors and growth of 2D materials, polymerisation reaction, and structural and morphological control by optimising the concentration, ratio, temperature, and pH.^{186,189}

5. Heterointerface characterisation techniques

The nature and chemistry of heterointerfaces are very important; however, there is no single direct technique available by which all characteristics of heterointerfaces can be revealed. Hence, a set of available techniques can be used to probe the characteristics of heterointerfaces in 2D HSs. The theoretical studies can predict a few properties; however, experimental techniques are essential to understand the HSs completely. Moreover, the investigation about the formation, nature and characteristics of heterointerfaces can guide us in designing better 2D HSs and developing scalable synthesis processes. The heterointerfaces formed between lateral 2D HSs are exposed and easily accessible, whereas the heterointerface contact area of vertical HSs is hidden underneath the surface and thus is more difficult to characterise properly. This section will briefly explain how we can utilise available optical, X-ray, scanning probe, electron and diffraction characterisation techniques to determine the characteristics of 2D HSs and their heterointerfaces.

5.1 Optical techniques

Optical microscopy is considered one of the simplest and cheapest techniques to visualise the common features such as position, size, shape and yield of large-area 2D HSs.^{190–192} For instance, optical microscopy was primarily used to assess the large size ($> 100 \mu\text{m}$), triangular shape, and density of CVD grown $\text{WSe}_2/\text{MoSe}_2$ 2D HSs.¹⁹⁰ However, the accuracy of optical microscopy results is highly dependent on the colour contrast of individual constituents, and the resolution limit restricts its applications to some extent. Despite the limitations, optical microscopes are considered as an integral part of mechanical transfer synthesis of vdW 2D HSs, device development and

several characterisation techniques such as AFM and also Raman and PL spectroscopy.

Optical spectroscopy techniques are non-invasive tools for measuring the intensity of absorption or emission of radiation to assess the electronic band structure, structural properties and crystal quality. Sometimes, Raman and PL spectroscopy can be conjugated with second-harmonic generation (SHG) to verify the structural and optical properties of 2D HSs. Amongst various optical spectroscopic techniques, Raman spectroscopy is one of the most rapid optical techniques to probe the interactions of different 2D materials at the heterointerface by observing the changes in vibrational characteristics.¹⁹³ Raman spectroscopy can also help in observing changes in chemical compositions and distributions,^{194,195} doping,^{195,196} structural strains^{196,197} and crystal quality^{195,197} at the heterointerfaces. Interestingly, 2D HSs' stacking order can significantly enhance the Raman scattering compared to the isolated layers,^{198,199} as interlayer coupling at the heterointerface influences the increase of electronic state density at the surface. To make Raman spectroscopy more effective and get a clear picture of heterointerfaces, a combination of Raman and PL spectroscopy is often used. For example, to confirm the formation of MoS_2/WS_2 2D HSs, both Raman and PL spectra from the core, heterointerface and the surroundings were recorded as shown in Fig. 11.²⁰⁰ Raman and PL spectra confirm that the central triangle is MoS_2 while WS_2 is only present at the surroundings (Fig. 11a and e). Further, the structural integrity and high-quality of the sharp heterointerface are also confirmed by Raman and PL spatial mappings as presented in Fig. 11b–d and f–h, respectively. Interestingly, Raman and PL mappings appear to be marginally diffused at the heterointerface of MoS_2 and WS_2 , which might be due to the large laser spot size and mapping step size. As such limitations cannot be circumvented in Raman and PL instruments, other techniques such as transmission electron microscopy (TEM) can be used to resolve such issue accurately.

Moreover, the PL spectrum is also used to evaluate the interlayer electronic characteristics such as interlayer excitonic states and charge transfer at the heterointerface in 2D HSs. The decrease of individual PL signals can be observed due to the interlayer charge transfer in 2D HSs.^{201–203} For instance, when a type II band alignment occurs at the heterointerface of 2D HSs, the bounded electrons and holes known as excitons are localised in individual layers, which can also be investigated using PL.²⁰²

Unfortunately, utilisation of PL is restricted by their bandgap. For instance, while direct bandgap semiconductors, consisting of ultrathin layers, show strong PL signals; weak PL signals may appear in indirect bandgap semiconductors. For example, SnS_2 doesn't show any PL signal due to its indirect bandgap in $\text{SnS}_2/\text{MoS}_2$ vertical 2D HSs, which makes it difficult to identify the heterointerface through PL.²⁰⁵ In such a case, alternative techniques are required, which are capable of identifying and characterising the heterointerface.

5.2 Scanning probe microscopy (SPM) techniques

SPM techniques use a physical probe to study the surface and heterointerface of 2D HSs at the nanoscale level. Furthermore, these

techniques are capable of identifying the exact arrangement of the atoms if the heterointerface is exposed, and thus, they help in defining the nature and characteristics of 2D HSs. Moreover, the SPM technique is not merely a surface visualisation technique, rather it is widely used to interrogate advanced electronic, optoelectronic and mechanical properties at an ultra-high resolution which sometimes cannot be obtained using other techniques. Scanning tunnelling microscopy (STM) and atomic force microscopy (AFM) are the two most common SPM techniques used for the fundamental studies of 2D materials and their HSs.

In STM, a metallic tip is brought to the surface of the sample and the surface local density of states is imaged, observing the tunnelling current while a bias voltage is applied between the probe and the surface.²⁰⁶ STM has a very high spatial resolution of ~ 0.1 and ~ 0.01 nm in the in-plane and out-of-plane direction,

respectively, through which every single atom can be imaged. Surface topographical information can be obtained using STM (Fig. 11i) while scanning tunnelling spectroscopy (STS), an extension of STM, can provide electronic properties of both occupied and unoccupied states. The geometric properties can be studied by STM, whereas STS can be used to study the interfacial band alignment and offset of vertical HSs. Type II band alignment in the HS formed by the monolayers of MoS_2 and WS_2 shows an interfacial bandgap of ~ 1.45 eV while the bandgap of individual MoS_2 and WS_2 is 2.16 and 2.38 eV, respectively.²⁰⁷ A small lattice constant difference and relative rotating angles between the constituting layers in a vertical 2D HS can generate the Moiré pattern which influences the local mechanical and electrical properties.^{208,209} The Moiré pattern can be studied thoroughly using STM. For example, STM reveals

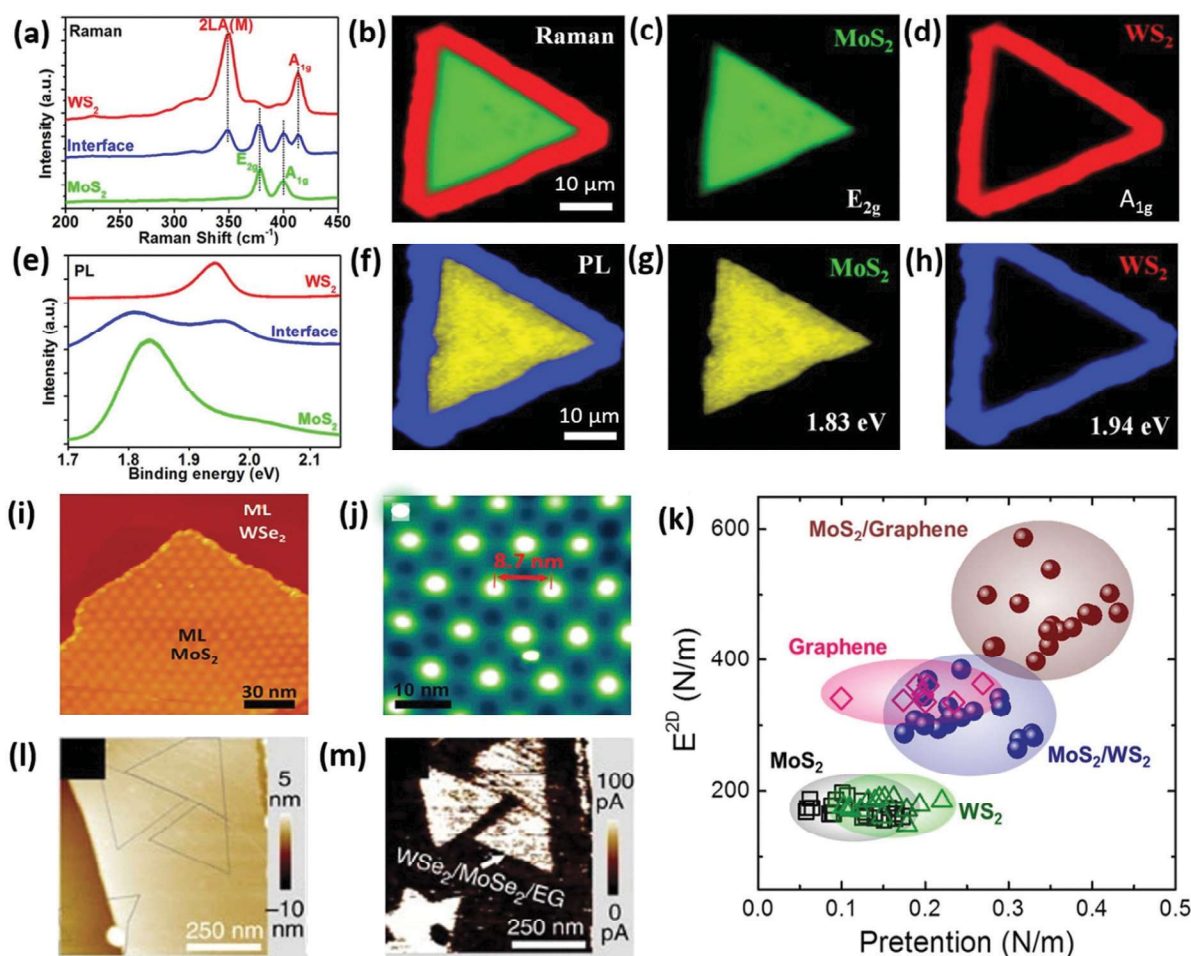


Fig. 11 (a) Raman spectra of central MoS_2 , outer WS_2 and the heterointerface of MoS_2/WS_2 . (b) Combined Raman intensity mapping of the MoS_2 E_{2g} mode and WS_2 A_{1g} mode further confirms the central MoS_2 and outer WS_2 . (c) Raman intensity mapping of MoS_2 E_{2g} only. (d) Raman intensity mapping of WS_2 A_{1g} only. (e) PL spectra show MoS_2 , WS_2 and the heterointerface. (f) Combined PL intensity mapping of MoS_2 and WS_2 at 1.83 and 1.94 eV, respectively, further confirms the central MoS_2 and the outer WS_2 . (g) PL intensity mapping of MoS_2 at 1.83 eV. (h) PL intensity mapping of WS_2 at 1.94 eV. Reproduced with permission from ref. 200, copyrights reserved to American Chemical Society 2015. (i) STM image of the MoS_2/WS_2 HS taken on a highly oriented pyrolytic-graphite substrate. (j) Moiré pattern observed using STM; the MoS_2/WS_2 HS shows a periodicity of 8.7 nm. Reproduced with permission from ref. 194, copyrights reserved to American Association for the Advancement of Science (United States) 2017. (k) Comparison of elastic properties of 2D layers and their 2D HSs. Reproduced with permission from ref. 204, copyrights reserved to American Chemical Society 2014. (l) The MoSe_2 domains are difficult to identify topographically; however, (m) conductive AFM clearly delineates their location due to enhanced tunnelling of the HSs. Reproduced with permission from ref. 124, copyrights reserved to Springer Nature 2015.

that the Moiré pattern on the top MoS₂ layer in the MoS₂/WSe₂ bilayer with a lattice constant of ~8.7 nm appears when the rotating angle between layers is either 0° or 180° (Fig. 11j).²⁰⁹ Despite many advantages, obtaining quality information from STM and STS is often very challenging and time-consuming, and they require high-quality conductive and contamination-free samples, and an atomically flat conductive substrate. However, insulating substrates or samples can be characterised by tuning the experimental parameters or using special arrangements.^{210,211}

Moreover, AFM can easily image three-dimensional topography and characterise the surface and heterointerface at atomic resolution. AFM can provide detailed information about surface morphology, height and relative orientation of layers in 2D HSs.²¹² Apart from imaging, AFM is also an excellent tool to probe the Moiré patterns,²⁰⁸ defects,²¹³ mechanical buckling and sliding of the heterointerface²⁰⁴ relating to 2S HSs. The intrinsic physical parameters such as adhesion energy and friction properties of the heterointerface of 2D HSs are challenging and yet to be reported experimentally. However, the nano-indentation using the AFM tip can be used to examine the relative interlayer interaction in 2D HSs. The elastic moduli of 2D HSs can be measured by indenting the suspended ultrathin 2D HSs with an AFM tip. The elastic moduli of 2D HS constituting monolayers are always lower than the sum of the modulus of individual monolayers probably due to the interlayer sliding. Such observation was found to be true for 2D HSs of MoS₂/WS₂ and MoS₂/G.²⁰⁴ The summation of the modulus of the constituting layers of MoS₂/WS₂ and MoS₂/G is 348 and 520 N m⁻¹, respectively, but the value is reduced to 314 ± 31 and 467 ± 48 N m⁻¹, respectively when 2D HSs are formed (Fig. 11k).²⁰⁴ The relative strain in the form of buckling at the heterointerface of lateral HSs can also easily be observed using AFM.²⁰⁹

Electronic properties are useful to understand the surface potential, Fermi level, and charge transfer of both lateral and vertical HSs which can be observed using the extended function of AFM such as conductive AFM and Kelvin probe force microscopy (KPFM). Local variation in conductivity in HSs can sometimes provide a useful tool to properly locate the heterointerface in 2D HSs, which is not accessible through the standard topography.¹²⁴ The smaller size (~300 nm) of MoSe₂ relative to WSe₂ (~2 μm) in the WSe₂/MoSe₂ HS on exfoliated graphene is difficult to identify through AFM topography as shown in Fig. 11l. However, enhanced current transport across 2D HSs, measured using conductive AFM, can locate the position of MoSe₂ clearly, as shown in Fig. 11m.¹²⁴ The interactions of constituting layers at the heterointerface can also be probed by KPFM, which measures the surface potential difference between the probe tip and the sample surface.^{214,215} Further using KPFM, the relative position of the Fermi level can be determined by measuring the work function of the individual surface, and such measurement is invaluable to understand the band alignment and charge transfer for the design of future heterointerfaces.^{12,216}

5.3 X-ray based techniques

X-ray based characterisation techniques are non-destructive techniques to study the electron transfer,^{217,218} crystal structures,²¹⁹

edge structures,²²⁰ interfacial interactions,^{220,221} surface states,²¹⁹ defects,²²² and chemical compositions^{195,219} during the heterostructuring of various 2D materials. X-ray diffraction (XRD), X-ray photoelectron spectroscopy (XPS), and X-ray absorption spectroscopy (XAS) are the most widely used X-ray based techniques for characterising 2D HSs. Among these, XPS is a surface-sensitive technique particularly convenient to characterise the surface states and interfacial interaction by analysing the binding energies of the different elements in 2D HSs.^{220,223,224} In many cases, the electron configuration of 2D HSs changes due to the formation of the heterointerface and charge transfer between adjacent layers. For example, the charge transfer between constituting layers at the heterointerface of WO₃/g-C₃N₄ causes a shift in binding energies found in XPS spectra, confirming their strong connection at heterointerfaces.²¹⁸ As such, a positive shift of 0.2 eV of C1s and N1s (compared to g-C₃N₄) and a negative shift of 0.2 eV of W⁶⁺ (compared to WO₃) can be observed in the WO₃/g-C₃N₄ 2D HS due to the interfacial charge transfer between WO₃ and g-C₃N₄ layers at the heterointerface (Fig. 12a–c). Such a shift can also be observed in XPS O1s of CoO/CoP 2D HSs (Fig. 12d). However, change in the binding energy alone does not guaranty the formation of a perfect heterointerface; therefore, in-depth electronic structural characterisation may help in getting a better idea such as the use of XPS results along with XAS.

XAS provides overall atomic structure information based on the electronic state of individual atoms. XAS can be divided into X-ray absorption near edge structure (XANES) and extended X-ray absorption fine structure (EXAFS). XANES provides information on the electronic structures and coordination geometry of the absorbing atoms whereas the structural information such as interatomic distances, coordination numbers, and near neighbour atomic type can be obtained using EXAFS. In a typical example, controlled phosphorisation of the precursor yields the 2D HS of CoO/CoP; consequently, the structure and coordination of the CoO/CoP HS are investigated using both XANES and EXAFS.²²⁵ As depicted in Fig. 12e, the Fourier transformed (FT) EXAFS at the Co K edge shows two distinct peaks of CoO/CoP corresponding to Co–P and Co–Co bonds. Moreover, the slight increase of the Co–Co bond distance in CoO/CoP (compared to Co₃O₄) demonstrates the strong interaction between O and metal atoms at the interface.

The first step at 7716 eV of CoO/CoP in the XANES spectrum (Co K edge) proves that the valence of CoO/CoP is located between Co₃O₄ and CoP (Fig. 12f). It has been proven that X-ray based techniques can be very helpful not only in confirming the formation of the heterointerface but also in the characterisation of the chemistry of the heterointerface. However, there are several challenges associated with determining the perfectly repeating order of the heterointerface at each level in stacked HSs due to the operating limitations of these techniques or the associated sample preparations. Therefore, to gain complete structural information of 2D HSs, several X-ray techniques might be used in conjunction. In addition, modifying sample processing procedures can also provide the base for gaining in-depth insight regarding heterointerfaces. For example, the ability of depth profiling in XPS through step-wise etching of the

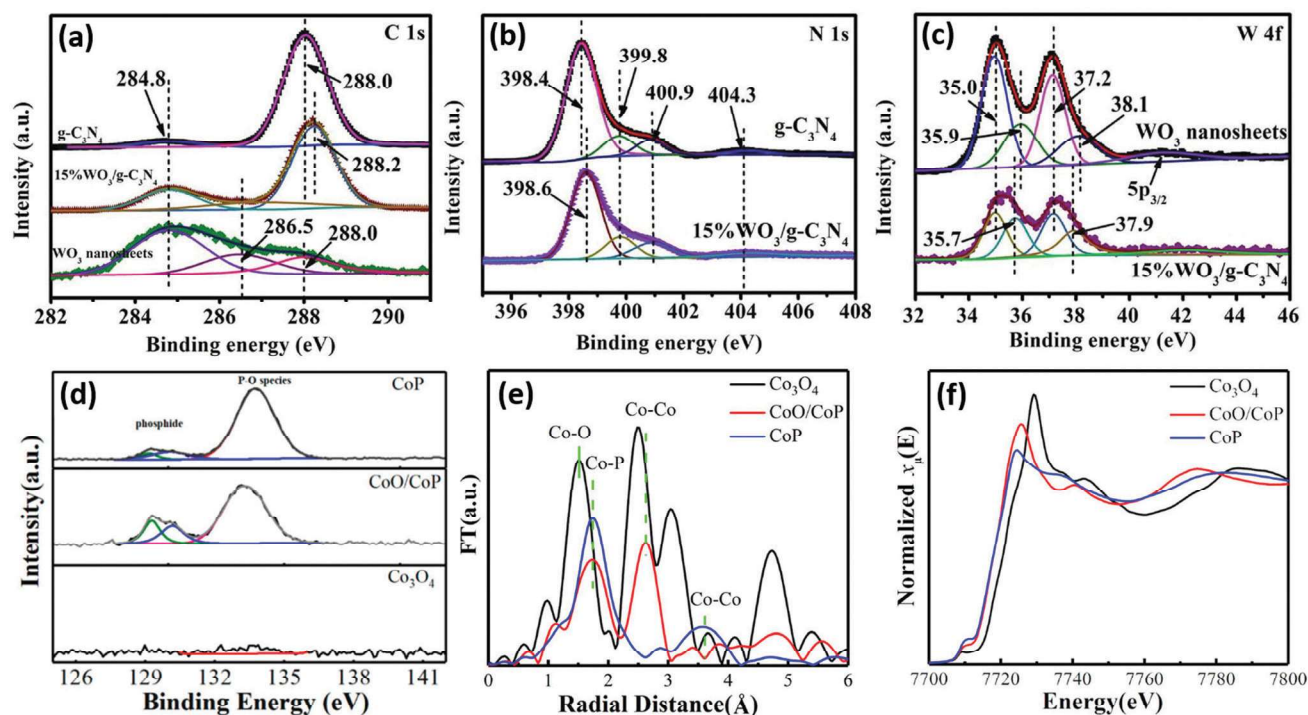


Fig. 12 High-resolution XPS spectra of $\text{WO}_3/\text{g-C}_3\text{N}_4$, WO_3 , and $\text{g-C}_3\text{N}_4$ at (a) C 1s. (b) N 1s. (c) W 4f. Reproduced with permission from ref. 218, copyrights reserved to Elsevier 2019. (d) XPS O1s peaks, Co K edge (e) EXAFS and (f) XANES spectrum of Co_3O_4 , CoO/CoP , and CoP . Reproduced with permission from ref. 225, copyrights reserved to American Chemical Society 2018.

sample can provide information about the nature of a heterointerface. Note: energy-dispersive X-ray spectroscopy (EDS) is also an X-ray based technique used in conjunction with electron microscopy techniques; therefore, it will be covered in Section 5.4.

5.4 Electron microscopy techniques

Electron microscopy mainly includes two generic classes, namely scanning electron microscopy (SEM) and TEM. SEM is primarily limited to the examination of the material surface while TEM can penetrate through the thin samples designed to examine the internal structure. The morphology of 2D HSs irrespective of type (lateral or vertical) or size (small or large-area) can be easily visualised using SEM with a much higher resolution than optical microscopy. In addition, SEM can also roughly differentiate the lateral heterointerfaces in large-area 2D HSs.¹⁹⁵ Unfortunately, even with the help of cross-section, in most of the cases, SEM is not suitable to pinpoint the heterointerface. Similarly, other detailed analyses such as composition, orientation, crystalline properties, interlayer penetration, atomic/structural properties, and defects/disorders of heterointerfaces are also not possible using SEM.

Nonetheless, such a sub-nm spatial resolution and analysis of heterointerfaces is accessible by TEM and its extended imaging and analysis techniques. TEM imaging modes such as bright-field (BF) imaging, selected area electron diffraction (SAED), HRTEM, STEM, and HAADF and spectroscopic techniques such as EDS and electron energy loss spectrometry (EELS) can provide information in real and reciprocal space about the morphology, chemical composition, thickness, atomic defects,

grain boundaries, and stacking sequences of 2D HSs and their heterointerfaces.^{45,224,226–228} In a typical example, small lattice mismatch ($\sim 3.5\%$) driven solution-phase epitaxial growth of cubic PbSe on rhombohedral Bi_2Se_3 resulted in vdW 2D HSs as shown in Fig. 13a.⁴⁵ A TEM image of the surface of $\text{PbSe}/\text{Bi}_2\text{Se}_3$ was taken to confirm the partial coverage of Bi_2Se_3 by growing PbSe (Fig. 13b). Further, the SAED pattern, shown in Fig. 13c, confirms the two sets of diffraction patterns of hexagonal and square along with the lattice spacing, which can be indexed to Bi_2Se_3 and PbSe , respectively.

An atomically resolved HRTEM image of the $\text{PbSe}/\text{Bi}_2\text{Se}_3$ heterointerface can confirm the heterointerface and its excellent crystallinity (Fig. 13d). Moreover, the HAADF-STEM-EDS image (Fig. 13e) and elemental analysis (Fig. 13f and g) can further reveal the chemical composition and elemental distribution of the heterointerface.^{219,229,230} For instance, the composition line scan of EDS presented in Fig. 13f confirms that Se is uniformly distributed in both regions while the Pb and Bi contents are localised in their respective PbSe and Bi_2Se_3 regions, respectively.

No doubt various *ex situ* characterisation techniques have been utilised to characterise the nature of the heterointerface and the formation of 2D HSs. However, no single characterisation technique can accurately present the full analysis of 2D HSs; therefore, a combination of several techniques is imperative to understand the heterointerface and 2D HSs fully. Certainly, the *in situ* characterisation offers a more robust understanding of the evolution processes during the synthesis or device performance. As such, *in situ* STM was used to understand the relief of strain at the G/h-BN lateral heterointerface.⁵⁴ In another example,

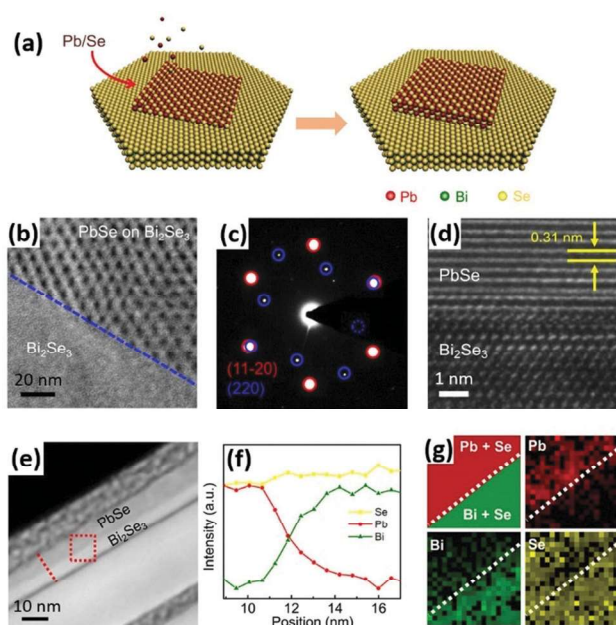


Fig. 13 (a) A schematic illustration of the epitaxial growth of PbSe on Bi_2Se_3 which forms the 2D HS of PbSe/ Bi_2Se_3 . (b) TEM image of the surface of the vertical PbSe/ Bi_2Se_3 HS; the marked blue line distinguishes the bottom layer of Bi_2Se_3 from PbSe/ Bi_2Se_3 HS. (c) SAED of the PbSe/ Bi_2Se_3 HS; the red and blue spots are corresponding to Bi_2Se_3 and PbSe, respectively. (d) Cross-sectional HRTEM image pinpoints the individual constituents and shows the excellent crystallinity of the heterointerface. (e) Cross-sectional HAADF-STEM image of the PbSe/ Bi_2Se_3 HS; the corresponding line profile and elemental mapping are shown in (f) and (g), respectively. Reproduced with permission from ref. 45, copyrights reserved to American Association for the Advancement of Science (United States) 2016.

in situ XRD was carried out for the identification of the product evolution during charging and discharging of CoO/CoP catalyst-based metal–air batteries.⁴⁷ Unfortunately, existing *in situ/ex situ* techniques are unable to pinpoint the heterointerface evolution, behaviour and electron transfer during synthesis and application processes. Therefore, there is a need to put more efforts to completely reveal the hidden science behind the nature and role of the heterointerface in 2D HSs. In fact, theoretical studies can also provide some degree of guidelines which can be opted by the experimental scientists to study the formation mechanism of 2D HSs and the role of the heterointerface in enhancing their performance.

6. Applications of 2D heterostructures

Establishing well-defined heterointerfaces in 2D HSs may lead to intriguing properties, particularly for energy and electronic applications. The targeted applications of 2D HSs vary depending on the synthesis methods, geometries and throughput. For instance, large-area and high-quality 2D HSs developed using methods such as CVD, ALD, PVD, and layer-by-layer assembly offer peculiar advantages in electronics. However, relatively low throughput of these methods may restrict their applications for energy storage and conversion units. Conversely, hydro-/solvo-thermal, electrostatic self-assembly and interface-assisted synthesis

methods can be used for processing large-volume products, which are particularly favourable for energy applications. Considering the potential of heterointerfaces, examples of 2D HSs with well-defined heterointerfaces are presented (note: traditional composites or other geometries like 2D/0D and 2D/1D are not considered here). This section highlights the role of heterointerfaces in realising high power energy storage units, efficient bifunctional catalysts, effective physical/chemical sensors, and neuromorphic/plasmonic applications.

6.1 High power energy storage devices

Energy and power densities, coupled with cycle life, are the major factors that differentiate between batteries and supercapacitors. Taking advantage of the redox charge storage mechanism, batteries are capable of storing larger energies, hence have high energy density values. However, their slow dis/charging rate results in poor power density, thus restricting their applications. On the other hand, supercapacitors can store charge at fast rates, as fast as 100 times that of a battery due to their quick surface accumulation of charges (electric double-layer capacitors, EDLCs) or surface redox process (pseudocapacitors), hence bear high power density, which makes them suitable for applications in devices where millisecond dis/charging is required. However, they possess low energy density, $<10 \text{ W h kg}^{-1}$ (or specific capacitance $<100 \text{ F g}^{-1}$) (Fig. 14a), thus storing lesser energy than batteries.^{17,231} For both batteries and supercapacitors, the limited power density and energy density is determined by the inherent characteristics of their electrode materials and the way energy is stored in electrodes. Research over the last decade or two has been dedicated to producing energy storage devices that are capable of combining the high energy density of batteries with the power density and longevity of supercapacitors, presented as high power energy batteries in Fig. 14a.

Energy and power density of tradition systems can be improved by developing battery–supercapacitor hybrid (BSH) devices,^{232,233} where one of the electrodes of symmetric supercapacitors is replaced with that of a battery, thus giving the device an unprecedented combined property of batteries and supercapacitors. Intercalation type electroactive titanium oxide-based compounds, e.g. $\text{Li}_4\text{Ti}_5\text{O}_{12}$ (LTO)²³⁴ and $\text{Na}_2\text{Ti}_3\text{O}_7$ (STO),²³⁵ are often used as the anode while capacitor-type activated carbon (AC) is used as a cathode. No doubt, synergising the properties of batteries and supercapacitors to produce high energy and power density devices looks fascinating but still challenging as batteries and supercapacitors have a different electrochemical mechanism. For example, ionic storage in batteries is controlled by the diffusion of metal/electrolytic ions (e.g. Li^+ , Na^+ , K^+ , Zn^{2+} , etc.) across the electrode materials; thus, many ions can be stored deep in the bulk but require more time.²³⁶ On the other hand, in supercapacitors ion storage takes place at the surface, which is a much quicker process but can only store limited number of ions.²³¹ For optimum performance, the capacity of both electrodes to store ions must be balanced, and it is usually achieved by optimising the mass loading of each electrode.

This ultimately results in energy density similar (though slightly increased) to that of traditional pseudocapacitors.

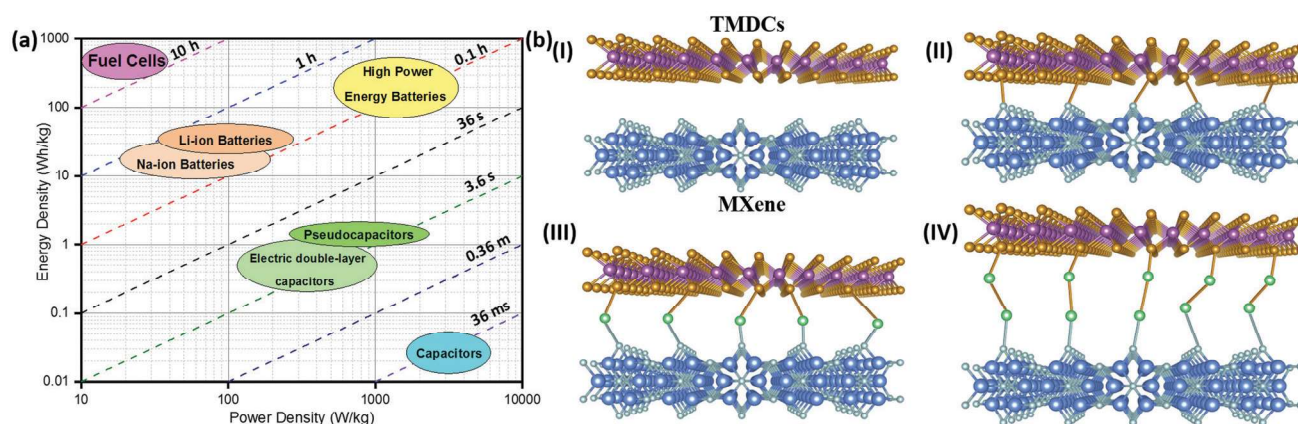


Fig. 14 (a) Ragone plot showing the capabilities of different devices and pointing future needs. (b) Schematic illustration of different types of 2D HSs with tunable heterointerfaces to be used as an electrode for energy storage devices.

Therefore, the only possible way to handle this challenge is by designing materials in a way that allows direct access to each active site of a bulk battery electrode. Recently, the development of 2D HSs has led to the possibility of such design of electrodes which will be capable of providing the opportunity to engineer the interface in such a way that electrolytes will be able to access active sites directly. The face-to-face contact in 2D HSs between dissimilar 2D materials ensures better charge realignment by providing larger specific contact area and active sites, thus maximising the storage potential. Moreover, the presence of large interlayer spacing and heterointerfaces in 2D HSs (large enough to accommodate ions like Na^+ and K^+) serves as channels for faster mass transfer of ions and storage, coupled with increasing diffusion (both on the surface and in the bulk material) and adsorption of electrolytic ions.^{27,229,231}

Furthermore, to achieve high volumetric energy and power densities, there is a need for high packing density, large active redox surfaces, a lesser distance for electron diffusion and sufficient interlayer spacing. All these are achievable using 2D HSs; however, just like constituent 2D materials, 2D HSs have the propensity for self-restacking into excessive layers if not properly engineered, thus eliminating the merits of the HSs.^{237,238} Further, faster electrolyte/ion movement can be achieved by tuning interlayer spacing with negligible diffusion resistance. Experimental and computational studies have shown that doping one of the constituent 2D materials of 2D HSs (e.g. G/MoS_2) will result in increased interlayer spacing.^{239,240} For example, nitrogen doping in graphene increases the interlayer spacing from 0.62 nm to 0.98 nm at the heterointerface in NG/MoS_2 .¹⁰² This enlarged interlayer spacing will ensure rapid diffusion of ions (including larger ones such as Na^+ , K^+ , Mg^{+2} , and Al^{+3}) and compensate structural changes during cycling. In addition, taking advantage of covalent connection through linkers, the interlayer distance and heterointerface chemistry can easily be tuned to achieve desired properties (Fig. 14b). Although enlarged interlayer spacing is desirable in 2D HS-based electrodes, care must be taken not to over increase the spacing. In 2D HSs, charge transfer across layers (both laterally and vertically) and redistribution are responsible for the efficiency and performance of the electrode.¹⁰⁶ With increasing

interlayer spacing, larger electrolytic ions like Na^+ and K^+ and their intercalation reaction products can easily pass through. However, if the interlayer spacing is too large, a decrease in the magnitude of charge transfer across layers (both laterally and vertically) and redistribution will occur, consequently reducing the performance of the electrodes.

Combining dissimilar 2D materials into 2D HSs and studying them for potential applications as an electrode in high power and high energy storage devices requires an understanding of the properties of constituent 2D materials. TMDs, e.g. MoS_2 and MoSe_2 , and TMOs, e.g. V_2O_5 and MoO_3 , are known to have redox potentials and exhibit high performances in batteries. Graphene and MXenes, on the other hand, are characterised to possess high metallic conductivity, with exceptional performance as an electrode in supercapacitors and pseudocapacitors, showing high charge and discharge rates. Therefore, combining TMDs or TMOs with graphene or MXenes to form 2D HSs will eliminate their limitations, and the resultant 2D HSs will be redox-active, highly conductive and flexible. For example, Xu *et al.* synthesised $\text{MoSe}_2/\text{Ti}_3\text{C}_2\text{T}_x\text{-MXene}$ by a hydrothermal method and evaluated its performance in the sodium-ion battery (SIB).²⁴¹ They reported that MoSe_2 and $\text{Ti}_3\text{C}_2\text{T}_x\text{-MXene}$ are joined together by strong vdW attractions at the heterointerface. Also, the lattice fringes of MoSe_2 were partially distorted at the heterointerface due to lattice mismatch between MoSe_2 and $\text{Ti}_3\text{C}_2\text{T}_x\text{-MXene}$ (Fig. 15a). Furthermore, the DFT study showed an indirect band (~ 1.01 eV) for MoSe_2 near the Fermi level (Fig. 15b), confirming its semiconductor nature; thus, MoSe_2 could result in sluggish kinetics as an electrode in batteries. On the other hand, the band structure of $\text{Ti}_3\text{C}_2\text{T}_x\text{-MXene}$ (Fig. 15c) showed a filled conduction band confirming its metallic property. On combining $\text{Ti}_3\text{C}_2\text{T}_x\text{-MXene}$ with MoSe_2 to form 2D HSs, the empty conduction band of MoSe_2 became filled with $\text{Ti}_3\text{C}_2\text{T}_x\text{-MXene}$ and moved to the Fermi level, thus making $\text{MoSe}_2/\text{Ti}_3\text{C}_2\text{T}_x\text{-MXene}$ metallic (Fig. 15d). The metallic property of $\text{MoSe}_2/\text{Ti}_3\text{C}_2\text{T}_x\text{-MXene}$ could in turn facilitate rapid ionic transport between $\text{Ti}_3\text{C}_2\text{T}_x\text{-MXene}$ and MoSe_2 , thus leading to faster electrochemical kinetics. In addition, Na^+ diffusion pathways on $\text{Ti}_3\text{C}_2\text{T}_x\text{-MXene}$ (Fig. 15e) and MoSe_2 (Fig. 15f) showed the presence of two stable sites for adsorption

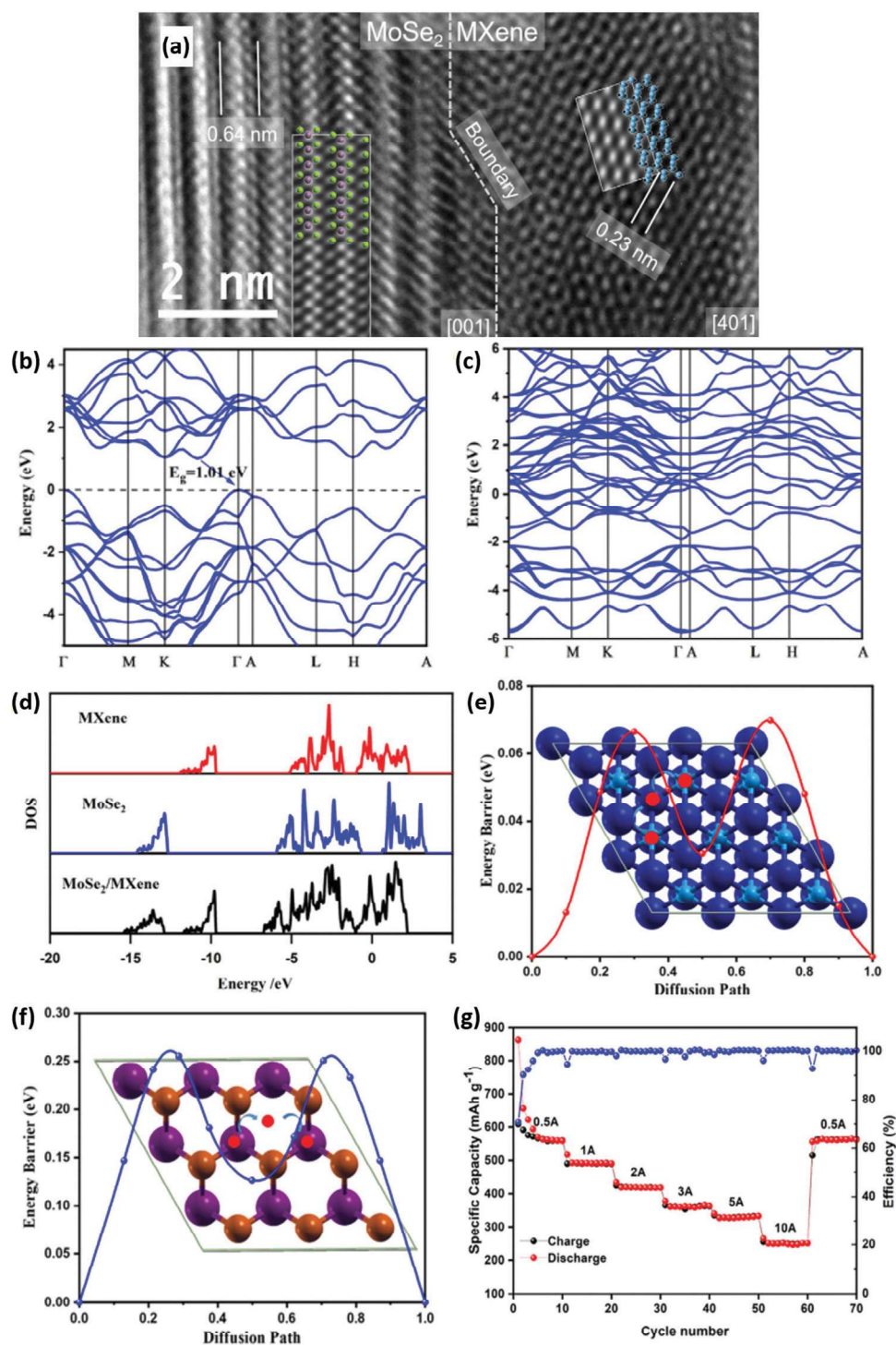


Fig. 15 (a) HRTEM image of the $\text{MoSe}_2/\text{Ti}_3\text{C}_2\text{T}_x\text{-MXene}$ heterointerface. Band structures of (b) MoSe_2 and (c) $\text{Ti}_3\text{C}_2\text{T}_x\text{-MXene}$. (d) The density of states of $\text{Ti}_3\text{C}_2\text{T}_x\text{-MXene}$, MoSe_2 and the $\text{MoSe}_2/\text{Ti}_3\text{C}_2\text{T}_x\text{-MXene}$ heterointerface. Energy diffusion pathways and calculated energy barrier of single Na^+ on (e) $\text{Ti}_3\text{C}_2\text{T}_x\text{-MXene}$ and (f) MoSe_2 . (g) Charge–discharge capacities of $\text{MoSe}_2/\text{Ti}_3\text{C}_2\text{T}_x\text{-MXene}$ at different cycling current rates. Reproduced with permission from ref. 241, copyrights reserved to Elsevier 2020.

(at the top and in the middle). Furthermore, the energy barriers of the synthesised $\text{MoSe}_2/\text{Ti}_3\text{C}_2\text{T}_x\text{-MXene}$ is 0.095 eV as against that of MoSe_2 (0.25 eV) and $\text{Ti}_3\text{C}_2\text{T}_x\text{-MXene}$ (0.066 eV), and thus, faster Na^+ transport and charge transfer. When evaluated as a potential electrode, very high reversible capacities were obtained

at different current densities (Fig. 15g) and a Coulombic efficiency (CE) of 99.8% was obtained, thus, highlighting that appropriate selection of materials and careful construction of heterointerfaces are critical for making 2D HSS highly functional for high energy and power batteries.

Recently, Wang *et al.* synthesised the NiCoAl-LDH/V₄C₃T_x HS using a hydrothermal method and investigated its performance as a battery-type electrode.²⁴² The resultant electrode delivered a specific capacity of 300 C g⁻¹ at a current density of 20 A g⁻¹ in 1 M KOH.²⁴² Moreover, when combined with AC in a full cell, high energy densities of 71.7 and 45 W h kg⁻¹ at power densities of 830 and 20 000 W kg⁻¹, respectively, were obtained, and the battery could dis/charge in only 8.1 s. Interestingly, it showed 98% capacity retention after 10 000 cycles when tested at 20 A g⁻¹. The synergistic effect of the faradaic redox properties of NiCoAl-LDH and the conducting properties of V₄C₃T_x coupled with the tuned interlayer spacing at the heterointerface in realising such high-power energy storage devices. The strength and stability of the heterointerface in 2D HS-based electrodes is another factor that could be improved for a longer life cycle and better performance. Strong interactions at the heterointerfaces between dissimilar materials may result in the formation of highly stable HSs with more charge redistribution, which can be achieved through covalent bonding. Direct covalent bonding not only brings the materials closer to harvest the benefits of the heterointerface but also help in quick charge transfer from one material to another. For example, Nakhanivej *et al.* developed face-to-face covalently bonded oBP/rGO (oxidised BP, oBP) *via* ozonation, vacuum filtration and thermal treatment.²⁴³ They reported that the presence of interfacial chemical bonds (C–O–P=O and C–P=O) is responsible for the strong interactions between rGO and oBP, and rapid charge transport. When investigated for potential usage as an electrode for energy storage applications, it was observed that the redox-active sites were confined to the heterointerface, storing 99% of the total stored charges at 2000 mV s⁻¹ with an ultrafast pseudo-capacitance mechanism. A specific capacitance of 478 F g⁻¹ at 1 A g⁻¹ with a rate capability of ~72% was obtained. In addition, a capacity retention of 91% was attained after 50 000 cycles, indicating exceptional stability. Moreover, the influence of interfacial strength on the structural stability and performance of Ti₃C₂T_x-MXene/CoAl-LDH synthesised *via* the electrostatic self-assembly method was also investigated.²⁴⁴ The 2D HS showed a volumetric capacity of 2472 C cm⁻³ and a rate capability of 70.6% at 20 A g⁻¹ in 3 M KOH. Further, when the Ti₃C₂T_x-MXene/CoAl-LDH 2D HS was tested as a cathode in a full cell with Ti₃C₂T_x-MXene/G as an anode, a high energy density of 85.4 W h L⁻¹ was obtained, along with good stability by retaining 94.4% of its performance after 30 000 cycles. This exceptional performance was attributed to the improved charge distribution and high structural stability through strong interfacial connections at the heterointerfaces.

Research on the usage of 2D HSs as a potential electrode possibly holds the key for better high power and energy density storage devices, but more research efforts are still required. Especially, the focus should be on selection of materials of suitable combinations, the role of the heterointerface, redox chemistry at the heterointerface, and electronic and ionic separation in the presence of an electrolyte at the heterointerface.

6.2 Bifunctional catalysts

The design and development of highly efficient and sustainable catalysts are always challenging, especially when it comes to

catalysts that simultaneously show high reaction kinetics in two separate reactions within an integrated electrolyser. For example, transition metal phosphides generally exhibit superior catalytic activity for HER but underperform for oxygen evolution reaction (OER).^{245–247} In contrast, TMOs and transition metal (oxy)hydroxides perform well for OER in alkaline media but exhibit poor HER performance.^{245,248,249} 2D HS based bifunctional catalysts are particularly promising for catalytic HER and OER in overall water splitting and oxygen reduction reaction (ORR) and OER in electrochemical energy technologies (*e.g.* metal–air batteries). Investigations of 2D HSs for use as bifunctional catalysts are still at their early stage, and there are only a few studies of 2D HSs for bifunctional catalysts dually and highly active towards both HER and OER or OER and ORR in a single system. Such a limited number of studies might be due to the lack of understanding and theoretical prediction of the behaviour of heterointerfaces in the presence of an electrolyte, the synthesis of a perfect heterointerface, and effective combination of individual constituents. Among 2D HSs bifunctional catalysts, transition metal sulphides^{227,250–254} are particularly popular as one of the materials of 2D HSs followed by engineered carbonaceous materials,^{12,255} transition metal phosphides,^{14,256} and MXenes.²⁵²

Bifunctional catalysts to produce hydrogen by overall water splitting based on 2D HSs take advantage of the unique properties of heterointerfaces which cannot be achieved by standalone materials. The overall water splitting catalytic reaction consists of two half-reactions, where hydrogen is produced at the cathode and oxygen is produced at the anode simultaneously in the same or different electrolytes. The theoretical water splitting potential is 1.23 V in standard conditions; however, practically, it requires a much higher potential. Such overpotential results from the sluggish kinetics of the OER/HER on the electrode surface. The OER is considered more kinetically sluggish than HER due to its four-electron transfer process. Although HER is a single-electron transfer process but the multi-step reaction that includes adsorption, reduction, and desorption processes makes it difficult to happen. In addition to intrinsic sluggish reaction kinetics, several vital factors such as active sites and electrical conductivity also determine the quality of catalysts. Noble metal-based materials are benchmarked as HER and OER catalysts, for example, platinum (Pt)-based materials are superior for HER, whereas iridium and ruthenium oxides (RuO₂ and IrO₂) are considered ideal for OER. Integrated IrO₂-Pt catalysts require 1.57 V for overall water splitting to achieve 10 mA cm⁻² current density.¹⁴ Considering the scarcity and associated cost of noble metal-based catalysts, the fundamental challenge is to develop low-cost, earth-abundant catalysts which have abundant active sites and superior electrical conductivity to make the overall process energy-efficient by reducing the overpotential. Therefore, the design and development of viable 2D HS catalysts with superior performances for both HER and OER at a reduced cost is of paramount importance.

The primary approach within HSs for bifunctional catalysts to improve the performance can be attained by combining two distinct materials into a HS by exploiting the HER active catalytic performance of one material and the OER active catalytic performance of the other.^{255,257} In such case, combined

synergies of several parameters such as heterointerface properties, superior conductivity, and electronic structure modulation through the surfaces, edges, and interfaces are considered key success factors for improving the overall system efficiency of 2D HSs. Inspired by the beneficial synergistic effects of two different 2D materials of 2D HSs, Yanna *et al.* developed a 2D HS of $\text{Co}_3\text{S}_4/\text{MoS}_2$ that consists of a MoS_2 nanosheet shell grown on the core of hollow Co_3S_4 by using a two-step synthesis.²⁵⁷ The unique morphology of $\text{Co}_3\text{S}_4/\text{MoS}_2$ shows excellent bifunctional catalytic performances owing to the HER active catalyst MoS_2 and the OER active catalyst Co_3S_4 in an acidic and alkaline electrolyte, respectively.

Modification of surfaces, edges, and interfaces can improve the catalytic properties for overall water splitting since electrochemical reactions mainly occur on the surfaces, on the edges, or at the interfaces of electrocatalysts.^{258,259} However, the heterointerface is considered most important for 2D HSs since the heterointerface not only acts as an electron transfer channel between individual materials but also provides an abundance of active sites.^{12,227} Rationally engineered defects and disorders at the heterointerface can promote the electron transfer and provide new active sites for boosting water splitting efficiency.²²⁷ For example, the rich sulphur defects and disorders due to the mismatch of $\text{MoS}_2/\text{NiS}_2$ at the heterointerface during the synthesis process can improve the binding ability of catalysts with H atoms.²²⁷ Such defects and disordered structure at the heterointerface can facilitate the reduction of electron density around Ni atoms and boost HER performance. Within the same structure, the transformation of metal sulphides to oxides/hydroxides promotes the OER process. Interestingly, the heterointerface induced structural phase transformation (*e.g.* 2H to 1T) or the use of a mixed structural phase (*e.g.* 1T/2H) within HSs is also proven effective to improve the overall water splitting performance compared to individual 2D materials.^{250,252}

The heterointerface can also be synergised with light-induced photoelectrons to enhance the overall water splitting performance. In such an instance, the heterointerface introduces new active sites through the optimisation of the electronic structure while the photoelectrons produced by the photo-excited components further accelerate the redox kinetics.^{33,260,261} For example, a 2D HS of Ni_3S_2 edged with MoS_2 synthesised by the one-pot hydrothermal method offers both unique structure and improved bifunctional catalysis in the presence of solar light.³³ The photo-generated charge transfer from the photo-excited Ni_3S_2 to the Mo–S–Ni covalent heterointerface favours the chemisorption of hydrogen and oxygen-containing intermediates at the heterointerface resulting in the acceleration of redox kinetics. Based on this mechanism, the full water splitting cell voltage was reduced to 1.5 V@1 sun irradiation, while it was 1.53 V without the presence of solar light.

Notably, carbonaceous materials or MXene as one of the materials of the HS not only serve as highly conductive media to enhance the charge transferability and prevent the aggregation of pairing materials for long term functionality^{252,259} but also significantly contribute to the active sites in the presence of specific dopants or defects.^{255,262,263} As such, functional/engineered, metal-free carbonaceous materials/HSs are promising in achieving a

performance close to that of noble metals. For example, modulation of electronic configuration along with a carefully designed heterointerface between liquid-phase exfoliated BP (EBP) nanosheets and NG yields a highly active bifunctional catalyst with cell voltage as low as 1.54 V@10 mA cm^{-2} for overall water splitting in alkaline media.¹² The 2D HS of EBP/NG was prepared by the assembly of EBP onto the surface of NG exploiting the oppositely charged electrostatic interaction. A KPFM measurement was performed to reveal the relative position of the Fermi level between EBP and NG. KPFM revealed that the work functions of EBP and NG are ~ 4.7 eV and ~ 4.5 eV, respectively, meaning the lower position of the Fermi level of EBP compared to that of NG (Fig. 16a). Therefore, such a difference in the Fermi level between the individual constituents of a 2D HS favours charge redistribution due to the electron migration through the heterointerface from NG to EBP (Fig. 16b). As illustrated in Fig. 16c, the computational differential charge density of the EBP/NG 2D HS further validates the electron and hole enriched EBP and NG, respectively. The low HER overpotential of EBP/NG is probably due to the electron enrichment of EBP from NG by electron injection through the heterointerface which accelerates the H adsorption over the surfaces of the catalyst (Fig. 16d and e). Concurrently, the charge transfer from NG due to N doping and formation of a HS can generate positively charged carbon sites across the heterointerface which is highly favourable for high OER activity (Fig. 16f and g).

In general, transition metal phosphides are considered superior for both HER and OER than their corresponding transition metal compounds (*e.g.* oxides, sulphides, nitrides). For instance, overall water splitting performance can significantly be improved when only transition metal phosphides¹⁴ are used in 2D HSs instead of the combination of the transition metal sulphide and phosphide.²⁵³ The 2D HS of $\text{FeP}/\text{Ni}_2\text{P}$ was reported as one of the best bifunctional catalysts among water alkaline electrolyzers which required only 1.42 V to achieve 10 mA cm^{-2} for overall water splitting. $\text{FeP}/\text{Ni}_2\text{P}$ has also proven outstanding in energy efficiency, which delivered a high current density of 1500 mA cm^{-2} at less than 1.85 V cell voltage.¹⁴ Theoretical calculations suggested that the most active facet (001) of FeP was exposed during the formation of $\text{FeP}/\text{Ni}_2\text{P}$ HSs, which probably reduced ΔG_{H} significantly. Such reduction of ΔG_{H} in $\text{FeP}/\text{Ni}_2\text{P}$ contributed strongly to high HER activity and resulted in an overpotential of only 14 mV@10 mA cm^{-2} . The ΔG_{H} of the FeP(001) facet is only 0.06 eV while the Ni_2P (001) facet has relatively strong ΔG_{H} (0.306 eV). The synergistic effects of constituting materials, fast electron transport, and the presence of oxidised species at the surface accelerated the OER process at the $\text{FeP}/\text{Ni}_2\text{P}$ anode and required only 154 mV overpotential to deliver 10 mA cm^{-2} .

Apart from water splitting, the engineering of heterointerfaces is also beneficial to address some of the critical issues which are hindering the practical applications of electrochemical energy technologies. In this regard, ORR and OER are the two most important reactions of metal–air batteries. However, the sluggish kinetics of ORR and OER in the discharging and charging processes, low initial/rate capability, and poor cycle life are considered main obstacles for the efficient development of

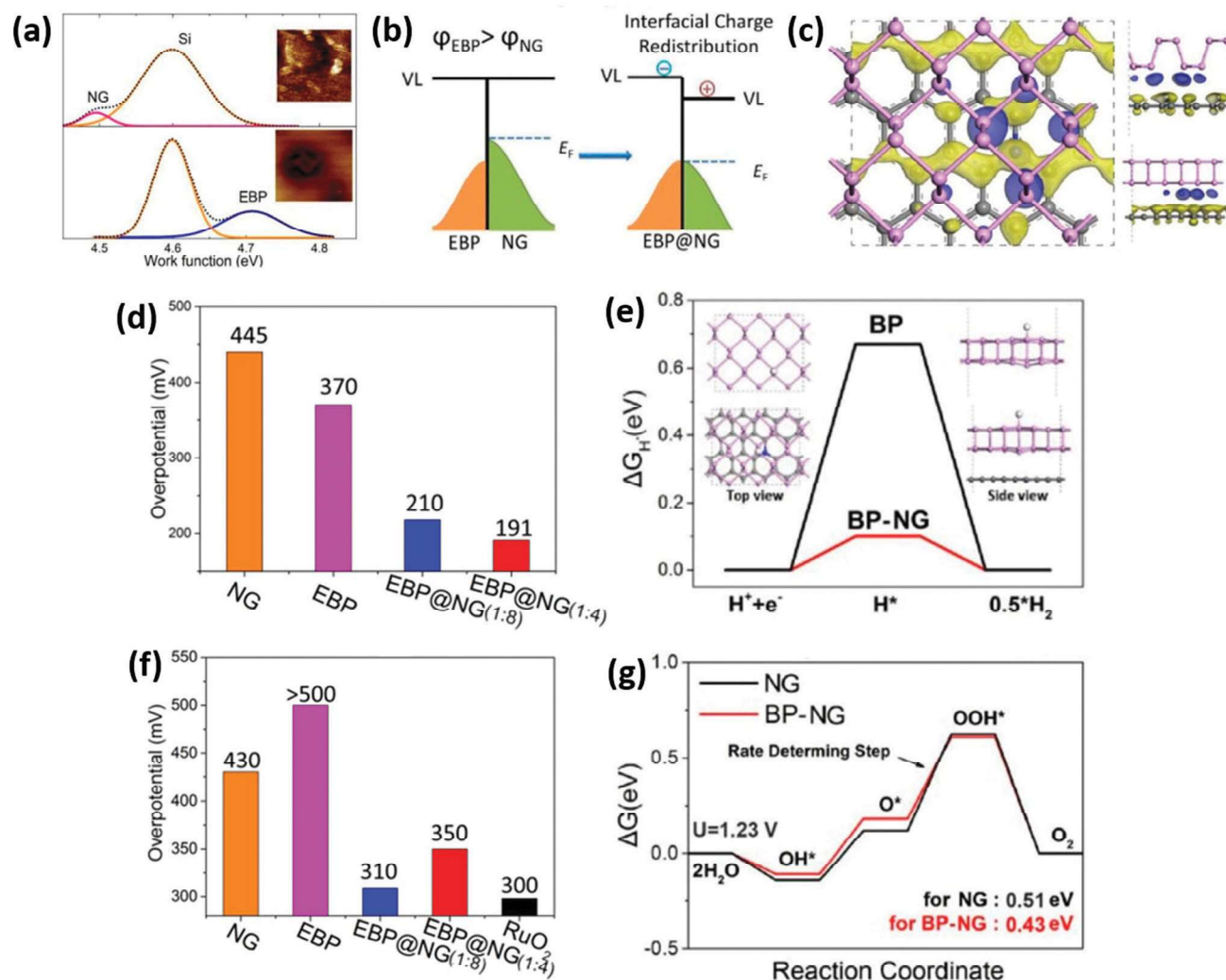


Fig. 16 (a) Work function measurements of NG and EBP using KPFM show that EBP has a higher work function than NG; hence the Fermi level position of EBP is lower than that of NG. (b) Interfacial charge redistribution occurs between EBP and NG at the heterointerface due to the mismatch in the Fermi level position of EBP and NG. (c) The illustration of differential charge densities at NG and EBP regions, where blue and yellow are electron rich regions, respectively. (d) Low HER overpotential of EBP/NG at 10 mA cm⁻² due to the low hydrogen adsorption free energy (ΔG_{H^*}) of HS, as shown in (e). (f) Low OER overpotential of EBP/NG at 10 mA cm⁻² due to the formation of a key intermediate (hydroperoxy species, OOH*) for oxygen evolution as shown in (g). Reproduced with permission from ref. 12, copyrights reserved to American Chemical Society 2019.

such technologies. Therefore, similar to water splitting, inexpensive oxygen catalysts are highly desirable, which have both high OER and ORR activities to achieve better metal-air battery performances. CoO is known to have good ORR activity whereas CoP shows good OER activity. However, the combined structure of CoO and CoP in the form of a 2D HS is not only highly active for both ORR and OER but exceeds the performance of individual constituents. Such enhancement of performance is believed to be from the interpenetration of O-P species (Fig. 17a) at the heterointerface which improves electron transfer, conductivity between constituting layers and boosts the activity of both OER and ORR (Fig. 17b).²²⁵ Activation of both OER and ORR in the 2D CoO/CoP HS also enhanced the initial capacity, rate capability, and cycle performance of Na-O₂ metal-air batteries.

Furthermore, engineering of composition/structure or both within 2D HSs is also an effective approach to improve the electrocatalytic properties.^{256,264} For example, manipulating

the structural composition at the heterointerface of NiFe₂O₄/FeNi₂S₄ to improve the catalyst surface binding energy with oxygenated species can accelerate the reaction kinetics of both ORR and OER.²⁶³ The NiFe₂O₄/FeNi₂S₄ HS catalyst was prepared by a hydrothermal approach, followed by oxidation and partial sulphidation. It is known that the weak oxygen adsorption energy (E_o) makes the reaction kinetics stronger and DFT calculations revealed that the heterointerface formed through the (311) plane between NiFe₂O₄ and FeNi₂S₄ (Fig. 18a) has the most enhanced oxygen electrocatalytic properties due to the lowest E_o compared to only NiFe₂O₄ or FeNi₂S₄ (Fig. 18b). Such enhancement is attributed to the adsorption of oxygen on the Ni surface at the heterointerface, as illustrated in the differential charge density of the interfacial model (Fig. 18c). As a result, the NiFe₂O₄/FeNi₂S₄ HS improved both OER (overpotential of 429 mV@10 mA cm⁻²) and ORR (onset potential of 0.715 V) than either NiFe₂O₄

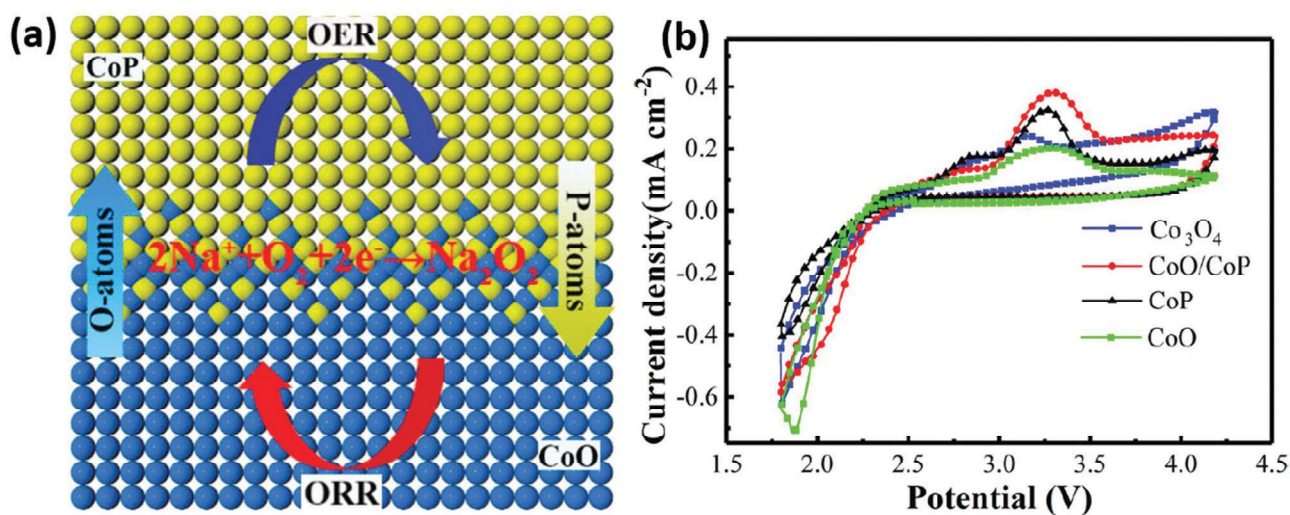


Fig. 17 (a) Interpenetration of O–P at the heterointerface of CoO/CoP 2D HSs facilitates conductivity improvement and electron transfer which enhances the ORR and OER activities. (b) ORR and OER performance measurements by cyclic voltammetry curves. Reproduced with permission from ref. 225, copyrights reserved to American Chemical Society 2018.

or FeNi₂S₄ in a neutral electrolyte (Fig. 18d). Moreover, the HS used as a Zn–air electrode can deliver high power density (44.4 mW cm⁻² as shown in Fig. 18e) while maintaining stability for 900 discharging/charging cycles in neutral media (Fig. 18f).

The oxygen vacancy-rich In-doped 2D porous CoO/CoP HS is an ideal example of both composition and structure engineered electrocatalysts for rechargeable Zn–air batteries. Vacancy-rich doped CoO/CoP was developed in three simple steps: initially, In–Co-layered double hydroxides were prepared by the solvothermal method in the presence of hydrogen peroxide followed by oxidation and phosphorisation. The oxygen vacancies at the heterointerface of the 2D HS were introduced by the •OH free radical in the initial solvothermal step and enhanced by the oxidation process. Such engineering of the composition and structure of CoO/CoP shows high ORR activity (onset potential of 0.94 V) and OER activity (overpotential of 365 mV@10 mA cm⁻²) in alkaline media. Furthermore, an air cathode composed of a 2D HS exhibited large power (139.4 mW cm⁻²), high energy density (938 W h kg_{Zn}⁻¹), and excellent cycling stability which was superior to that of Pt/C–RuO₂ for Zn–air batteries. The detailed HER and OER or ORR and OER performance parameters of 2D HS bifunctional catalysts are summarised in Table 1.

Even though considerable advances have been made in exploring 2D HSs for creating bifunctional catalysts, many challenges still exist for the development of high performing bifunctional catalysts. For example, the majority of studies on 2D HSs for bifunctional catalysts have been carried out in alkaline electrolytes, while stable and durable 2D HS catalysts which are highly active in acidic media are needed for many practical applications. Carbon-based materials have a strong tolerance to both acidic and basic media; therefore, functionalisation and loading co-catalysts on carbon-based materials can provide abundant reaction sites and improved conductivity while being resistive to electrolytes. Such incorporation of carbon-based materials should be further investigated in 2D

HSs. Other 2D materials can also offer different capabilities in terms of durability and adjusting the heterostructure properties. In this regard, the basal and boundary contacts play important roles, and trade-offs between the performance and stability should be studied. The next challenge is the low-throughput of well-defined heterointerfaces formed by two dissimilar materials using gas and vacuum-based synthesis methods. Therefore, alternative synthesis methods which can construct well-defined heterointerfaces by high-throughput solution-based approaches need to be developed. Besides synthesis methods, manipulation of heterointerface chemistry is another critical challenge as it requires balancing several material features such as exposing the maximum number of active sites, enhancing ion mass transport (electrolyte penetration) and improving electronic conductivity without compromising the stability. Considering this, the creation of heterointerfaces through covalent bonding helps in tuning such properties but their mechanisms of action yet need to be completely understood. The direct bonding between two materials may influence the mass transport negatively, while adding linkers may impact the conductivity or stability; therefore, the balance between these factors also needs to be investigated. The theoretical studies and *in situ* characterisation can help in understanding the role of heterointerfaces and unveil the underlying mechanisms for the development of effective 2D HSs. For instance, DFT provides predictions to identify the active species and optimise the catalysts at the molecular levels. However, more efforts are required to identify the exact catalytic/reaction mechanisms at heterointerfaces in the presence of ions/electrolytes/solvents. Moreover, the development of *in situ* microscopy/spectroscopy characterisation techniques is crucial to explore and discover the state/morphology modulations and mechanisms of catalysts during reaction processes.

6.3 Physical and chemical sensors

6.3.1 Gas sensors. Heteroarchitectures provide innumerable heterointerfaces that enhance gas sensing abilities.^{267,268}

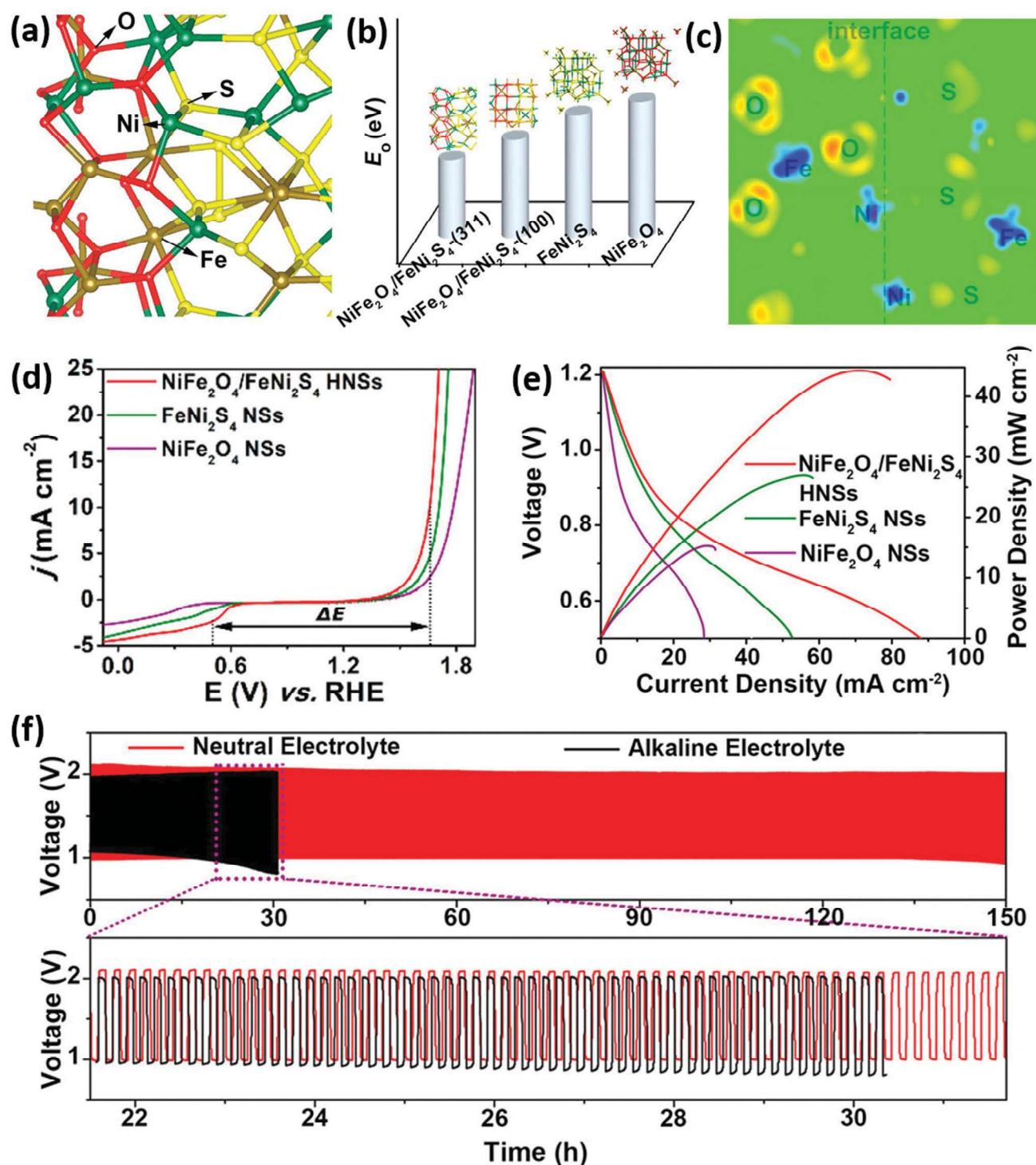


Fig. 18 Panels (a–c) are obtained from the computational model. (a) Interface model of oxygen adsorption geometry at the (311) planes of NiFe₂O₄/FeNi₂S₄. (b) The oxygen adsorption energy (E_o) comparison between different catalysts. (c) Differential charge density of the (311) facets of the heterointerface between FeNi₂S₄ and NiFe₂O₄ where an increase in electron density is marked by red/yellow regions and a decrease in electron density is marked by blue regions. (d) The LSV polarisation curves of catalysts for both ORR and OER. (e) The discharge polarisation and the corresponding power density curves of catalysts of Zn-air batteries in neutral media. (f) Long-term cycling performance at 0.5 mA cm⁻² of Zn-air batteries made from NiFe₂O₄/FeNi₂S₄ shows the stable performance of the catalyst in the neutral media. Reproduced with permission from ref. 264, copyrights reserved to American Chemical Society 2018.

Notably, certain intrinsic limitations of standalone 2D materials (such as incomplete desorption and high signal to noise ratio) hinder the gas sensing performance that can be overcome by

forming heterointerfaces.^{267,269} First principles studies revealed that strong and weak interactions of gas molecules with a material's surface depend heavily on their adsorption energies^{270–272}

Table 1 Performance comparison of different 2D HS based bifunctional catalysts

Catalysts	Substrate	Synthesis method	HER overpotential (mV) @10 mA cm ⁻²	OER overpotential (mV) @10 mA cm ⁻²	Water splitting potential (V) @10 mA cm ⁻²	Tafel slope (HER) (mV dec ⁻¹)	Tafel slope (OER) (mV dec ⁻¹)	Electrolyte	OER onset-potential (V)	Catalyst loading (mg cm ⁻²)	Ref.
FeP/Ni ₃ P	NF	CVD	14	154	1.42	24.2	22.7	1 M KOH	—	8	14
Iron-cobalt layered double hydroxide/graphdiyne	NF	Hydrothermal	43	216	1.43	98.9	43.6	1 M KOH	—	—	265
Ni-Fe hydroxide/defective G	GCE	Electrostatic self-assembly	300	210	1.43 ^a	110	52	1 M KOH	—	0.28	255
MoS ₂ /NiCoS	GCE (HER, OER), NF (overall)	Solventothermal	189	290	1.50	75	77	1 M KOH	—	0.14 (HER, OER), 3 (overall)	266
Ni ₃ S ₂ /MoS ₂	NF	Hydrothermal	78	260	1.53	68	59	1 M KOH	—	—	33
BP/NG	GCE	Electrostatic self-assembly	125 (1:4 ratio)	265 (1:8 ratio)	1.54	76	89	1 M KOH	—	0.3	12
NiS/G	CC	Pyrolysis + sulphidation	70	300	1.54	50.1 (1:4 ratio)	55.8 (1:8 ratio)	1 M KOH	—	2.4	254
MoS ₂ /NiS ₂	CC	Hydrothermal + sulphurisation	62	278	1.59	50.1	91.7	1 M KOH	—	—	227
MoSe ₂ (1T/2H)/MXene	NF	Hydrothermal	95	340	1.64	91	90	1 M KOH	—	2-3	252
NiS/Ni ₃ P	CC	Hydrothermal + sulphurisation + phosphorisation	111@20	255@20	1.67	78.1	41.3	1 M KOH	—	—	253
Pd decorated MoS ₂ /rGO	GCE	Solventothermal + chemical reduction	86	245	—	35.9	42	1 M KOH	—	0.35	250
Co ₃ S ₄ /MoS ₂	GCE	Hydrothermal	~210	310	—	88	59	0.5 H ₂ SO ₄ (HER), 1 M KOH (OER)	—	0.283	257
MoN/C@MoS ₂	GCE	Self-assembly + hydrothermal + carbonisation	117	390	—	64.3	72	1 M KOH (HER), 0.1 M KOH (OER and ORR)	0.90	0.196	251
NiFe ₂ O ₄ /FeNi ₂ S ₄	CFP, RRDE with a Pt ring, GCE	Hydrothermal + oxidation + sulphidation	—	429	—	—	—	0.2 M PBS	0.715	—	264
CoO/CoP	CP	Hydrothermal + phosphatation	—	—	—	—	—	0.5 M NaTFSI	—	1.66	225
Oxygen vacancy-rich in-doped CoO/CoP	RDE	Solventothermal + oxidation + phosphorisation	—	365	—	—	—	0.1 M KOH	0.94	0.250	256

Nickel foam (NF), glassy carbon electrode (GCE), carbon cloth (CC), carbon fibre paper (CFP), rotating ring-disk electrode (RRDE). ^a Calculated from the graph at 10 mA cm⁻².

Table 2 Comparative gas sensing performances of different 2D HSs to highlight the role of the heterointerface

Sensing structure	Synthesis method	Target gas	Detection limit (ppm)	Exposure/purging time	Concentration (ppm)	Response (%)	Temperature and conditions	Ref.
G/MoS ₂	Mechanical exfoliation + CVD + dry transfer	NO ₂	1.2	5/30 min	5	~9	150 °C	277
G/MoS ₂ FET	Mechanical exfoliation + CVD + dry transfer	NH ₃	5	—	100	~4	150 °C	278
BP/h-BN/MoS ₂ FET	Mechanical exfoliation + CVD + dry transfer	NO ₂	—	—	1	>10 ³	Room temperature (RT)	281
BP/h-BN/MoS ₂ FET	Mechanical exfoliation + dry transfer	NO ₂	0.01	—	0.1	120	RT	281
g-C ₃ N ₄ /SnS ₂	Solvothermal	NO ₂	0.1256	—/166 s	1	503	RT	13
Sn _{0.5} W _{0.5} S ₂ /SnS ₂	Hydrothermal	Acetone	0.1	—	10	~8	RT	283
Ti ₃ C ₂ T _x /WSe ₂	Electrostatic self-assembly	Ethanol	1	9.7/6.6 s	40	~9	RT	284
rGO/MoS ₂	Ultrasonication assisted mechanical interaction	H ₂ O (50% RH)	5%	6.3/30.8 s	85%	2494.25	RT	285
ZnO/g-C ₃ N ₄	Ultrasonic mixing + calcination	NO ₂	1	142/190 s	7	44.8	RT, 460 nm, 12.7 W m ⁻²	286
g-C ₃ N ₄ /rGO	LbL self-assembly	NO ₂	0.1	138/318 s	2	110	RT	287
BP/MoSe ₂	Dry transfer	SO ₂	2	140/130 s	2	~3	RT, 365 nm	288
BP/MoSe ₂	Dry transfer	NO ₂	0.025	5/2 min	0.025	10.5	RT	288
g-C ₃ N ₄ /rGO	Ultrasonication assisted self-assembly	NO ₂	0.6	—	5	~30	150 °C	289
NbSe ₂ /WSe ₂	One-step CVD	NO ₂	0.12	—	5	~35	—	290
WSe ₂ /MoS ₂	Dry transfer	NO ₂ , TNT	0.15	6.4/2.9 min	0.5	45	RT	291
G/WS ₂ /G	Dry transfer	NO ₂	1	360 s/—	30	~20	300 °C	292
G/h-BN/G	Dry transfer	NO ₂	—	—	40	~10	300 °C	292
rGO/CuO	LbL self-assembly	CO	0.25	70/160 s	1	2.56	RT	293

which in turn alter their electrical properties.²⁷³ Changes caused by the adsorbent (alien materials) and the adsorbate (gas analytes) interaction due to the synergistic effect at the heterointerface provide superior sensing performance when compared to their individual counterparts.²⁷⁴ Table 2 lists the sensing performances of various 2D HSs devised for gas sensing applications.

Graphene has been well known as one of the most reliable materials for the fabrication of electrodes in chemical sensing.^{275,276} Combining TMDs with graphene electrodes not only preserves their ultrathin feature but also facilitates effective charge transfer at their heterointerface. For instance, the gas sensor device made of G/MoS₂ on the flexible polyimide (Fig. 19a) displayed a highly stable and reproducible response to NO₂ (Fig. 19b) which paves the way for wearable gas sensing applications.²⁷⁷ Tabata *et al.* also devised a G/MoS₂ based field effect transistor (FET) with an added feature of a gas barrier (Fig. 19c).²⁷⁸ The gas barrier passivated the graphene uncovered MoS₂ which enabled precise control of the Schottky barrier height. Unlike a metal–MoS₂ interface, the 2D HS based G/MoS₂ heterointerface is extremely sensitive to its charge carrier density, allowing effective electrostatic tuning of the Schottky barrier height at the heterointerface. Characteristics such as availability of absorption sites at proximity to the heterointerface and weak-Fermi level pinning at the heterointerface which cannot be obtained from a metal–semiconductor based gas sensor can easily be achieved through the formation of 2D HSs. This leads to a substantial gain in resistance that corresponds to a value greater than 10³ upon exposure to 1 ppm of NO₂, under a reverse bias condition (Fig. 19d).²⁷⁸ Motivated by these results, a DFT study based on G/hBN reveals a substantial variation in the adsorption energies of both NO and NO₂ gas molecules with respect to their position on the HS surface.²⁷⁹ BP, a strong competitor to graphene, has shown effective Fermi level modulation upon adsorption to gas molecules.^{273,275,280} With BP

(top gate)/h-BN (interfacial layer)/MoS₂ (conduction channel), effective modulation in the Fermi level of both BP and MoS₂ has been observed.²⁸¹ A change in channel conductance under the influence of drain and gate bias enables the 2D HS to detect concentrations as low as 3.3 ppb of NO₂.

Gas sensors operating at high temperatures hinder the practicability of operation; therefore, a gas sensor working at room temperature is essential to reduce the operating cost and design complexity. For example, pristine 2D materials like SnS₂ can sense gas molecules only at a high temperature.²⁸² To make SnS₂ workable at room temperature, it can be coupled with g-C₃N₄ nanosheets which offers large interfacial contact with more active sites for adsorption of NO₂.¹³ The difference in the work function potential between the materials aids a highly favourable Fermi mediated charge transfer from g-C₃N₄ to SnS₂ that enables detection concentrations close to 1 ppm of NO₂. Additionally, desorption of NO₂ molecules with a recovery time as short as 166 s has been observed due to the increased mobility and reduced activation of charge carriers from g-C₃N₄. The obtained performance is indeed higher (change in response of 503%) and faster compared to that of pristine SnS₂ gas sensors. However, to make SnS₂ workable in the ppb range of detection, Wang *et al.* developed a 2D HS by adding a metallic element to SnS₂ which displayed striking gas sensing abilities.²⁸³ By synthesising Sn_{0.5}W_{0.5}S₂ nanosheets on SnS₂ nanoplates, an ohmic-like contact was observed at the heterointerface which facilitated rapid charge transfer when exposed to acetone concentrations as low as 100 ppb at room temperature (Fig. 19e). A remarkable improvement in the specific area from 6.25 to 11.37 m² g⁻¹ and a 35 times reduction in the background noise with improved sensitivity were observed in this 2D HS (Fig. 19f).

The effective charge transfer properties of Ti₃C₂T_x MXene^{294,295} when combined with the availability of abundant active sites in

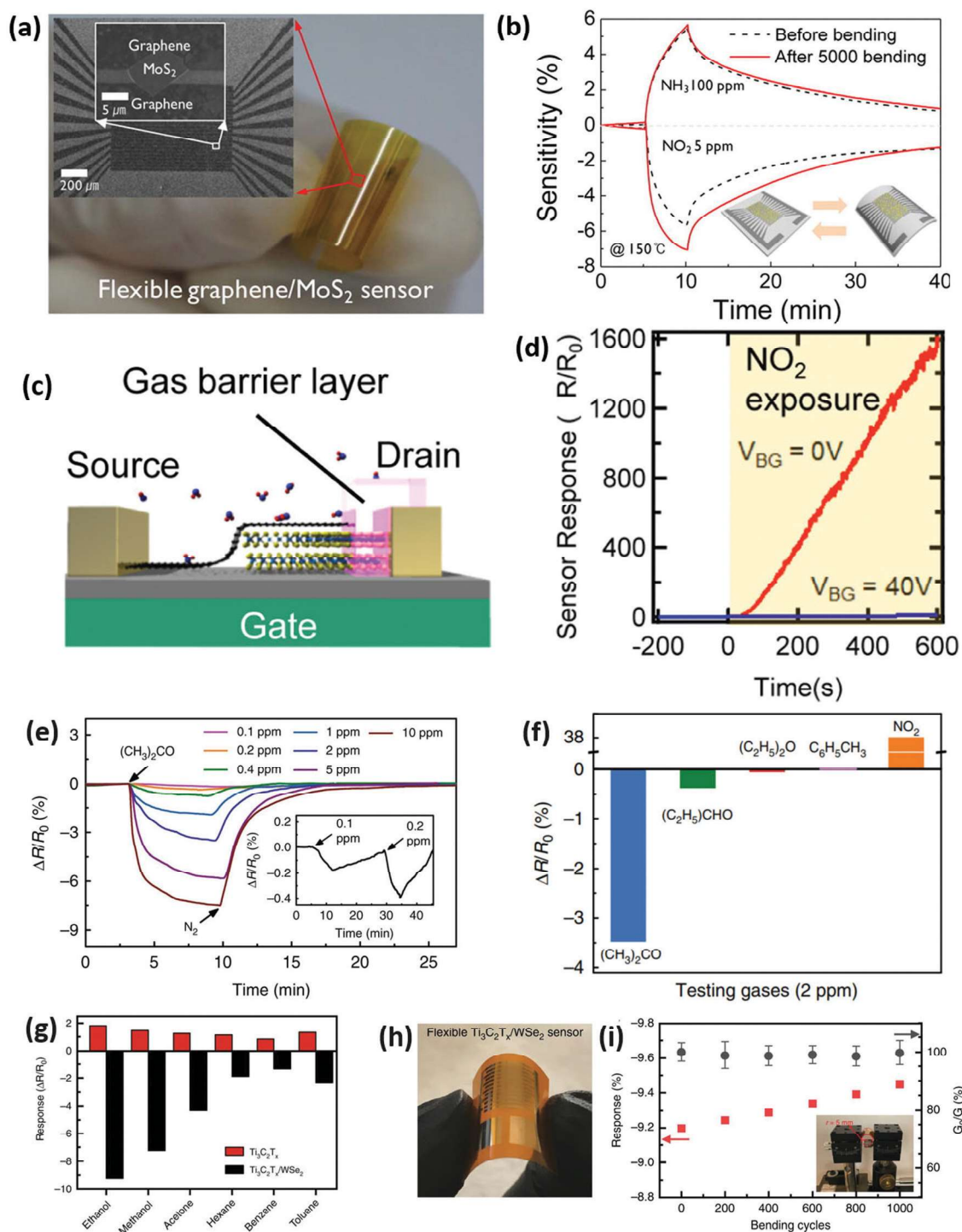


Fig. 19 2D HSs for gas sensing. (a) Optical image of a G/MoS₂ heterostructured device on a bent polyimide substrate. (b) Comparison of the gas response characteristics of the flexible heterostructured device before/after the bending cycle test; (inset) 3D schematic images showing the bending test condition. No serious performance degradation was observed even after performing 5000 bending cycle tests. The gas-sensing tests were performed at 150 °C. According to the material specification of the polyimide substrate film used, the temperature range from −269 to 400 °C is acceptable for its applications, which indicates that our annealing condition does not degrade the polyimide flexible film seriously. Reproduced with permission from ref. 277, copyrights reserved to American Chemical Society 2015. (c) Schematic of the G/MoS₂ HS device with a gas sensing barrier. (d) Time-dependent sensor responses of the G/MoS₂ HS under different gate voltages ($V_{BG} = 0$ and 40 V) in a linear scale. Reproduced with permission from ref. 278, copyrights reserved to American Chemical Society 2018. (e) Response–recovery curves of a typical chemiresistive sensor fabricated from Sn_{0.5}W_{0.5}S₂/SnS₂ HSs in response to acetone gas with increasing concentrations. Inset: Zoom-in response of the sensor towards 0.1 and 0.2 ppm acetone. (f) Comparison of the responses of the Sn_{0.5}W_{0.5}S₂/SnS₂ sensor towards different gases, including acetone, diethyl ether, propanal, toluene, and NO₂. Reproduced with permission from ref. 283, copyrights reserved to Springer Nature, 2018. (g) Selectivity test of the Ti₃C₂T_x and Ti₃C₂T_x/WSe₂ sensors upon exposure to various volatile organic compounds at 40 ppm. (h) Photograph of a flexible Ti₃C₂T_x/WSe₂ nanohybrid sensor. (i) Changes in ethanol sensing response and electrical conductance as a function of bending cycles. Reproduced with permission from ref. 284, copyrights reserved to Springer Nature 2020.

WSe₂ display a 12-fold increase in detecting 40 ppm of ethanol compared to pristine WSe₂ and Ti₃C₂T_x (Fig. 19g). The high noise level (~1.008%) and sheet resistance (26.3 ± 5.2 MΩ) from WSe₂ were alleviated to 0.15% and 3.3 ± 0.5 kΩ upon the formation of the 2D HS which also improved the response and recovery times of 9.7 s and 6.6 s. Additionally, the catalytic effect of the hybrid structure resolved the issue of incomplete desorption faced by pristine Ti₃C₂T_x. Devising the 2D HS on polyimide (Fig. 19h) displayed 1000 cycles of bending without performance degradation, thus demonstrating good flexibility and mechanical strength (Fig. 19i).

Light-activated gas sensing is also one of the conducive strategies that enable improved gas sensing performances,²⁹⁶ where improvements in the mobility of charge carriers along with a faster response and recovery time have been observed.^{297,298} In a different approach, Zheng *et al.* reported a NO₂ gas sensor by stacking multilayer p-type MoS₂ on a monolayer n-type MoS₂.²⁹⁹ The fabricated 2D HS displayed a 60 times improved response (in comparison to pristine p-type MoS₂) upon exposure to 20 ppm of NO₂ under the illumination of a 395 nm LED source. The energetic photons from UV enable effective extraction of electrons from the material, which increases its Schottky barrier height from 0.532 eV in the dark to 0.511 eV in light.²⁹⁹ Lack of the interfacial layer makes it difficult to obtain such performances from pristine or bulk materials. In another attempt, Wang *et al.* developed a gas sensor based on g-C₃N₄ nanosheets and ZnO, by subjecting the device to visible light.²⁸⁶ As a photosensitizer, g-C₃N₄ facilitated maximum absorbance from visible light that allowed surplus charge carriers to be transferred onto the surface of ZnO *via* the heterointerface for the detection of NO₂ concentration as low as 38 ppb (Fig. 20a).²⁸⁶ The concept of selective gas sensing by light activation and deactivation has been introduced by using g-C₃N₄/rGO.²⁹² The 2D HS displayed p-type properties with high selectivity to NO₂ and no response to SO₂ in the absence of light at room temperature (Fig. 20b). Interestingly, in the presence of light, the device displayed n-type semiconducting characteristics with the ability to detect 2 ppm of SO₂ at room temperature. Photon assisted gas sensing facilitated the effective separation of carriers while passing *via* the potential barrier of the heterointerface. Weakly adsorbed SO₂ before light irradiation gained enough momentum to extract carriers after irradiation, thereby modulating the photo-carrier density at the heterointerface (Fig. 20c). The demonstrated “light on–off strategy” using a 2D HS paves the path for practical light-sensing applications.

Very recently, Lee *et al.* devised a self-powered gas sensor made of a Gr/WS₂/Gr vdW HS.³⁰⁰ Adsorption and desorption of gas molecules were supported by a built-in electric field due to the electrochemical potential difference generated at the heterointerface. With this technique, H₂ gas sensing with concentrations as low as 1 ppm was detected at room temperature. Interestingly, selective gas sensing was also observed here with a polarity dependent change in electrical parameters where the response becomes positive (negative) upon exposure to NO₂ (H₂ or NH₃).³⁰⁰ Kim *et al.* also recently attempted a self-powered gas sensor with WSe₂(p-type)/WS₂(n-type) and MoS₂ (n-type)/WSe₂

(p-type) HSs. Under white light illumination, the WSe₂ and MoS₂ surface of each HS displayed maximum selectivity towards 10 ppm of NO₂ and NH₃ showing a response of 178% and 62%, respectively, without the application of an external bias.³⁰¹ DFT results indicated that the sensing performance was also influenced by the WSe₂ counterpart of the MoS₂/WSe₂ 2D HS. However, it is felt that further examination is imperative to understand this behaviour.

From the above analysis, it is seen that when 2D HSs are subjected to various techniques, they provide improved gas detection abilities. Performances obtained on flexible substrates and the recent discovery of self-powered gas sensing show breakthrough towards realising the Internet of Things (IoT) based sensors. Though certain materials like MXenes have attained considerable progress in gas sensing in their pristine state, it is felt that the heterostructuring concept is still in its early stages of exploration. As most of the HSs have focused on only NO₂ and NO_x based gas detection, there is a need to shift paradigms and inspect detection of other hazardous gases such as H₂S, CO and CO₂ as well. Comprehensive research about the interfacial properties of 2D HSs could help to achieve desired selectivity and sensitivity for these gases and lead to more research opportunities in this field.

6.3.2 Biosensors. The ultrathin feature of 2D materials holds promising properties of ultra-high sensitivity towards bioanalytes, making them highly desirable candidates for biosensing applications.^{302,303} Materials with such affluent properties, when brought together to work as a single entity, provide remarkable biosensing performances with promising functionalities.³⁰² For example, having shown reasonable response towards DNA^{304,305} (and recently virus³⁰⁶) detection, 2D MoS₂ suffers from instability and degradation issues in both aqueous solution and ambient environment.³⁰⁷ However, such a problem has been mitigated by developing a 2D HS with the highly stable G/MoS₂ for label-free detection of DNA hybridisation.³⁰⁸ The synergistic effect is evident through a significant enhancement in PL intensity upon immobilisation of target DNA. Ultimately, G/MoS₂ delivered outstanding sensitivity that can sense DNA at concentrations as low as 1 aM.

2D HSs built onto metallic films are also seen as a potential approach towards DNA sensing. The technique commonly referred to as surface plasma resonance (SPR), which effectively captures even minute variations in the refractive index of stacked 2D HSs.^{309–311} Certain modified SPR techniques such as the localised surface plasma resonance (LSPR) and the photonic spin Hall effect (PSHE) have theoretically illustrated the ultra-sensitive detection capability of HSs towards bioanalytes. For example, the G/MoS₂ proposed by El Barghouti *et al.* illustrated single stranded DNA (ss-DNA) detection with sensitivity as high as 403 nm per RUI (Fig. 21a).³¹² Similarly, Li *et al.* demonstrated that graphene stacked on MoS₂ causes spin-dependent variations due to the changes in the material's refractive index upon adsorption of biomolecules.³¹³ As most 2D biomolecular recognition elements display a high refractive index,^{314,315} combining these materials into 2D HSs ensures better sensing abilities.

Besides detecting DNAs, 2D HSs have also been illustrated for stretching a DNA. Stretching double-stranded DNA (ds-DNA)

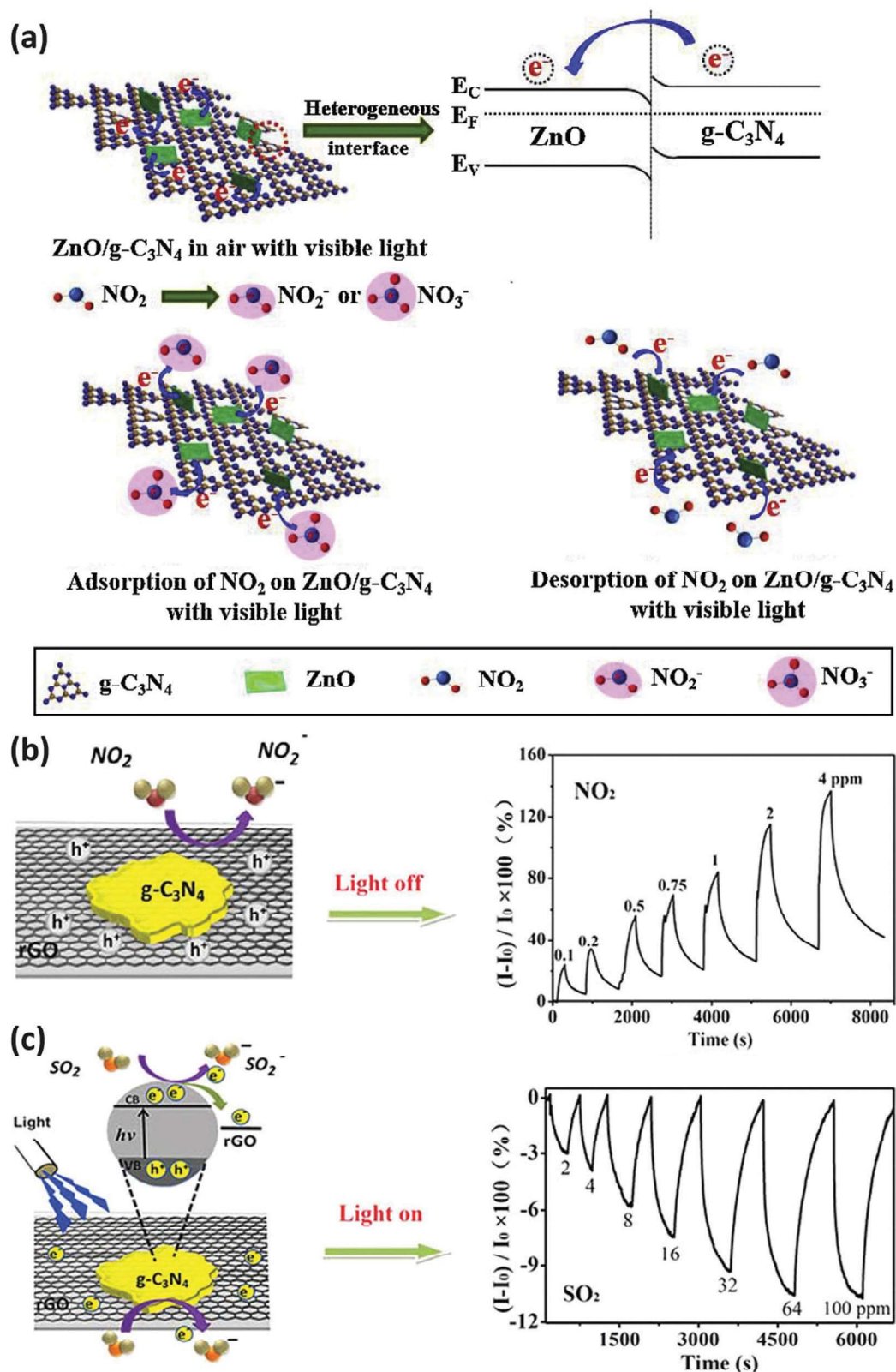


Fig. 20 Light-activated gas sensing in 2D HSs. (a) Schematic illustration of the electron transfer process in the sensing reaction of ZnO/g-C₃N₄. Reproduced with permission from ref. 286, copyrights reserved to Elsevier 2020. (b) Schematic illustration of the NO₂ detection mechanism on a multilayer g-C₃N₄/rGO sensor without light irradiation. (c) Schematic illustration of the SO₂ detection mechanism on a multilayer g-C₃N₄/rGO sensor with UV light irradiation. Reproduced with permission from ref. 287 copyrights reserved to American Chemical Society 2017.

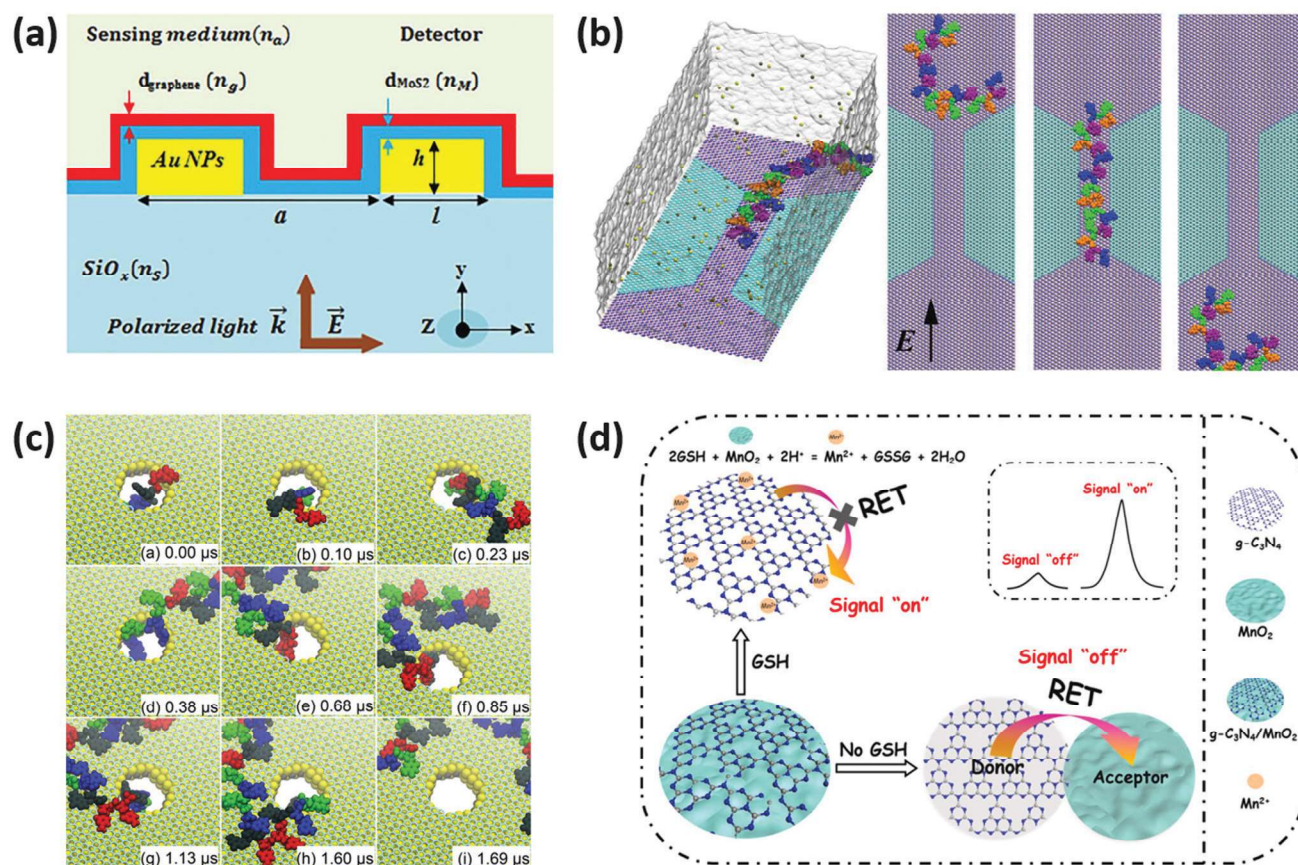


Fig. 21 2D HSs for biosensing. (a) Schematic representation of highly sensitive hybrid LSPR sensor based on AuNPs/MoS₂ (blue)/G (red). Reproduced with permission from ref. 316, copyrights reserved to Elsevier 2020. (b) System setups for MD simulations of ssDNA's transport through a 2D nanopore. The simulation system contains a patterned 2D HS containing the graphene domain (cyan), the *cis* and *trans* hBN reservoirs and hBN nanopores (N atoms in blue and B atoms in pink); 20-base-long ssDNA molecule adsorbed on the 2D surface; K⁺ and Cl⁻ ions are coloured in tan and yellow respectively; water is shown transparently (left). ssDNA molecule transits the 2D nanopore in a stretched and single-file conformation (right). Reproduced with permission from ref. 317, copyrights reserved to American Chemical Society 2020. (c) Snapshots of the progressive transport of the ssDNA molecule through the G/MoS₂ HS pore: (a) 0, (b) 0.10, (c) 0.23, (d) 0.38, (e) 0.68, (f) 0.85, (g) 1.13, (h) 1.60, and (i) 1.69 μ s. Reproduced with permission from ref. 318, copyrights reserved to American Chemical Society 2018. (d) Schematic principle of the designed "off-on" ECL-RET sensing platform for GSH detection. Reproduced with permission from ref. 319, copyrights reserved to Elsevier 2019.

using micro and nanofluidic channels has been reported exclusively.^{320–322} However, stretching ss-DNA with fluidic channels has not been a straightforward approach for reasons such as electro-osmosis and clogging.^{323,324} Building 2D HSs with nanopores could support simplistic transportation and sensing of ss-DNA by limiting one nucleotide at a time through the 2D nanopores.³²⁵ As an example, the lateral G/h-BN HS³¹⁷ has demonstrated elongation of a 20 base-long ss-DNA that is energetically confined between two graphene barriers. The transportation of the nucleotides of ss-DNA occurred in just 22 ns from the *cis* h-BN reservoir to the *trans* h-BN reservoir with the application of an external bias (Fig. 21b). As both graphene and h-BN possess different adsorption energies for ss-DNA on their surface, this flat planar HS facilitated spontaneous stretching of ss-DNA with improved signal to noise ratio and minimal spatial fluctuation. In another attempt, Luan *et al.* also theoretically illustrated ss-DNA transportation using a nanopore made of G/MoS₂ without the application of an external bias.³¹⁸ The illustration showed continuous transportation of nucleotides through the pores of G/MoS₂ just by harnessing the

chemical potential difference for ss-DNA on the surface of both the materials. The challenges of false data readouts and cross-talking between the nucleotides of ss-DNA^{326–328} are seen to be alleviated through this technique. The illustrated results have shown that the nucleotides can move from the surface of MoS₂ to graphene in 1.7 μ s (Fig. 21c). Nonetheless, these prototypes hold promising capabilities for base sensing of DNA molecules that can be exploited for practical applications.

In a very different approach, electrochemiluminescence (ECL) and resonant energy transfer (RET) techniques were implemented for the detection and measurement of a complex biomolecule like glutathione.^{319,329,330} The limitation of obtaining high energy transfer efficiencies *via* this strategy has been overcome by devising a 2D HS made of a donor (g-C₃N₄) and an acceptor (MnO₂). This facilitated the shortening of the energy transfer distance between the molecules, thereby providing an improved charge transfer reaction and an obvious increase in resonant efficiency. In this HS, absence of glutathione is seen through a weaker ECL signal while the presence of glutathione

shows a stronger ECL signal due to the decomposition of MnO_2 to Mn^{2+} on $g\text{-C}_3\text{N}_4$ (Fig. 21d).^{319,329,330} Successively, this mode of operation facilitated high sensitivity with detection limits as low as 0.05 μM in human serum.

It is clearly implicated through the above examples that certain complications such as poor sensitivity, low efficiency and ambient degradation suffered by pristine 2D materials have been resolved through the formation of HSs. However, further in-depth systematic investigation is needed to understand the behaviour of interfacial properties in the presence of bioanalytes. The current research trajectory is focused more on DNA sensing; therefore, a better understanding of the interfacial mechanism will aid in expanding the sensing paradigms to many other complex bioanalytes such as proteins, peptides, and various kinds of viruses and bacteria. This will eventually lead to faster development of biosensors in this exciting field of study.

6.3.3 Optoelectronic sensors. 2D HSs can be harnessed in developing a range of optoelectronic devices such as photodetectors, photovoltaic cells, photodiodes and light-emitting diodes,²⁴ where heterointerfaces play a pivotal role in altering the optical properties of dissimilar materials.³³¹ For instance, a vdW HS results in the advent of a new set of Dirac points as can be seen in the case of the G/h-BN vdW 2D HS.³³² Interlayer coupling is another phenomenon that promotes alteration of the band structure of associated hetero materials.³⁰⁴ Strong and weak coupling facilitate different band alignments and optical transactions between the alien materials.⁹⁵ The conduction band minimum and the valence band maximum contained in opposite layers facilitate effective spatial separation of electron-hole pairs in a 2D HS.^{202,333} This phenomenon proves extremely beneficial for solar energy conversion and light detection. Interlayer excitonic emission,³³⁴ improved tunnelling efficiency, photo gating, rectification, and bandgap modulation due to variations in stacking angles³³⁵ are some of the intriguing phenomena that occur in a 2D HS. Table 3 discusses different 2D HSs and their device performances to highlight the role of different heterointerfaces.

Broadband photodetection (BPD), one of the essential aspects of a photodetector (PD), provides the possibility for a single device to detect a range of wavelengths. Bulk and pristine 2D materials show low optical absorption coefficients and low mobility,⁴⁴ thereby hampering their ability to be selective to a broad wavelength range. The formation of 2D HSs eliminates such problems by providing two or more photoactive layers which provide different absorption coefficients and effective separation of electron-hole pairs ultimately broadening their absorption spectra. Alei *et al.* showed BPD from UV to NIR by devising a $p\text{-MoTe}_2/g\text{-n-SnS}_2$ HS encapsulated on both sides by h-BN.³³⁶ The availability of 3 photoactive layers provides surplus photocarriers which aid in providing a responsivity (R) value that exceeds 2600 A W^{-1} for both 532 and 1064 nm wavelengths. Graphene considerably reduces the interfacial trap charges and improves the interfacial contact for effective charge transfer *via* the heterointerface. Interestingly, at wavelengths above 1240 nm, the effect of photogating³³⁷ becomes predominant in the HS due

Table 3 Comparative optoelectronic performances of different 2D HSs to highlight the role of heterointerfaces

Sensing HS	Synthesis method	Type of PDs	Wavelength (nm)	Responsivity (A W^{-1})	Detectivity (Jones)	EQE (%)	Ref.
$\text{SnSe}_2/\text{MoS}_2$	Two-step CVD	V-PC	500	9.1×10^3	9.1×10^{10}	3.1×10^4	344
$\text{h-BN}/\text{MoTe}_2/\text{G}/\text{SnS}_2/\text{h-BN}$	Layer-by-layer dry transfer	V-PV	1064	2.63×10^3	1.09×10^{13}	—	336
$\text{MoS}_2/\text{h-BN}/\text{G}$	Dry transfer	V-PC	405	180	2.63×10^{13}	—	345
$\text{G}/\text{WSe}_2/\text{G}$	Dry transfer	V-PTI	1500	0.00012	—	—	343
GaSe/GaSb	Layer-by-layer epitaxial growth	V-PV	680	0.1	2.2×10^{12}	50	337
$\text{WSe}_2/\text{BP}/\text{MoS}_2$	Mechanical exfoliation + dry transfer	V-PC-FET	1550	1.12	2.21×10^{10}	—	346
$\text{MoS}_2/\text{G}/\text{WSe}_2$	Polymer-free vdW assembly + dry transfer	V-PV-FET	532	4250	2.2×10^{12}	10^6	347
PbS/MoS_2	Dry transfer	V-PC	800	4.5×10^4	3×10^{13}	—	348
WS_2/WSe_2	CVD	L-PV diode-FET	514	—	—	9.9	342
BP/MoS_2	CVD + mechanical exfoliation	V-PV diode-FET	633	0.418	—	0.3	349
$\text{G}/\text{MoS}_2/\text{WSe}_2/\text{G}$	Polymer-free vdW assembly	V-PV-FET	532	0.002	—	34	350
$\text{WSe}_2/\text{MoS}_2$	Exfoliation + transfer	V-diode-FET	750	0.011	—	1.5	351
$\text{G}/\text{MoS}_2/\text{G}$	CVD + exfoliation	V-PV-FET	488	0.22	—	55	352
Special PDs							
Sensing HS	Synthesis method	Device performance					Ref.
MoS_2/WS_2	Polymer-free transfer	Ultrafast hole transfer time (<50 fs)					44
$\text{G}/\text{h-BN}/\text{G}$	CVD + exfoliation + dry transfer	Seebeck coefficient – 99.3 $\mu\text{V K}^{-1}$; ZT = 1.05×10^{-6}					353

PC – photoconductor, PV – photovoltaic, L – lateral, V – vertical.

to the enhanced exciton lifetime of trapped charges at the heterointerface. A strong interlayer coupling transition was observed in the type-II $\text{MoTe}_2/\text{MoS}_2$ BPD where the phenomenon facilitated a distinct photoresponse in the infrared region of 1550 nm wavelength.⁹⁹ Functionalised PDs have also been attempted where a 2D HS made of ultrathin Ga_2O_3 and TiO_2 was functionalised with Ag plasmonic nanostructures that showed improved responsivity in the visible range. The 2D HS supported an enhanced charge separation process at the heterointerface accompanied by a reduction in dark current.³³⁸

Whilst most 2D HSs limited their light detection abilities to wavelengths ranging between UV and NIR, Zong *et al.* devised a BP/WSe₂ and BP/MoS₂ PD that detected mid-infrared (MIR) wavelengths at room temperature.³³⁹ A 4 nm thick BP placed on WSe₂ displayed significant PL quenching with an enhancement

as high as 192% in the MIR region ranging from 2.79 μm to 3.89 μm (Fig. 22a). Owing to the band bending of BP near the heterointerface of BP/WSe₂, charge carriers were effectively transferred from BP to WSe₂ that ensured efficient separation of electron–hole pairs. Similarly, with the BP/MoS₂ HS, an EL enhancement is obtained at 4.09 μm at room temperature (Fig. 22b). The above processes were supported by band to band and thermionic tunnelling that facilitated rapid charge transfer at the heterointerface upon application of various drain and gate voltages.

Because of the synergistic effect in 2D HSs, the effect of photovoltaics becomes more pronounced compared to pristine 2D materials. An asymmetric 2D HS made of graphene, h-BN, MoS₂ and MoTe₂ showed charge injection to the active layers through tunnelling (under the application of a negative drain

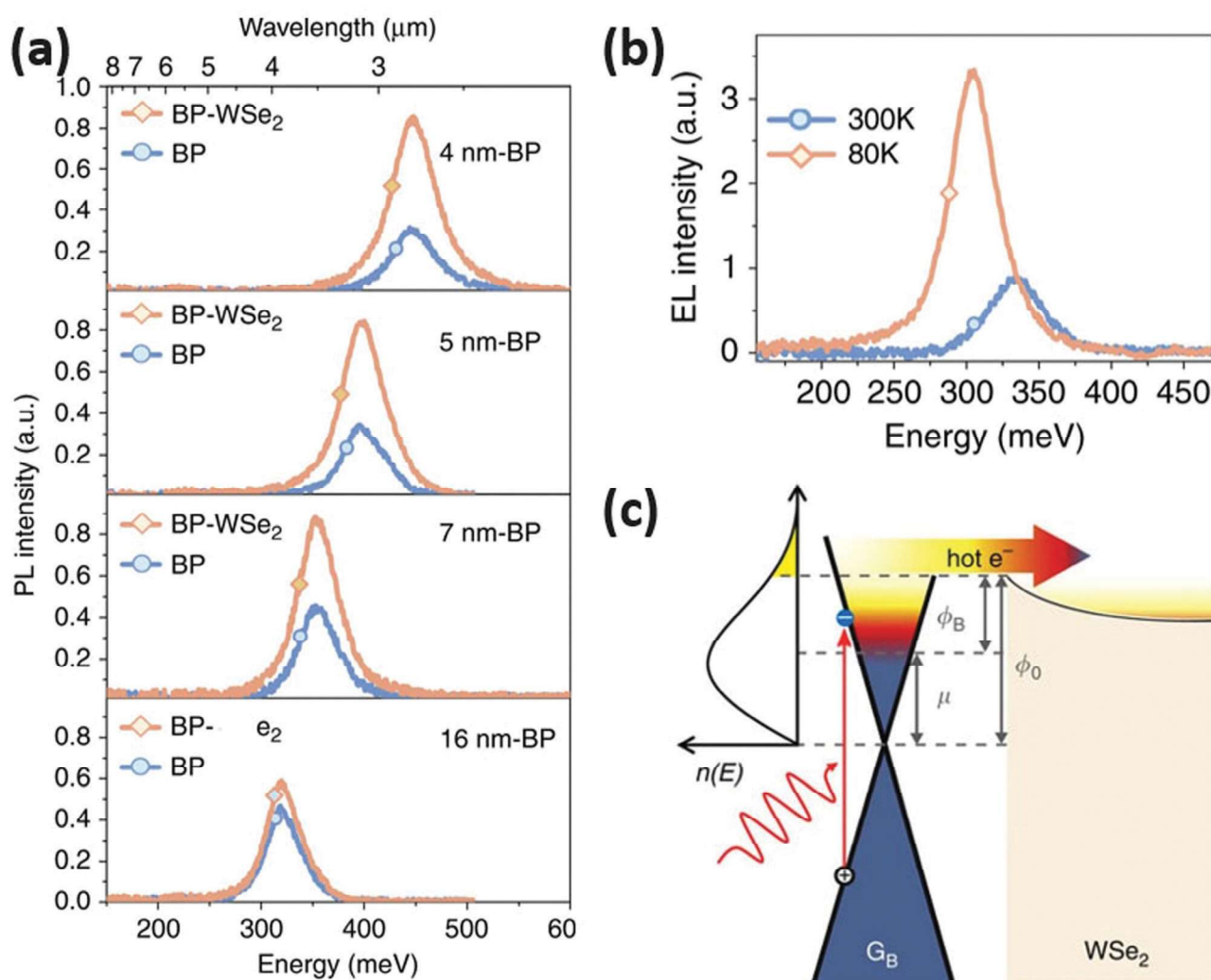


Fig. 22 2D HSs for optoelectronics. (a) MIR PL spectra of thin-film BP (blue lines) and BP-WSe₂ HSs (orange lines) at 80 K. (b) EL of the BP-MoS₂ heterojunction diode at 80 K, $I_{\text{ds}} = 8.05 \mu\text{A}$ (orange line) and at 300 K, $I_{\text{ds}} = 8.50 \mu\text{A}$ (blue line). Reproduced with permission from ref. 339, copyrights reserved to Springer Nature 2020. (c) Simplified band diagram of the PTI effect at a G/WSe₂ interface. The ultrafast thermalisation of photoexcited carriers in graphene gives rise to a hot-electron distribution $n(E)$ with a lifetime longer than 1 ps. As the number of electrons in the hot tail (yellow shaded area) of $n(E)$ increases, more electrons are emitted over the Schottky barrier ϕ_{B} , which generates a larger thermionic current (represented by the horizontal arrow). The colour gradient from blue to yellow illustrates the heat contained in the electron distribution. The offset between the graphene neutrality point and the WSe₂ conduction edge is denoted by ϕ_0 and was experimentally determined to be 0.54 eV. Reproduced with permission from ref. 343, copyrights reserved to Springer Nature 2016.

bias) and thermal activation mechanisms (under the influence of a positive drain bias).³⁴⁰ A strain free heterointerface allowed effective control over the gate, which modulated the carrier density of MoS₂ and MoTe₂. This enabled a rectification ratio as high as 10⁸ and an on-off ratio of 6×10^8 . A record low current of $\sim 10^{-5}$ nA proved the HS's ability to be used for the development of low-power devices.³⁴⁰

Charge transfer and response time remain as critical parameters to evaluate the performance of a PD. For instance, the sharp heterointerface of MoS₂/WS₂ showed that ultrafast charge transfer of holes *via* the heterointerface occurred within 50 fs of optical excitation.⁴⁴ This was verified from the process of PL quenching and observations of strong transient optical signals. Furthermore, a G/WSe₂/G HS encapsulated by h-BN exhibited sub-picosecond (5.5 ps) optical excitation.³⁴¹ Factors such as the thickness of the layers, bias voltage (V_B), channel length, and out-of-plane drift-diffusion that occurs *via* the heterointerface facilitated such a fast response.

Besides the vertical WS₂/MoS₂, a lateral WS₂/MoS₂ also showed strong photovoltaic properties.³⁰ The built-in electric field at the sharp atomic heterointerfaces showed strong PL intensities due to exciton generation at intermediate energies. The heterointerface also acted as a recombination site that facilitated an effective separation of electron-hole pairs. Similarly, a WS₂/WSe₂ lateral HS FET revealed rectification properties at the heterointerface, with the formation of a p-n diode.³⁴² Localised photoresponse obtained at the heterointerface enabled an external quantum efficiency of 9.9%, thereby proving the capability of the formed lateral HS.

By inducing a temperature gradient to the top and bottom graphene layers, a G/WSe₂/G HS could detect low energy photons through the mechanism of photo-thermionic (PTI) emission.³⁴³ The quick movement of electron-hole pairs to the thermalised carrier distribution centre enabled carriers with energy higher than the Schottky barrier height to be moved to WSe₂ *via* the G/WSe₂ heterointerface (Fig. 22c). A characteristic decay time of 1.3 ps was extracted on the cooling time of hot carriers in graphene that implicated domination of the PTI effect over photocurrent generation in the HS.

Various 2D HSs have been formulated to date which show promising optoelectronic properties. Bandgap and heterointerface engineering have been well-examined in many HSs that offer novel physical properties at the atomic scale. Heterointerfaces also provide feasible outcomes for PD's figures of merit. One aspect that has not been covered in 2D HS based PDs is the surface treatment of a 2D HS by means of doping. Focused research on this topic could bring out novel concepts and suggest if there is any room for performance improvements. Also, the temperature gradient is one aspect that is neglected in most HSs. A careful study of this aspect could facilitate more HSs in this area of study. Despite the improvements seen here, it is felt that a considerable amount of effort must be put into realising 2D HS based devices for commercial use.

6.4. Neuromorphic and plasmonic applications

2D HSs, having unique heterointerfaces, offer significant advantages for data integration, tuneability, and power consumption

which are imperative in memristive, synaptic, nociceptive, and plasmonic responses that could be used in the field of neuromorphic computing and data communications.³⁵⁴⁻³⁵⁶ High-quality heterointerfaces obtained by combining distinct 2D materials have shown promising potential as resistive switching memories. The heterointerfaces formed between the distinct 2D layers fundamentally affect the data storage mechanism by drastically enhancing the charge transport properties, ultimately leading to the possibility of developing robust memristors.³⁵⁷ Traditional memristors (mostly based on oxides) suffer from poor thermal stability at elevated temperatures, which limits their applications. However, the excellent structural stability that may be offered by 2D HSs can come to the rescue by creating exceptional switching abilities.³⁵⁸ As an example, G/MoS_{2-x}O_x/G has been constructed,³⁵⁹ which showed an operational temperature of up to 340 °C with repetitive bipolar switching and endurance up to 10⁷. The high thermal stability is attributed to the existence of an atomically sharp heterointerface between the graphene electrodes and the MoS_{2-x}O_x switching layer, a property not easily achievable in metal oxide films. Additionally, the 2D HS fabricated on polyimide offers both exceptional mechanical flexibility and thermal stability over 1000 bending cycles, which again is quite arduous to achieve in standalone organic and inorganic materials.³⁵⁹ Besides, 2D HSs also offer device architectures that could work under novel operational modes which can reduce power consumption and high-data integrability.³⁶⁰ The memtransistor architecture, in particular, can take advantage of 2D HSs that provide the possibility of assimilating one-transistor-one-resistor (1T1R) configuration within a single device that offers the unique advantage of self-selectivity.³⁶¹ The problems such as sneak path current and absence of multiple states that predominantly exist in 2D pristine counterparts can be resolved through the formation of 2D HSs.³⁶² Highly functional memory devices have thus been devised with the help of 2D HS based memristors that hold great prospects for futuristic neuromorphic technologies.

Apart from memristors, neuromorphic applications have also been involved in realising bio-inspired electronic devices. Artificial synapse is one such example that mimics certain neural functionalities of the biological synapse such as the learning/forgetting behaviours and short- and long-term memories, to name a few.³⁶³ 2D HSs have been reported to provide superior synaptic performances in comparison to standalone 2D synaptic devices for a variety of reasons.^{355,364} Firstly, architectures like those based on memtransistors, which facilitate the incorporation of gate tuneability, can display enhanced tuneability of potentiation using 2D HSs, as observed in the vertical G/WSe₂/WO_x.^{230,355} Secondly, transistor-based 2D HSs have shown additional control to explore other neural functionalities such as spike time-dependent plasticity (STDP) and Hebbian and non-Hebbian learning which improve data accuracy and ultimately lead to a more realistic imitation of biological synapses.^{192,365} Finally, defect engineering at heterointerfaces plays a vital role in adjusting the charge trapping/de-trapping process thereby allowing precise modulation of the trap states which helps in achieving desirable synaptic characteristics.³⁶⁶

In addition to electronic synaptic devices, a wide variety of optoelectronic synapses have also been formulated using 2D HSs. It should also be added that the ability to modulate band alignment at the heterointerface with the help of photonic signals stands as a key factor in designing a wide variety of artificial synapses.^{362,367} Additionally, whilst many pristine 2D based artificial synapses are only limited to UV detection due to their wide bandgap property, 2D HS based photonic synapses can facilitate a wider detection of wavelengths by choosing semimetal or lower bandgap semiconductors.³⁶⁸ Due to these advantages, characteristics such as bio-plasticity, long-term potentiation (LTP), long-term depression (LTD) effects, and STDP have been successfully mimicked by highly energy-efficient 2D HSs.^{369,370}

In recent attempts, 2D HSs have been deployed in devising artificial nociceptors, another category of bio-inspired electronics that can mimic the functions of corneal nociceptors of the human eye. For instance, Akbari *et al.* developed an ultrathin highly transparent 2D HS that enabled a highly sensitive TiO₂/Ga₂O₃ (Ar) and a high threshold TiO₂/Ga₂O₃ (N₂) artificial nociceptor.¹³³ Similarly, 2D HSs, made of WO₃/TiO₂ and Ga₂O₃ [or Ga₂O₃(N₂)]/TiO₂, have enabled the receptive and nociceptive detection of visible light pulses where behaviours such as threshold, relaxation, allodynia, and hyperalgesia have been successfully demonstrated.³⁷¹ The difference in electro-negativity, obtained by combining distinct 2D materials, along with the ability to achieve effective modulation at the heterointerface has facilitated the development of optoresponsive nociceptors that bear a close resemblance to the human bio-nociceptors.^{133,371} Altogether, the bio-capability of 2D HSs is evident from these proof-of-concept reports and they hold great potential in devising a wide variety of smart optical devices in the future.

In addition to advancements seen in electronic and optoelectronic devices, plasmonic devices are increasingly seen amongst 2D HSs where feasible solutions are provided to overcome the challenges of high-power consumption and heat generation in electronic circuitry.³⁷² Graphene, a widely recognised plasmonic material, within the IR region, has been deemed to be relatively slow for all-optical plasmonic modulation.³⁷³ However, graphene when combined with TMDs facilitates ultrafast optical modulation due to the enhanced charge transfer and recombination of photogenerated carriers.³⁷⁴ For example, the G/MoS₂ 2D HS demonstrated the transfer of photoexcited charge carriers within 7 ps from MoS₂ to graphene *via* the heterointerface.³⁷⁵ Plasmonic modulators based on 2D HSs proved to be highly beneficial for future data processing and communications; therefore, further investigation is required to construct 2D HSs with the selected materials successfully.

It is realised that high-density data integration, improved area efficiency, and low power consumption are some of the key benefits that come along with 2D HSs for neuromorphic and data processing applications. However, chip-level advancements in memristor structures have not been implemented to date, which requires enormous synthesis, fabrication, and integration efforts and advancements. Whilst a considerable amount of progress has been made with artificial synapses, artificial nociceptors based

on 2D HSs are still in their infancy, which means they require significant attention.

7. Conclusions and future perspectives

The emergence of new properties by creating heterointerfaces among dissimilar materials has attracted intensive research into understanding the role of the heterointerface in giving birth to new properties in HSs. Here, we have reviewed the recent literature on 2D HSs to explain the nature and role of heterointerfaces in overcoming the shortcomings of individual 2D materials, to optimise the synthesis methods for better control over the heterointerface and to obtain 2D HSs at large-scale. The physicochemical properties of 2D HSs are highly dependent on the structure and the type of heterointerfaces. Generally, two types of interfaces can be formed among the 2D materials, either connected through strong static interactions forming vdW 2D HSs or connected through a direct covalent bond forming covalently bonded 2D HSs. In fact, the dangling free planar surfaces of 2D materials provide considerable flexibility for constructing the heterointerfaces of desired materials without considering their incompatibility or lattice mismatch constraints. The creation of such atomically sharp heterointerfaces, with highly distinct electronic, optical and catalytic properties, offers new functionalities emerging from the generation, confinement and transport of charges, photons, phonons and excitons. Thus, it allows the designing of new electronic and optoelectronic devices for multiple sensing applications. Moreover, modulated electronic properties of vdW 2D HSs through rapid charge transfers and their redistributions at the heterointerface allow optimised adsorption energies for several intermediates along with high conductivity resulting in enhanced electrochemical performances for energy storage and conversion applications. However, these electronic changes in vdW 2D HSs are mostly originated by tuning the density of states through physical interactions which required certain structural matching. However, these structural matching start to diminish when used as electrodes in electrochemical devices where electrolytes/ions need to penetrate through the layers. Besides, when structural changes are made to allow 3D movement of electrolytes for efficient mass transport, by introducing porous structures, many vdW 2D HSs fail to provide full benefits of the HS. Thus, covalent connections were found beneficial to address such challenges which are difficult or impossible to address through vdW HSs. The covalent connections allow direct electron transfer through their unique heterointerfaces and also provide easy structural tunings to make 2D HSs suitable for applications where vdW 2D HSs fail to give their best advantages like in batteries. Moreover, covalent 2D HSs offer natural structural matching of 2D materials, hence allowing the integration of a variety of 2D materials especially with defects or high porosity to enhance the density of the active sites and fast 3D mass transport. In addition, covalently bonded 2D HSs also provide flexibility in terms of tuning the chemistry of heterointerfaces through introducing heteroatoms bringing

additional redox-active centres as well as providing opportunities to manage the spacing at the heterointerfaces by introducing long linkers to make 2D HSs effective for storage of ions with large ionic radii such as Na^+ , K^+ , Zn^{2+} , and Al^{3+} . Besides all these advantages, sandwiching of individual 2D materials into 2D HSs creates high structural stability for long life when implemented into various devices.

No doubt, 2D HSs provide enhanced properties and new functionalities but these can only be achieved through a facile synthesis of such 2D HSs with fine control over heterointerfaces and controllable sequential stacking of 2D materials at large-scale. The challenge with currently available synthesis methods is their small-scale for constructing 2D HSs (like CVD, PVD, and ALD) as well as the fact that they are mostly restricted to the formation of vdW heterointerfaces on specific substrates. Although the quality of heterointerfaces formed by these methods is generally high, limited production forces researchers to develop alternative approaches where solution-based approaches like ECD, hydro-/solvo-thermal synthesis, LBL, electrostatic self-assembly, and interfacial growth are found effective. Some of these can produce very large quantities, such as hydro-/solvo-thermal synthesis, but generally offer very poor control over the quality of heterointerfaces and structures of the resultant 2D HSs; thus, they are not capable of fetching the full capabilities of 2D HSs. However, techniques like LBL, electrostatic self-assembly and interfacial growth are found to be promising in developing both high-quality and large quantities of 2D HSs. But these techniques require very sophisticated synthesis of individual 2D materials and their functionalisation with required charges or groups to define and control the quality of heterointerfaces. Therefore, in-depth knowledge of chemistry and materials science is required to explore different methods with appropriate modifications to develop scalable synthesis methods to produce large quantities of 2D HSs with well-defined heterointerfaces.

Besides the synthesis of 2D HSs, their characterisation, to determine the nature of the heterointerface and its role in manipulating the characteristics of 2D materials, is very challenging, especially in the case of vertically stacked 2D HSs. The combination of various techniques has been utilised where comparing the characteristics of 2D HSs with individual 2D materials provides information about the heterointerface. But to properly understand the advantages of 2D HSs and their formation, such characterisation techniques need to be explored that can provide the exact information solely like in the case of individual materials, where *in situ* approaches or support from theoretical studies can be essential to set the data bank for comparative analysis among 2D HSs. In addition to characterisation, integrating complex 2D HSs into functional devices is another challenge as it requires reliable and independent contact to each layer for electronic devices. Similarly, batteries and water splitting require 3D ionic diffusion, which is restricted by the planar structure of 2D materials, and can be obtained by utilising holey 2D materials but then constructing their 2D HSs will be another challenge due to the presence of possible dangling bonds at the basal planes or poor crystallinity that results in high mismatch.

To make 2D HSs available and go beyond the boundaries of current technologies, efforts from both theoretical and experimental researchers are required working in close collaboration. The theoretical studies can help to predict the best combinations of 2D materials (based on the bandgap, charge transport/separation/generation, impact on the density of state, manipulation of redox-active sites as well as many other parameters) along with the suitable heterointerface (vdW or covalent) to achieve the functionalities missing in the individual 2D materials. This will help in saving time spent by experimentalists in the hit and trial method of various combinations to achieve the desired 2D HSs efficiently by being well-informed and will help them to modify their experimental procedures much faster. The theoretical studies can also help to understand the role of heterointerfaces in improving the properties of 2D materials and their behaviour in specific applications, such as how the ionic and electronic separations can occur at the heterointerface in the presence of electrolytes between the layers of dissimilar materials, where the traditional DFT studies are not sufficient. In the end, better methods to produce high-quality 2D HSs with precise control over physical dimensions (lateral and vertical thickness), chemical composition, relative orientations and well-defined heterointerfaces in a stacked manner are required; otherwise, all the benefits of 2D HSs listed in this review or literature will remain restricted to books.

Conflicts of interest

There are no conflicts to declare.

Acknowledgements

N. M. is grateful for the financial support from RMIT Vice-Chancellor Fellowship, RMIT University, Australia. S. G. is grateful for the RTP Stipend Scholarships (RSS), funded by the Commonwealth Government of Australia. R. V. appreciates the support from McKenzie Fellowship, University of Melbourne, Australia. K. K. Z. acknowledges support from the Australian Research Council Centre of Excellence FLEET (CE170100039). M. W. K. would like to recognise the HEC, Pakistan-RMIT University, Australia joint program for the PhD scholarship and acknowledges the support provided by CSIRO, Australia.

Notes and references

- 1 K. S. Novoselov, A. Mishchenko, A. Carvalho and A. H. Castro Neto, *Science*, 2016, **353**, aac9439.
- 2 D. Jariwala, T. J. Marks and M. C. Hersam, *Nat. Mater.*, 2017, **16**, 170–181.
- 3 P. Solis-Fernandez, M. Bissett and H. Ago, *Chem. Soc. Rev.*, 2017, **46**, 4572–4613.
- 4 H. Wang, F. Liu, W. Fu, Z. Fang, W. Zhou and Z. Liu, *Nanoscale*, 2014, **6**, 12250–12272.
- 5 A. Pant, Z. Mutlu, D. Wickramaratne, H. Cai, R. K. Lake, C. Ozkan and S. Tongay, *Nanoscale*, 2016, **8**, 3870–3887.

- 6 X. Liu and M. C. Hersam, *Adv. Mater.*, 2018, **30**, 1801586.
- 7 M.-H. Chiu, C. Zhang, H.-W. Shiu, C.-P. Chuu, C.-H. Chen, C.-Y. S. Chang, C.-H. Chen, M.-Y. Chou, C.-K. Shih and L.-J. Li, *Nat. Commun.*, 2015, **6**, 7666.
- 8 C. Jin, E. Y. Ma, O. Karni, E. C. Regan, F. Wang and T. F. Heinz, *Nat. Nanotechnol.*, 2018, **13**, 994–1003.
- 9 L. Li and M. Zhao, *J. Phys. Chem. C*, 2014, **118**, 19129–19138.
- 10 C. R. Dean, A. F. Young, I. Meric, C. Lee, L. Wang, S. Sorgenfrei, K. Watanabe, T. Taniguchi, P. Kim, K. L. Shepard and J. Hone, *Nat. Nanotechnol.*, 2010, **5**, 722–726.
- 11 J. Fu, J. Yu, C. Jiang and B. Cheng, *Adv. Energy Mater.*, 2018, **8**, 1701503.
- 12 Z. Yuan, J. Li, M. Yang, Z. Fang, J. Jian, D. Yu, X. Chen and L. Dai, *J. Am. Chem. Soc.*, 2019, **141**, 4972–4979.
- 13 Q. Sun, J. Hao, S. Zheng, P. Wan, J. Li, D. Zhang, Y. Li, T. Wang and Y. Wang, *Nanotechnology*, 2020, **31**, 425502.
- 14 F. Yu, H. Zhou, Y. Huang, J. Sun, F. Qin, J. Bao, W. A. Goddard, S. Chen and Z. Ren, *Nat. Commun.*, 2018, **9**, 2551.
- 15 G.-C. Guo, R.-Z. Wang, B.-M. Ming, C. Wang, S.-W. Luo, M. Zhang and H. Yan, *J. Mater. Chem. A*, 2019, **7**, 2106–2113.
- 16 X. Wang, Y. Li, P. Das, S. Zheng, F. Zhou and Z.-S. Wu, *Energy Storage Mater.*, 2020, **31**, 156–163.
- 17 E. Pomerantseva and Y. Gogotsi, *Nat. Energy*, 2017, **2**, 17089.
- 18 A. Zhu, L. Qiao, Z. Jia, P. Tan, Y. Liu, Y. Ma and J. Pan, *Dalton Trans.*, 2017, **46**, 17032–17040.
- 19 D. Jariwala, V. K. Sangwan, C.-C. Wu, P. L. Prabhurashi, M. L. Geier, T. J. Marks, L. J. Lauhon and M. C. Hersam, *Proc. Natl. Acad. Sci. U. S. A.*, 2013, **110**, 18076–18080.
- 20 D. Ruzmetov, K. Zhang, G. Stan, B. Kalanyan, G. R. Bhimanapati, S. M. Eichfeld, R. A. Burke, P. B. Shah, T. P. O'Regan, F. J. Crowne, A. G. Birdwell, J. A. Robinson, A. V. Davydov and T. G. Ivanov, *ACS Nano*, 2016, **10**, 3580–3588.
- 21 Y. Liu, N. O. Weiss, X. Duan, H.-C. Cheng, Y. Huang and X. Duan, *Nat. Rev. Mater.*, 2016, **1**, 16042.
- 22 K. K. Kim, H. S. Lee and Y. H. Lee, *Chem. Soc. Rev.*, 2018, **47**, 6342–6369.
- 23 Q. Zeng and Z. Liu, *Adv. Electron. Mater.*, 2018, **4**, 1700335.
- 24 X. Zhou, X. Hu, J. Yu, S. Liu, Z. Shu, Q. Zhang, H. Li, Y. Ma, H. Xu and T. Zhai, *Adv. Funct. Mater.*, 2018, **28**, 1706587.
- 25 T. A. Shifa, F. Wang, Y. Liu and J. He, *Adv. Mater.*, 2019, **31**, 1804828.
- 26 T. D. Thanh, N. D. Chuong, H. V. Hien, T. Kshetri, L. H. Tuan, N. H. Kim and J. H. Lee, *Prog. Mater. Sci.*, 2018, **96**, 51–85.
- 27 P. Das, Q. Fu, X. Bao and Z.-S. Wu, *J. Mater. Chem. A*, 2018, **6**, 21747–21784.
- 28 N. Mahmood, I. A. De Castro, K. Pramoda, K. Khoshmanesh, S. K. Bhargava and K. Kalantar-Zadeh, *Energy Storage Mater.*, 2019, **16**, 455–480.
- 29 C. Li, Q. Cao, F. Wang, Y. Xiao, Y. Li, J.-J. Delaunay and H. Zhu, *Chem. Soc. Rev.*, 2018, **47**, 4981–5037.
- 30 Y. Gong, J. Lin, X. Wang, G. Shi, S. Lei, Z. Lin, X. Zou, G. Ye, R. Vajtai, B. I. Yakobson, H. Terrones, M. Terrones, B. K. Tay, J. Lou, S. T. Pantelides, Z. Liu, W. Zhou and P. M. Ajayan, *Nat. Mater.*, 2014, **13**, 1135–1142.
- 31 C. N. R. Rao, K. Pramoda, A. Saraswat, R. Singh, P. Vishnoi, N. Sagar and A. Hezam, *APL Mater.*, 2020, **8**, 020902.
- 32 C. Huang, S. Wu, A. M. Sanchez, J. J. P. Peters, R. Beanland, J. S. Ross, P. Rivera, W. Yao, D. H. Cobden and X. Xu, *Nat. Mater.*, 2014, **13**, 1096–1101.
- 33 C. Wang, X. Shao, J. Pan, J. Hu and X. Xu, *Appl. Catal., B*, 2020, **268**, 118435.
- 34 Z. Huang, A. Alharbi, W. Mayer, E. Cuniberto, T. Taniguchi, K. Watanabe, J. Shabani and D. Shahrjerdi, *Nat. Commun.*, 2020, **11**, 3029.
- 35 P. Vishnoi, K. Pramoda, U. Gupta, M. Chhetri, R. G. Balakrishna and C. N. R. Rao, *ACS Appl. Mater. Interfaces*, 2019, **11**, 27780–27787.
- 36 K. Pramoda, U. Gupta, I. Ahmad, R. Kumar and C. N. R. Rao, *J. Mater. Chem. A*, 2016, **4**, 8989–8994.
- 37 X. Wang, H. Li, H. Li, S. Lin, W. Ding, X. Zhu, Z. Sheng, H. Wang, X. Zhu and Y. Sun, *Adv. Funct. Mater.*, 2020, **30**, 0190302.
- 38 C. Chen, X. Xie, B. Anasori, A. Sarycheva, T. Makaryan, M. Zhao, P. Urbankowski, L. Miao, J. Jiang and Y. Gogotsi, *Angew. Chem., Int. Ed.*, 2018, **57**, 1846–1850.
- 39 Y. Yu, J. Zhou and Z. Sun, *Nanoscale*, 2019, **11**, 23092–23104.
- 40 W. Hong, G. W. Shim, S. Y. Yang, D. Y. Jung and S.-Y. Choi, *Adv. Funct. Mater.*, 2019, **29**, 1807550.
- 41 M. P. Levendorf, C.-J. Kim, L. Brown, P. Y. Huang, R. W. Havener, D. A. Muller and J. Park, *Nature*, 2012, **488**, 627–632.
- 42 G. Fiori, A. Betti, S. Bruzzone and G. Iannaccone, *ACS Nano*, 2012, **6**, 2642–2648.
- 43 S. J. Haigh, A. Gholinia, R. Jalil, S. Romani, L. Britnell, D. C. Elias, K. S. Novoselov, L. A. Ponomarenko, A. K. Geim and R. Gorbachev, *Nat. Mater.*, 2012, **11**, 764–767.
- 44 X. Hong, J. Kim, S. F. Shi, Y. Zhang, C. Jin, Y. Sun, S. Tongay, J. Wu, Y. Zhang and F. Wang, *Nat. Nanotechnol.*, 2014, **9**, 682–686.
- 45 Z. Lin, A. Yin, J. Mao, Y. Xia, N. Kempf, Q. He, Y. Wang, C.-Y. Chen, Y. Zhang, V. Ozolins, Z. Ren, Y. Huang and X. Duan, *Sci. Adv.*, 2016, **2**, e1600993.
- 46 Z. Wei, M. K. Akbari, R. Hai, R. K. Ramachandran, C. Detavernier, F. Verpoort, E. Kats, H. Xu, J. Hu and S. Zhuiykov, *Sens. Actuators, B*, 2019, **287**, 147–156.
- 47 P. Xiong, X. Zhang, F. Zhang, D. Yi, J. Zhang, B. Sun, H. Tian, D. Shanmukaraj, T. Rojo, M. Armand, R. Ma, T. Sasaki and G. Wang, *ACS Nano*, 2018, **12**, 12337–12346.
- 48 K. Kang, K.-H. Lee, Y. Han, H. Gao, S. Xie, D. A. Muller and J. Park, *Nature*, 2017, **550**, 229–233.
- 49 R. Dong, T. Zhang and X. Feng, *Chem. Rev.*, 2018, **118**, 6189–6235.
- 50 Y. Zhu, W. Peng, Y. Li, G. Zhang, F. Zhang and X. Fan, *J. Mater. Chem. A*, 2019, **7**, 23577–23603.
- 51 P. Chen, Z. Zhang, X. Duan and X. Duan, *Chem. Soc. Rev.*, 2018, **47**, 3129–3151.
- 52 Z. Peng, R. Yang, M. A. Kim, L. Li and H. Liu, *RSC Adv.*, 2017, **7**, 27048–27057.
- 53 D. Voiry, R. Fullon, J. Yang, C. de Carvalho Castro e Silva, R. Kappera, I. Bozkurt, D. Kaplan, M. J. Lagos, P. E. Batson, G. Gupta, A. D. Mohite, L. Dong, D. Er, V. B. Shenoy, T. Asefa and M. Chhowalla, *Nat. Mater.*, 2016, **15**, 1003–1009.

- 54 M.-Q. Zhao, N. Trainor, C. E. Ren, M. Torelli, B. Anasori and Y. Gogotsi, *Adv. Mater. Technol.*, 2019, **4**, 1800639.
- 55 Q. H. Wang, K. Kalantar-Zadeh, A. Kis, J. N. Coleman and M. S. Strano, *Nat. Nanotechnol.*, 2012, **7**, 699–712.
- 56 M. Mohiuddin, Y. Wang, A. Zavabeti, N. Syed, R. S. Datta, H. Ahmed, T. Daeneke, S. P. Russo, A. R. Rezk, L. Y. Yeo and K. Kalantar-Zadeh, *Chem. Mater.*, 2018, **30**, 5593–5601.
- 57 M. Mohiuddin, N. Pillai, A. Zavabeti, N. Mahmood, N. Syed, R. S. Datta, D. Jampaiah, T. Daeneke, J. Z. Ou and K. Kalantar-Zadeh, *Appl. Mater. Today*, 2018, **12**, 359–365.
- 58 C. Tan and H. Zhang, *Chem. Soc. Rev.*, 2015, **44**, 2713–2731.
- 59 K. Kalantar-zadeh, J. Z. Ou, T. Daeneke, A. Mitchell, T. Sasaki and M. S. Fuhrer, *Appl. Mater. Today*, 2016, **5**, 73–89.
- 60 Y. Wang, B. J. Carey, W. Zhang, A. F. Chrimes, L. Chen, K. Kalantar-zadeh, J. Z. Ou and T. Daeneke, *J. Phys. Chem. C*, 2016, **120**, 2447–2455.
- 61 L. Lin, W. Lei, S. Zhang, Y. Liu, G. G. Wallace and J. Chen, *Energy Storage Mater.*, 2019, **19**, 408–423.
- 62 R. S. Datta, F. Haque, M. Mohiuddin, B. J. Carey, N. Syed, A. Zavabeti, B. Zhang, H. Khan, K. J. Berean, J. Z. Ou, N. Mahmood, T. Daeneke and K. Kalantar-zadeh, *J. Mater. Chem. A*, 2017, **5**, 24223–24231.
- 63 J. Mei, T. Liao, L. Kou and Z. Sun, *Adv. Mater.*, 2017, **29**, 1700176.
- 64 A. Ostadhosseini, J. Guo, F. Simeski and M. Ihme, *Commun. Chem.*, 2019, **2**, 95.
- 65 E. P. Nguyen, B. J. Carey, J. Z. Ou, J. van Embden, E. D. Gaspera, A. F. Chrimes, M. J. S. Spencer, S. Zhuiykov, K. Kalantar-zadeh and T. Daeneke, *Adv. Mater.*, 2015, **27**, 6225–6229.
- 66 C. Zhang, N. Mahmood, H. Yin, F. Liu and Y. Hou, *Adv. Mater.*, 2013, **25**, 4932–4937.
- 67 H. Gao, J. Suh, M. C. Cao, A. Y. Joe, F. Mujid, K.-H. Lee, S. Xie, P. Poddar, J.-U. Lee, K. Kang, P. Kim, D. A. Muller and J. Park, *Nano Lett.*, 2020, **20**, 4095–4101.
- 68 J. Jiang, C. Ling, T. Xu, W. Wang, X. Niu, A. Zafar, Z. Yan, X. Wang, Y. You, L. Sun, J. Lu, J. Wang and Z. Ni, *Adv. Mater.*, 2018, **30**, 1804332.
- 69 W. Xu, C. Sun, K. Zhao, X. Cheng, S. Rawal, Y. Xu and Y. Wang, *Energy Storage Mater.*, 2019, **16**, 527–534.
- 70 Z. Dai, L. Liu and Z. Zhang, *Adv. Mater.*, 2019, **31**, 1805417.
- 71 B. You, M. T. Tang, C. Tsai, F. Abild-Pedersen, X. Zheng and H. Li, *Adv. Mater.*, 2019, **31**, 1807001.
- 72 Q. Gong, L. Cheng, C. Liu, M. Zhang, Q. Feng, H. Ye, M. Zeng, L. Xie, Z. Liu and Y. Li, *ACS Catal.*, 2015, **5**, 2213–2219.
- 73 M. Qiao, J. Liu, Y. Wang, Y. Li and Z. Chen, *J. Am. Chem. Soc.*, 2018, **140**, 12256–12262.
- 74 Y. Liu, Y. Huang and X. Duan, *Nature*, 2019, **567**, 323–333.
- 75 K. Atsushi, S. Kazumasa and M. Takao, *Microelectron. Eng.*, 1984, **2**, 129–136.
- 76 A. Koma, *J. Cryst. Growth*, 1999, **201–202**, 236–241.
- 77 M. Yankowitz, Q. Ma, P. Jarillo-Herrero and B. J. LeRoy, *Nat. Rev. Phys.*, 2019, **1**, 112–125.
- 78 J. Kang, J. Li, S. S. Li, J. B. Xia and L. W. Wang, *Nano Lett.*, 2013, **13**, 5485–5490.
- 79 C. Zhang, C.-P. Chuu, X. Ren, M.-Y. Li, L.-J. Li, C. Jin, M.-Y. Chou and C.-K. Shih, *Sci. Adv.*, 2017, **3**, e1601459.
- 80 H. Zheng, X.-B. Li, N.-K. Chen, S.-Y. Xie, W. Q. Tian, Y. Chen, H. Xia, S. B. Zhang and H.-B. Sun, *Phys. Rev. B: Condens. Matter Mater. Phys.*, 2015, **92**, 115307.
- 81 X. Ma, D. Jiang, P. Xiao, Y. Jin, S. Meng and M. Chen, *Catal. Sci. Technol.*, 2017, **7**, 3481–3491.
- 82 H. Wang, L. Zhang, Z. Chen, J. Hu, S. Li, Z. Wang, J. Liu and X. Wang, *Chem. Soc. Rev.*, 2014, **43**, 5234–5244.
- 83 K. Xu, Y. Xu, H. Zhang, B. Peng, H. Shao, G. Ni, J. Li, M. Yao, H. Lu, H. Zhu and C. M. Soukoulis, *Phys. Chem. Chem. Phys.*, 2018, **20**, 30351–30364.
- 84 Y. Liu, S. Zhang, J. He, Z. M. Wang and Z. Liu, *Nano-Micro Lett.*, 2019, **11**, 13.
- 85 J. Su, G. D. Li, X. H. Li and J. S. Chen, *Adv. Sci.*, 2019, **6**, 1801702.
- 86 J. Low, J. Yu, M. Jaroniec, S. Wageh and A. A. Al-Ghamdi, *Adv. Mater.*, 2017, **29**, 1601694.
- 87 F. Withers, O. Del Pozo-Zamudio, A. Mishchenko, A. P. Rooney, A. Gholinia, K. Watanabe, T. Taniguchi, S. J. Haigh, A. K. Geim, A. I. Tartakovskii and K. S. Novoselov, *Nat. Mater.*, 2015, **14**, 301–306.
- 88 S. J. A. Moniz, S. A. Shevlin, D. J. Martin, Z.-X. Guo and J. Tang, *Energy Environ. Sci.*, 2015, **8**, 731–759.
- 89 K. Zhang, T. Zhang, G. Cheng, T. Li, S. Wang, W. Wei, X. Zhou, W. Yu, Y. Sun, P. Wang, D. Zhang, C. Zeng, X. Wang, W. Hu, H. J. Fan, G. Shen, X. Chen, X. Duan, K. Chang and N. Dai, *ACS Nano*, 2016, **10**, 3852–3858.
- 90 A. T. Hanbicki, H. J. Chuang, M. R. Rosenberger, C. S. Hellberg, S. V. Sivaram, K. M. McCreary, I. I. Mazin and B. T. Jonker, *ACS Nano*, 2018, **12**, 4719–4726.
- 91 X. H. Li and M. Antonietti, *Chem. Soc. Rev.*, 2013, **42**, 6593–6604.
- 92 T. Kwon, M. Jun, J. Joo and K. Lee, *J. Mater. Chem. A*, 2019, **7**, 5090–5110.
- 93 Z. Hu, Z. Wu, C. Han, J. He, Z. Ni and W. Chen, *Chem. Soc. Rev.*, 2018, **47**, 3100–3128.
- 94 K. Chu, Y. P. Liu, Y. B. Li, Y. L. Guo and Y. Tian, *ACS Appl. Mater. Interfaces*, 2020, **12**, 7081–7090.
- 95 H. Fang, C. Battaglia, C. Carraro, S. Nemsak, B. Ozdol, J. S. Kang, H. A. Bechtel, S. B. Desai, F. Kronast, A. A. Unal, G. Conti, C. Conlon, G. K. Palsson, M. C. Martin, A. M. Minor, C. S. Fadley, E. Yablonovitch, R. Maboudian and A. Javey, *Proc. Natl. Acad. Sci. U. S. A.*, 2014, **111**, 6198–6202.
- 96 R. Li, W. Sun, C. Zhan, P. R. C. Kent and D.-E. Jiang, *Phys. Rev. B*, 2019, **99**, 085429.
- 97 I. Demiroglu, F. M. Peeters, O. Gulseren, D. Cakir and C. Sevik, *J. Phys. Chem. Lett.*, 2019, **10**, 727–734.
- 98 C. He, J. H. Zhang, W. X. Zhang and T. T. Li, *J. Phys. Chem. C*, 2019, **123**, 5157–5163.
- 99 W. Yu, Z. Zhu, S. Zhang, X. Cai, X. Wang, C.-Y. Niu and W.-B. Zhang, *Appl. Phys. Lett.*, 2016, **109**, 103104.
- 100 K. Chang and W. Chen, *ACS Nano*, 2011, **5**, 4720–4728.
- 101 X. Fang, X. Yu, S. Liao, Y. Shi, Y.-S. Hu, Z. Wang, G. D. Stucky and L. Chen, *Microporous Mesoporous Mater.*, 2012, **151**, 418–423.

- 102 C. Zhao, X. Wang, J. Kong, J. M. Ang, P. S. Lee, Z. Liu and X. Lu, *ACS Appl. Mater. Interfaces*, 2016, **8**, 2372–2379.
- 103 R. Acharya and K. Parida, *J. Environ. Chem. Eng.*, 2020, **8**, 103896.
- 104 K. Pramoda, U. Gupta, M. Chhetri, A. Bandyopadhyay, S. K. Pati and C. N. Rao, *ACS Appl. Mater. Interfaces*, 2017, **9**, 10664–10672.
- 105 R. Kumar, V. M. Suresh, T. K. Maji and C. N. Rao, *Chem. Commun.*, 2014, **50**, 2015–2017.
- 106 R. Singh, U. Gupta, V. S. Kumar, M. M. Ayyub, U. V. Waghmare and C. N. R. Rao, *ChemPhysChem*, 2019, **20**, 1728–1737.
- 107 B. V. Lotsch, *Annu. Rev. Mater. Res.*, 2015, **45**, 85–109.
- 108 L. A. Ponomarenko, A. K. Geim, A. A. Zhukov, R. Jalil, S. V. Morozov, K. S. Novoselov, I. V. Grigorieva, E. H. Hill, V. V. Cheianov, V. I. Fal'ko, K. Watanabe, T. Taniguchi and R. V. Gorbachev, *Nat. Phys.*, 2011, **7**, 958–961.
- 109 A. K. Geim and I. V. Grigorieva, *Nature*, 2013, **499**, 419–425.
- 110 S. Z. Butler, S. M. Hollen, L. Cao, Y. Cui, J. A. Gupta, H. R. Gutiérrez, T. F. Heinz, S. S. Hong, J. Huang, A. F. Ismach, E. Johnston-Halperin, M. Kuno, V. V. Plashnitsa, R. D. Robinson, R. S. Ruoff, S. Salahuddin, J. Shan, L. Shi, M. G. Spencer, M. Terrones, W. Windl and J. E. Goldberger, *ACS Nano*, 2013, **7**, 2898–2926.
- 111 Y. Fang, Y. Lv, F. Gong, A. A. Elzatahry, G. Zheng and D. Zhao, *Adv. Mater.*, 2016, **28**, 9385–9390.
- 112 T. Roy, M. Tosun, M. Hettick, G. H. Ahn, C. Hu and A. Javey, *Appl. Phys. Lett.*, 2016, **108**, 083111.
- 113 C. Chen, Z. Feng, Y. Feng, Y. Yue, C. Qin, D. Zhang and W. Feng, *ACS Appl. Mater. Interfaces*, 2016, **8**, 19004–19011.
- 114 X. Yuan, L. Tang, S. Liu, P. Wang, Z. Chen, C. Zhang, Y. Liu, W. Wang, Y. Zou, C. Liu, N. Guo, J. Zou, P. Zhou, W. Hu and F. Xiu, *Nano Lett.*, 2015, **15**, 3571–3577.
- 115 W. Hao, C. Marichy and C. Journet, *2D Mater.*, 2018, **6**, 012001.
- 116 X. Wan, K. Chen, Z. Chen, F. Xie, X. Zeng, W. Xie, J. Chen and J. Xu, *Adv. Funct. Mater.*, 2017, **27**, 1603998.
- 117 W.-J. Ong, L.-L. Tan, S.-P. Chai, S.-T. Yong and A. R. Mohamed, *Nano Energy*, 2015, **13**, 757–770.
- 118 H. Hwang, P. Joo, M. S. Kang, G. Ahn, J. T. Han, B.-S. Kim and J. H. Cho, *ACS Nano*, 2012, **6**, 2432–2440.
- 119 C. Liu, X. Huang, J. Liu, J. Wang, Z. Chen, R. Luo, C. Wang, J. Li, L. Wang, J. Wan and C. Yu, *Adv. Sci.*, 2020, **7**, 1901480.
- 120 Y. L. Huang, Y. J. Zheng, Z. Song, D. Chi, A. T. S. Wee and S. Y. Quek, *Chem. Soc. Rev.*, 2018, **47**, 3241–3264.
- 121 R. Mas-Ballesté, C. Gómez-Navarro, J. Gómez-Herrero and F. Zamora, *Nanoscale*, 2011, **3**, 20–30.
- 122 P. A. Vermeulen, J. Mulder, J. Momand and B. J. Kooi, *Nanoscale*, 2018, **10**, 1474–1480.
- 123 L. A. Walsh and C. L. Hinkle, *Appl. Mater. Today*, 2017, **9**, 504–515.
- 124 Y.-C. Lin, R. K. Ghosh, R. Addou, N. Lu, S. M. Eichfeld, H. Zhu, M.-Y. Li, X. Peng, M. J. Kim, L.-J. Li, R. M. Wallace, S. Datta and J. A. Robinson, *Nat. Commun.*, 2015, **6**, 7311.
- 125 Z. Cai, B. Liu, X. Zou and H.-M. Cheng, *Chem. Rev.*, 2018, **118**, 6091–6133.
- 126 P. K. Sahoo, S. Memaran, Y. Xin, L. Balicas and H. R. Gutiérrez, *Nature*, 2018, **553**, 63–67.
- 127 H. Heo, J. H. Sung, J.-H. Ahn, F. Ghahari, T. Taniguchi, K. Watanabe, P. Kim and M.-H. Jo, *Adv. Electron. Mater.*, 2017, **3**, 1600375.
- 128 S. Bertolazzi, D. Krasnozhan and A. Kis, *ACS Nano*, 2013, **7**, 3246–3252.
- 129 R. W. Johnson, A. Hultqvist and S. F. Bent, *Mater. Today*, 2014, **17**, 236–246.
- 130 R. Browning, P. Plachinda, P. Padigi, R. Solanki and S. Rouvimov, *Nanoscale*, 2016, **8**, 2143–2148.
- 131 H.-K. Hong, J. Jo, D. Hwang, J. Lee, N. Y. Kim, S. Son, J. H. Kim, M.-J. Jin, Y. C. Jun, R. Erni, S. K. Kwak, J.-W. Yoo and Z. Lee, *Nano Lett.*, 2017, **17**, 120–127.
- 132 M. Karbalaee Akbari, Z. Hai, Z. Wei, C. Detavernier, E. Solano, F. Verpoort and S. Zhuiykov, *ACS Appl. Mater. Interfaces*, 2018, **10**, 10304–10314.
- 133 M. Karbalaee Akbari, J. Hu, F. Verpoort, H. Lu and S. Zhuiykov, *Nanomicro Lett.*, 2020, **12**, 83.
- 134 Y. Kim, D. Choi, W. J. Woo, J. B. Lee, G. H. Ryu, J. H. Lim, S. Lee, Z. Lee, S. Im, J.-H. Ahn, W.-H. Kim, J. Park and H. Kim, *Appl. Surf. Sci.*, 2019, **494**, 591–599.
- 135 A. J. Mannix, X. F. Zhou, B. Kiraly, J. D. Wood, D. Alducin, B. D. Myers, X. Liu, B. L. Fisher, U. Santiago, J. R. Guest, M. J. Yacaman, A. Ponce, A. R. Oganov, M. C. Hersam and N. P. Guisinger, *Science*, 2015, **350**, 1513–1516.
- 136 C. Muratore, A. A. Voevodin and N. R. Glavin, *Thin Solid Films*, 2019, **688**, 137500.
- 137 A. Bailini, F. Donati, M. Zamboni, V. Russo, M. Passoni, C. S. Casari, A. Li Bassi and C. E. Bottani, *Appl. Surf. Sci.*, 2007, **254**, 1249–1254.
- 138 Z. Yang, Z. Wu, Y. Lyu and J. Hao, *InfoMat*, 2019, **1**, 98–107.
- 139 S. Seo, S. Kim, H. Choi, J. Lee, H. Yoon, G. Piao, J.-C. Park, Y. Jung, J. Song, S. Y. Jeong, H. Park and S. Lee, *Adv. Sci.*, 2019, **6**, 1900301.
- 140 F. Ullah, Y. Sim, C. T. Le, M.-J. Seong, J. I. Jang, S. H. Rhim, B. C. Tran Khac, K.-H. Chung, K. Park, Y. Lee, K. Kim, H. Y. Jeong and Y. S. Kim, *ACS Nano*, 2017, **11**, 8822–8829.
- 141 B. Li, L. Ding, P. Gui, N. Liu, Y. Yue, Z. Chen, Z. Song, J. Wen, H. Lei, Z. Zhu, X. Wang, M. Su, L. Liao, Y. Gao, D. Zhang and G. Fang, *Adv. Mater. Interfaces*, 2019, **6**, 1901156.
- 142 M. I. Serna, S. M. N. Hasan, S. Nam, L. El Bouanani, S. Moreno, H. Choi, H. N. Alshareef, M. Minary-Jolandan and M. A. Quevedo-Lopez, *Adv. Mater. Interfaces*, 2018, **5**, 1800128.
- 143 J. D. Yao, Z. Q. Zheng and G. W. Yang, *Prog. Mater. Sci.*, 2019, **106**, 100573.
- 144 Q. Zhang, Y. Chen, C. Zhang, C.-R. Pan, M.-Y. Chou, C. Zeng and C.-K. Shih, *Nat. Commun.*, 2016, **7**, 13843.
- 145 J. M. Wofford, S. Nakhaie, T. Krause, X. Liu, M. Ramsteiner, M. Hanke, H. Riechert and J. M. J. Lopes, *Sci. Rep.*, 2017, **7**, 43644.
- 146 S. Vishwanath, X. Liu, S. Rouvimov, L. Basile, N. Lu, A. Azcatl, K. Magno, R. M. Wallace, M. Kim, J.-C. Idrobo, J. K. Furdyna, D. Jena and H. G. Xing, *J. Mater. Res.*, 2016, **31**, 900–910.

- 147 K. E. Aretouli, D. Tsoutsou, P. Tsipas, J. Marquez-Velasco, S. Aminalragia Giamini, N. Kelaidis, V. Psycharis and A. Dimoulas, *ACS Appl. Mater. Interfaces*, 2016, **8**, 23222–23229.
- 148 D. Tsoutsou, K. E. Aretouli, P. Tsipas, J. Marquez-Velasco, E. Xenogiannopoulou, N. Kelaidis, S. Aminalragia Giamini and A. Dimoulas, *ACS Appl. Mater. Interfaces*, 2016, **8**, 1836–1841.
- 149 A. Roy, H. C. P. Movva, B. Satpati, K. Kim, R. Dey, A. Rai, T. Pramanik, S. Guchhait, E. Tutuc and S. K. Banerjee, *ACS Appl. Mater. Interfaces*, 2016, **8**, 7396–7402.
- 150 J. N. Tiwari, R. N. Tiwari and K. S. Kim, *Prog. Mater. Sci.*, 2012, **57**, 724–803.
- 151 Z. Zhang, C. Feng, C. Liu, M. Zuo, L. Qin, X. Yan, Y. Xing, H. Li, R. Si, S. Zhou and J. Zeng, *Nat. Commun.*, 2020, **11**, 1215.
- 152 A. I. Pruna, N. M. Rosas-Laverde and D. Busquets Mataix, *Materials*, 2020, **13**, 624.
- 153 Q. Fu and X. Bao, *Chem. Soc. Rev.*, 2017, **46**, 1842–1874.
- 154 S. Cao, B. Shen, T. Tong, J. Fu and J. Yu, *Adv. Funct. Mater.*, 2018, **28**, 1800136.
- 155 Z. Yao, H. Sun, H. Sui and X. Liu, *Nanoscale Res. Lett.*, 2020, **15**, 78.
- 156 Y. Li, Z. Yin, G. Ji, Z. Liang, Y. Xue, Y. Guo, J. Tian, X. Wang and H. Cui, *Appl. Catal., B*, 2019, **246**, 12–20.
- 157 D. Jiang, T. Wang, Q. Xu, D. Li, S. Meng and M. Chen, *Appl. Catal., B*, 2017, **201**, 617–628.
- 158 A. Bafaqeer, M. Tahir and N. A. S. Amin, *Chem. Eng. J.*, 2018, **334**, 2142–2153.
- 159 R. Zhong, Z. Zhang, H. Yi, L. Zeng, C. Tang, L. Huang and M. Gu, *Appl. Catal., B*, 2018, **237**, 1130–1138.
- 160 W. Xu, W. Liu, J. F. Schmidt, W. Zhao, X. Lu, T. Raab, C. Diederichs, W. Gao, D. V. Seletskiy and Q. Xiong, *Nature*, 2017, **541**, 62–67.
- 161 P. Rivera, K. L. Seyler, H. Yu, J. R. Schaibley, J. Yan, D. G. Mandrus, W. Yao and X. Xu, *Science*, 2016, **351**, 688–691.
- 162 J. Wierzbowski, J. Klein, F. Sigger, C. Straubinger, M. Kremser, T. Taniguchi, K. Watanabe, U. Wurstbauer, A. W. Holleitner, M. Kaniber, K. Müller and J. J. Finley, *Sci. Rep.*, 2017, **7**, 12383.
- 163 T. Lee, S. H. Min, M. Gu, Y. K. Jung, W. Lee, J. U. Lee, D. G. Seong and B.-S. Kim, *Chem. Mater.*, 2015, **27**, 3785–3796.
- 164 M. Yang, Y. Hou and N. A. Kotov, *Nano Today*, 2012, **7**, 430–447.
- 165 B. S. Shim, P. Podsiadlo, D. G. Lilly, A. Agarwal, J. Lee, Z. Tang, S. Ho, P. Ingle, D. Paterson, W. Lu and N. A. Kotov, *Nano Lett.*, 2007, **7**, 3266–3273.
- 166 Y. Fu, S.-J. Li, J. Xu, M. Yang, J.-D. Zhang, Y.-H. Jiao, J.-C. Zhang, K. Zhang and Y.-G. Jia, *Langmuir*, 2011, **27**, 672–677.
- 167 K. C. Krogman, J. L. Lowery, N. S. Zacharia, G. C. Rutledge and P. T. Hammond, *Nat. Mater.*, 2009, **8**, 512–518.
- 168 S. Y. Kim, J. Hong, R. Kavian, S. W. Lee, M. N. Hyder, Y. Shao-Horn and P. T. Hammond, *Energy Environ. Sci.*, 2013, **6**, 888–897.
- 169 E. Kharlampieva, V. Kozlovskaya, J. Chan, J. F. Ankner and V. V. Tsukruk, *Langmuir*, 2009, **25**, 14017–14024.
- 170 K. Ariga, Y. Yamauchi, T. Mori and J. P. Hill, *Adv. Mater.*, 2013, **25**, 6477–6512.
- 171 M. Muramatsu, K. Akatsuka, Y. Ebina, K. Wang, T. Sasaki, T. Ishida, K. Miyake and M.-A. Haga, *Langmuir*, 2005, **21**, 6590–6595.
- 172 S. Patil, A. Harle, S. Sathaye and K. Patil, *CrystEngComm*, 2014, **16**, 10845–10855.
- 173 A. V. Kretinin, Y. Cao, J. S. Tu, G. L. Yu, R. Jalil, K. S. Novoselov, S. J. Haigh, A. Gholinia, A. Mishchenko, M. Lozada, T. Georgiou, C. R. Woods, F. Withers, P. Blake, G. Eda, A. Wirsig, C. Hucho, K. Watanabe, T. Taniguchi, A. K. Geim and R. V. Gorbachev, *Nano Lett.*, 2014, **14**, 3270–3276.
- 174 M.-H. Chiu, M.-Y. Li, W. Zhang, W.-T. Hsu, W.-H. Chang, M. Terrones, H. Terrones and L.-J. Li, *ACS Nano*, 2014, **8**, 9649–9656.
- 175 K. Lan, Q. Wei, R. Wang, Y. Xia, S. Tan, Y. Wang, A. Elzatahry, P. Feng, L. Mai and D. Zhao, *J. Am. Chem. Soc.*, 2019, **141**, 16755–16762.
- 176 H. Wang, Z. Zeng, P. Xu, L. Li, G. Zeng, R. Xiao, Z. Tang, D. Huang, L. Tang, C. Lai, D. Jiang, Y. Liu, H. Yi, L. Qin, S. Ye, X. Ren and W. Tang, *Chem. Soc. Rev.*, 2019, **48**, 488–516.
- 177 W. Li, Z. Lin and G. Yang, *Nanoscale*, 2017, **9**, 18290–18298.
- 178 J. Yan, C. E. Ren, K. Maleski, C. B. Hatter, B. Anasori, P. Urbankowski, A. Sarycheva and Y. Gogotsi, *Adv. Funct. Mater.*, 2017, **27**, 1701264.
- 179 T. Su, Z. D. Hood, M. Naguib, L. Bai, S. Luo, C. M. Rouleau, I. N. Ivanov, H. Ji, Z. Qin and Z. Wu, *Nanoscale*, 2019, **11**, 8138–8149.
- 180 C. Liu, M. Xiong, B. Chai, J. Yan, G. Fan and G. Song, *Catal. Sci. Technol.*, 2019, **9**, 6929–6937.
- 181 R. A. Marcus, *Annu. Rev. Phys. Chem.*, 1964, **15**, 155–196.
- 182 C. Zhang, B.-H. Wu, M.-Q. Ma, Z. Wang and Z.-K. Xu, *Chem. Soc. Rev.*, 2019, **48**, 3811–3841.
- 183 D. Rajwar, X. Sun, S. J. Cho, A. C. Grimsdale and D. Fichou, *CrystEngComm*, 2012, **14**, 5182–5187.
- 184 M.-A. Carvalho, H. Dekkiche, L. Karmazin, F. Sanchez, B. Vincent, M. Kaneshato, Y. Kikkawa and R. Ruppert, *Inorg. Chem.*, 2017, **56**, 15081–15090.
- 185 P. C. Ball and R. Evans, *J. Chem. Phys.*, 1988, **89**, 4412–4423.
- 186 M. Zhao, Y. Huang, Y. Peng, Z. Huang, Q. Ma and H. Zhang, *Chem. Soc. Rev.*, 2018, **47**, 6267–6295.
- 187 C. N. R. Rao, K. Pramoda and R. Kumar, *Chem. Commun.*, 2017, **53**, 10093–10107.
- 188 J. Zhang, Y. Chen and X. Wang, *Energy Environ. Sci.*, 2015, **8**, 3092–3108.
- 189 W. Zhou, Y.-P. Wu, X. Wang, J.-W. Tian, D.-D. Huang, J. Zhao, Y.-Q. Lan and D.-S. Li, *CrystEngComm*, 2018, **20**, 4804–4809.
- 190 Y. Gong, S. Lei, G. Ye, B. Li, Y. He, K. Keyshar, X. Zhang, Q. Wang, J. Lou, Z. Liu, R. Vajtai, W. Zhou and P. M. Ajayan, *Nano Lett.*, 2015, **15**, 6135–6141.
- 191 E. M. Alexeev, A. Catanzaro, O. V. Skrypka, P. K. Nayak, S. Ahn, S. Pak, J. Lee, J. I. Sohn, K. S. Novoselov, H. S. Shin and A. I. Tartakovskii, *Nano Lett.*, 2017, **17**, 5342–5349.
- 192 H.-K. He, R. Yang, H.-M. Huang, F.-F. Yang, Y.-Z. Wu, J. Shaibo and X. Guo, *Nanoscale*, 2020, **12**, 380–387.

- 193 L. Ding, M. S. Ukhtary, M. Chubarov, T. H. Choudhury, F. Zhang, R. Yang, A. Zhang, J. A. Fan, M. Terrones, J. M. Redwing, T. Yang, M. Li, R. Saito and S. Huang, *IEEE Trans. Electron Devices*, 2018, **65**, 4059–4067.
- 194 C. Zhang, C. P. Chuu, X. Ren, M. Y. Li, L. J. Li, C. Jin, M. Y. Chou and C. K. Shih, *Sci. Adv.*, 2017, **3**, e1601459.
- 195 Y. Zhang, L. Yin, J. Chu, T. A. Shifa, J. Xia, F. Wang, Y. Wen, X. Zhan, Z. Wang and J. He, *Adv. Mater.*, 2018, **30**, 1803665.
- 196 C. Neumann, L. Banszerus, M. Schmitz, S. Reichardt, J. Sonntag, T. Taniguchi, K. Watanabe, B. Beschoten and C. Stampfer, *Phys. Status Solidi B*, 2016, **253**, 2326–2330.
- 197 C. Xu, S. Song, Z. Liu, L. Chen, L. Wang, D. Fan, N. Kang, X. Ma, H.-M. Cheng and W. Ren, *ACS Nano*, 2017, **11**, 5906–5914.
- 198 Y. Tan, L. Ma, Z. Gao, M. Chen and F. Chen, *Nano Lett.*, 2017, **17**, 2621–2626.
- 199 J. Seo, J. Lee, Y. Kim, D. Koo, G. Lee and H. Park, *Nano Lett.*, 2020, **20**, 1620–1630.
- 200 K. Chen, X. Wan, J. Wen, W. Xie, Z. Kang, X. Zeng, H. Chen and J.-B. Xu, *ACS Nano*, 2015, **9**, 9868–9876.
- 201 F. Ceballos, M. Z. Bellus, H.-Y. Chiu and H. Zhao, *ACS Nano*, 2014, **8**, 12717–12724.
- 202 P. Rivera, J. R. Schaibley, A. M. Jones, J. S. Ross, S. Wu, G. Aivazian, P. Klement, K. Seyler, G. Clark, N. J. Ghimire, J. Yan, D. G. Mandrus, W. Yao and X. Xu, *Nat. Commun.*, 2015, **6**, 6242.
- 203 K. Liu, L. Zhang, T. Cao, C. Jin, D. Qiu, Q. Zhou, A. Zettl, P. Yang, S. G. Louie and F. Wang, *Nat. Commun.*, 2014, **5**, 4966.
- 204 K. Liu, Q. Yan, M. Chen, W. Fan, Y. Sun, J. Suh, D. Fu, S. Lee, J. Zhou, S. Tongay, J. Ji, J. B. Neaton and J. Wu, *Nano Lett.*, 2014, **14**, 5097–5103.
- 205 B. Li, L. Huang, M. Zhong, Y. Li, Y. Wang, J. Li and Z. Wei, *Adv. Electron. Mater.*, 2016, **2**, 1600298.
- 206 H. Yamaguchi and Y. Hirayama, *Jpn. J. Appl. Phys.*, 1998, **37**, L899–L901.
- 207 H. M. Hill, A. F. Rigosi, K. T. Rim, G. W. Flynn and T. F. Heinz, *Nano Lett.*, 2016, **16**, 4831–4837.
- 208 C. R. Woods, L. Britnell, A. Eckmann, R. S. Ma, J. C. Lu, H. M. Guo, X. Lin, G. L. Yu, Y. Cao, R. V. Gorbachev, A. V. Kretinin, J. Park, L. A. Ponomarenko, M. I. Katsnelson, Y. N. Gornostyrev, K. Watanabe, T. Taniguchi, C. Casiraghi, H. J. Gao, A. K. Geim and K. S. Novoselov, *Nat. Phys.*, 2014, **10**, 451–456.
- 209 C. H. Naylor, W. M. Parkin, Z. Gao, J. Berry, S. Zhou, Q. Zhang, J. B. McClimon, L. Z. Tan, C. E. Kehayias, M.-Q. Zhao, R. S. Gona, R. W. Carpick, A. M. Rappe, D. J. Srolovitz, M. Drndic and A. T. C. Johnson, *ACS Nano*, 2017, **11**, 8619–8627.
- 210 E. Stolyarova, K. T. Rim, S. Ryu, J. Maultzsch, P. Kim, L. E. Brus, T. F. Heinz, M. S. Hybertsen and G. W. Flynn, *Proc. Natl. Acad. Sci. U. S. A.*, 2007, **104**, 9209–9212.
- 211 X. Wu, R. Ge, P.-A. Chen, H. Chou, Z. Zhang, Y. Zhang, S. Banerjee, M.-H. Chiang, J. C. Lee and D. Akinwande, *Adv. Mater.*, 2019, **31**, 1806790.
- 212 J. Zhang, L. Du, S. Feng, R.-W. Zhang, B. Cao, C. Zou, Y. Chen, M. Liao, B. Zhang, S. A. Yang, G. Zhang and T. Yu, *Nat. Commun.*, 2019, **10**, 4226.
- 213 M. Heilmann, M. Bashouti, H. Riechert and J. M. J. Lopes, *2D Mater.*, 2018, **5**, 025004.
- 214 W. Yu, S. Li, Y. Zhang, W. Ma, T. Sun, J. Yuan, K. Fu and Q. Bao, *Small*, 2017, **13**, 1700268.
- 215 N. Zhou, R. Wang, X. Zhou, H. Song, X. Xiong, Y. Ding, J. Lü, L. Gan and T. Zhai, *Small*, 2018, **14**, 1702731.
- 216 G. Wang, L. Li, W. Fan, R. Wang, S. Zhou, J.-T. Lü, L. Gan and T. Zhai, *Adv. Funct. Mater.*, 2018, **28**, 1800339.
- 217 J. Liang, C. Ding, J. Liu, T. Chen, W. Peng, Y. Li, F. Zhang and X. Fan, *Nanoscale*, 2019, **11**, 10992–11000.
- 218 J. Fu, Q. Xu, J. Low, C. Jiang and J. Yu, *Appl. Catal., B*, 2019, **243**, 556–565.
- 219 F. Dong, T. Xiong, Y. Sun, Y. Zhang and Y. Zhou, *Chem. Commun.*, 2015, **51**, 8249–8252.
- 220 Z. Kou, T. Wang, Q. Gu, M. Xiong, L. Zheng, X. Li, Z. Pan, H. Chen, F. Verpoort, A. K. Cheetham, S. Mu and J. Wang, *Adv. Energy Mater.*, 2019, **9**, 1803768.
- 221 M. Zhu, Z. Sun, M. Fujitsuka and T. Majima, *Angew. Chem., Int. Ed.*, 2018, **57**, 2160–2164.
- 222 Y. Liu, Z. Gao, Y. Tan and F. Chen, *ACS Nano*, 2018, **12**, 10529–10536.
- 223 Z. Sun, Z. Yu, Y. Liu, C. Shi, M. Zhu and A. Wang, *J. Colloid Interface Sci.*, 2019, **533**, 251–258.
- 224 M.-Q. Yang, J. Dan, S. J. Pennycook, X. Lu, H. Zhu, Q.-H. Xu, H. J. Fan and G. W. Ho, *Mater. Horiz.*, 2017, **4**, 885–894.
- 225 J. Wang, R. Gao, L. Zheng, Z. Chen, Z. Wu, L. Sun, Z. Hu and X. Liu, *ACS Catal.*, 2018, **8**, 8953–8960.
- 226 X. Liu, Z. Wei, I. Balla, A. J. Mannix, N. P. Guisinger, E. Luijten and M. C. Hersam, *Sci. Adv.*, 2017, **3**, e1602356.
- 227 J. Lin, P. Wang, H. Wang, C. Li, X. Si, J. Qi, J. Cao, Z. Zhong, W. Fei and J. Feng, *Adv. Sci.*, 2019, **6**, 1900246.
- 228 L. Tao, K. Chen, Z. Chen, W. Chen, X. Gui, H. Chen, X. Li and J.-B. Xu, *ACS Appl. Mater. Interfaces*, 2017, **9**, 12073–12081.
- 229 L. Li, Y. Zheng, S. Zhang, J. Yang, Z. Shao and Z. Guo, *Energy Environ. Sci.*, 2018, **11**, 2310–2340.
- 230 W. Huh, S. Jang, J. Y. Lee, D. Lee, D. Lee, J. M. Lee, H.-G. Park, J. C. Kim, H. Y. Jeong, G. Wang and C.-H. Lee, *Adv. Mater.*, 2018, **30**, 1801447.
- 231 P. Simon, Y. Gogotsi and B. Dunn, *Science*, 2014, **343**, 1210–1211.
- 232 K. Naoi, W. Naoi, S. Aoyagi, J.-i. Miyamoto and T. Kamino, *Acc. Chem. Res.*, 2013, **46**, 1075–1083.
- 233 K. Naoi, S. Ishimoto, Y. Isobe and S. Aoyagi, *J. Power Sources*, 2010, **195**, 6250–6254.
- 234 T. Yuan, Z. Tan, C. Ma, J. Yang, Z.-F. Ma and S. Zheng, *Adv. Energy Mater.*, 2017, **7**, 1601625.
- 235 S. H. Woo, Y. Park, W. Y. Choi, N.-S. Choi, S. Nam, B. Park and K. T. Lee, *J. Electrochem. Soc.*, 2012, **159**, A2016–A2023.
- 236 M. Ma, S. Zhang, Y. Yao, H. Wang, H. Huang, R. Xu, J. Wang, X. Zhou, W. Yang, Z. Peng, X. Wu, Y. Hou and Y. Yu, *Adv. Mater.*, 2020, **32**, 2000958.
- 237 P. Xiong, R. Ma, N. Sakai and T. Sasaki, *ACS Nano*, 2018, **12**, 1768–1777.
- 238 C. Wang, F. Liu, J. Chen, Z. Yuan, C. Liu, X. Zhang, M. Xu, L. Wei and Y. Chen, *Energy Storage Mater.*, 2020, **32**, 448–457.

- 239 Y. Hou, J. Li, Z. Wen, S. Cui, C. Yuan and J. Chen, *Nano Energy*, 2014, **8**, 157–164.
- 240 B. Chen, Y. Meng, F. He, E. Liu, C. Shi, C. He, L. Ma, Q. Li, J. Li and N. Zhao, *Nano Energy*, 2017, **41**, 154–163.
- 241 E. Xu, Y. Zhang, H. Wang, Z. Zhu, J. Quan, Y. Chang, P. Li, D. Yu and Y. Jiang, *Chem. Eng. J.*, 2020, **385**, 123839.
- 242 X. Wang, H. Li, H. Li, S. Lin, J. Bai, J. Dai, C. Liang, X. Zhu, Y. Sun and S. Dou, *J. Mater. Chem. A*, 2019, **7**, 2291–2300.
- 243 P. Nakhanivej, X. Yu, S. K. Park, S. Kim, J.-Y. Hong, H. J. Kim, W. Lee, J. Y. Hwang, J. E. Yang, C. Wolverton, J. Kong, M. Chhowalla and H. S. Park, *Nat. Mater.*, 2019, **18**, 156–162.
- 244 H. Niu, X. Yang, Q. Wang, X. Jing, K. Cheng, K. Zhu, K. Ye, G. Wang, D. Cao and J. Yan, *J. Energy Chem.*, 2020, **46**, 105–113.
- 245 M. Mohiuddin, A. Zavabeti, F. Haque, A. Mahmood, R. S. Datta, N. Syed, M. W. Khan, A. Jannat, K. Messalea, B. Y. Zhang, G. Chen, H. Zhang, J. Z. Ou and N. Mahmood, *J. Mater. Chem. A*, 2020, **8**, 2789–2797.
- 246 M. W. Khan, S. Loomba, R. Ali, M. Mohiuddin, A. Alluqmani, F. Haque, Y. Liu, R. U. R. Sagar, A. Zavabeti, T. Alkathiri, B. Shabbir, X. Jian, J. Z. Ou, A. Mahmood and N. Mahmood, *Front. Chem.*, 2020, **8**, 733.
- 247 B. Kim, T. Kim, K. Lee and J. Li, *ChemElectroChem*, 2020, **7**, 3578–3589.
- 248 J. Zhang, C. Si, T. Kou, J. Wang and Z. Zhang, *Sustainable Energy Fuels*, 2020, **4**, 2625–2637.
- 249 M. S. Burke, L. J. Enman, A. S. Batchellor, S. Zou and S. W. Boettcher, *Chem. Mater.*, 2015, **27**, 7549–7558.
- 250 A. Pandey, A. Mukherjee, S. Chakrabarty, D. Chanda and S. Basu, *ACS Appl. Mater. Interfaces*, 2019, **11**, 42094–42103.
- 251 I. S. Amiin, Z. Pu, X. Liu, K. A. Owusu, H. G. R. Monestel, F. O. Boakye, H. Zhang and S. Mu, *Adv. Funct. Mater.*, 2017, **27**, 1702300.
- 252 N. Li, Y. Zhang, M. Jia, X. Lv, X. Li, R. Li, X. Ding, Y.-Z. Zheng and X. Tao, *Electrochim. Acta*, 2019, **326**, 134976.
- 253 X. Xiao, D. Huang, Y. Fu, M. Wen, X. Jiang, X. Lv, M. Li, L. Gao, S. Liu, M. Wang, C. Zhao and Y. Shen, *ACS Appl. Mater. Interfaces*, 2018, **10**, 4689–4696.
- 254 D. Zhang, H. Mou, F. Lu, C. Song and D. Wang, *Appl. Catal., B*, 2019, **254**, 471–478.
- 255 Y. Jia, L. Zhang, G. Gao, H. Chen, B. Wang, J. Zhou, M. T. Soo, M. Hong, X. Yan, G. Qian, J. Zou, A. Du and X. Yao, *Adv. Mater.*, 2017, **29**, 1700017.
- 256 W. Jin, J. Chen, B. Liu, J. Hu, Z. Wu, W. Cai and G. Fu, *Small*, 2019, **15**, 1904210.
- 257 Y. Guo, J. Tang, H. Qian, Z. Wang and Y. Yamauchi, *Chem. Mater.*, 2017, **29**, 5566–5573.
- 258 Y. P. Zhu, T. Y. Ma, M. Jaroniec and S. Z. Qiao, *Angew. Chem., Int. Ed.*, 2017, **56**, 1324–1328.
- 259 S. Liu, Y. Yin, M. Wu, K. S. Hui, K. N. Hui, C.-Y. Ouyang and S. C. Jun, *Small*, 2019, **15**, 1803984.
- 260 X. Zhang, J.-P. Veder, S. He and S. P. Jiang, *Chem. Commun.*, 2019, **55**, 1233–1236.
- 261 J. Jia, Q. Zhang, Z. Li, X. Hu, E. Liu and J. Fan, *J. Mater. Chem. A*, 2019, **7**, 3828–3841.
- 262 X. Yan, Y. Jia, T. Odedairo, X. Zhao, Z. Jin, Z. Zhu and X. Yao, *Chem. Commun.*, 2016, **52**, 8156–8159.
- 263 X. Yan, Y. Jia and X. Yao, *Chem. Soc. Rev.*, 2018, **47**, 7628–7658.
- 264 L. An, Z. Zhang, J. Feng, F. Lv, Y. Li, R. Wang, M. Lu, R. B. Gupta, P. Xi and S. Zhang, *J. Am. Chem. Soc.*, 2018, **140**, 17624–17631.
- 265 L. Hui, Y. Xue, B. Huang, H. Yu, C. Zhang, D. Zhang, D. Jia, Y. Zhao, Y. Li, H. Liu and Y. Li, *Nat. Commun.*, 2018, **9**, 5309.
- 266 C. Qin, A. Fan, X. Zhang, S. Wang, X. Yuan and X. Dai, *J. Mater. Chem. A*, 2019, **7**, 27594–27602.
- 267 A. Bag and N.-E. Lee, *J. Mater. Chem. C*, 2019, **7**, 13367–13383.
- 268 N. Joshi, T. Hayasaka, Y. Liu, H. Liu, O. N. Oliveira and L. Lin, *Microchim. Acta*, 2018, **185**, 213.
- 269 L. Reyes, A. Hoel, S. Saukko, P. Heszler, V. Lantto and C. G. Granqvist, *Sens. Actuators, B*, 2006, **117**, 128–134.
- 270 S. Ray, *Sens. Actuators, B*, 2016, **222**, 492–498.
- 271 S. Zhao, J. Xue and W. Kang, *Chem. Phys. Lett.*, 2014, **595**, 35–42.
- 272 Y. Zeng, S. Lin, D. Gu and X. Li, *Nanomaterials*, 2018, **8**, 851.
- 273 S. Cui, H. Pu, S. A. Wells, Z. Wen, S. Mao, J. Chang, M. C. Hersam and J. Chen, *Nat. Commun.*, 2015, **6**, 8632.
- 274 J. M. Walker, S. A. Akbar and P. A. Morris, *Sens. Actuators, B*, 2019, **286**, 624–640.
- 275 G. Lee, S. Kim, S. Jung, S. Jang and J. Kim, *Sens. Actuators, B*, 2017, **250**, 569–573.
- 276 J. Y. Kwak, J. Hwang, B. Calderon, H. Alsalman, N. Munoz, B. Schutter and M. G. Spencer, *Nano Lett.*, 2014, **14**, 4511–4516.
- 277 B. Cho, J. Yoon, S. K. Lim, A. R. Kim, D.-H. Kim, S.-G. Park, J.-D. Kwon, Y.-J. Lee, K.-H. Lee and B. H. Lee, *ACS Appl. Mater. Interfaces*, 2015, **7**, 16775–16780.
- 278 H. Tabata, Y. Sato, K. Oi, O. Kubo and M. J. A. M. Katayama, *ACS Appl. Mater. Interfaces*, 2018, **10**, 38387–38393.
- 279 F. A. de Souza, G. Sivaraman, J. Hertkorn, R. G. Amorim, M. Fyta and W. L. Scopel, *J. Mater. Chem. A*, 2019, **7**, 8905–8911.
- 280 A. N. Abbas, B. Liu, L. Chen, Y. Ma, S. Cong, N. Aroonyadet, M. Köpf, T. Nilges and C. Zhou, *ACS Nano*, 2015, **9**, 5618–5624.
- 281 S. Shi, R. Hu, E. Wu, Q. Li, X. Chen, W. Guo, C. Sun, X. Hu, D. Zhang and J. Liu, *Nanotechnology*, 2018, **29**, 435502.
- 282 J. Z. Ou, W. Ge, B. Carey, T. Daeneke, A. Rotbart, W. Shan, Y. Wang, Z. Fu, A. F. Chrimes and W. Wlodarski, *ACS Nano*, 2015, **9**, 10313–10323.
- 283 X. Wang, Z. Wang, J. Zhang, X. Wang, Z. Zhang, J. Wang, Z. Zhu, Z. Li, Y. Liu, X. Hu, J. Qiu, G. Hu, B. Chen, N. Wang, Q. He, J. Chen, J. Yan, W. Zhang, T. Hasan, S. Li, H. Li, H. Zhang, Q. Wang, X. Huang and W. Huang, *Nat. Commun.*, 2018, **9**, 3611.
- 284 W. Y. Chen, X. Jiang, S.-N. Lai, D. Peroulis and L. Stanciu, *Nat. Commun.*, 2020, **11**, 1302.
- 285 S. Y. Park, Y. H. Kim, S. Y. Lee, W. Sohn, J. E. Lee, Y.-S. Shim, K. C. Kwon, K. S. Choi, H. J. Yoo and J. M. Suh, *J. Mater. Chem. A*, 2018, **6**, 5016–5024.
- 286 H. Wang, J. Bai, M. Dai, K. Liu, Y. Liu, L. Zhou, F. Liu, F. Liu, Y. Gao and X. Yan, *Sens. Actuators, B*, 2020, **304**, 127287.

- 287 A. Chen, R. Liu, X. Peng, Q. Chen and J. Wu, *ACS Appl. Mater. Interfaces*, 2017, **9**, 37191–37200.
- 288 Z. Feng, B. Chen, S. Qian, L. Xu, L. Feng, Y. Yu, R. Zhang, J. Chen, Q. Li and Q. Li, *2D Mater.*, 2016, **3**, 035021.
- 289 N. T. Hang, S. Zhang and W. Yang, *Sens. Actuators, B*, 2017, **248**, 940–948.
- 290 B. Cho, A. R. Kim, D. J. Kim, H.-S. Chung, S. Y. Choi, J.-D. Kwon, S. W. Park, Y. Kim, B. H. Lee and K. H. Lee, *ACS Appl. Mater. Interfaces*, 2016, **8**, 19635–19642.
- 291 S. Dhara, H. Jawa, S. Ghosh, A. Varghese and S. Lodha, 2020, arXiv preprint arXiv:11350.
- 292 H. K. Choi, J. Park, N. Myoung, H.-J. Kim, J. S. Choi, Y. K. Choi, C.-Y. Hwang, J. T. Kim, S. Park and Y. Yi, *Nanoscale*, 2017, **9**, 18644–18650.
- 293 D. Zhang, C. Jiang, J. Liu and Y. Cao, *Sens. Actuators, B*, 2017, **247**, 875–882.
- 294 A. Sinha, H. Zhao, Y. Huang, X. Lu, J. Chen and R. Jain, *Trends Anal. Chem.*, 2018, **105**, 424–435.
- 295 E. Lee, A. VahidMohammadi, B. C. Prorok, Y. S. Yoon, M. Beidaghi and D.-J. Kim, *ACS Appl. Mater. Interfaces*, 2017, **9**, 37184–37190.
- 296 S. Yang, C. Jiang and S.-H. Wei, *Appl. Phys. Rev.*, 2017, **4**, 021304.
- 297 R. Kumar, N. Goel and M. Kumar, *ACS Sens.*, 2017, **2**, 1744–1752.
- 298 Y. Huang, W. Jiao, Z. Chu, G. Ding, M. Yan, X. Zhong and R. Wang, *J. Mater. Chem. C*, 2019, **7**, 8616–8625.
- 299 W. Zheng, Y. Xu, L. Zheng, C. Yang, N. Pinna, X. Liu and J. Zhang, *Adv. Funct. Mater.*, 2020, **30**, 2000435.
- 300 D. Lee, H. Park, S. D. Han, S. H. Kim, W. Huh, J. Y. Lee, Y. S. Kim, M. J. Park, W. I. Park and C. Y. Kang, *Small*, 2019, **15**, 1804303.
- 301 Y. Kim, S. Lee, J. G. Song, K. Y. Ko, W. J. Woo, S. W. Lee, M. Park, H. Lee, Z. Lee and H. Choi, *Adv. Funct. Mater.*, 2020, 2003360.
- 302 W. Wen, Y. Song, X. Yan, C. Zhu, D. Du, S. Wang, A. M. Asiri and Y. Lin, *Mater. Today*, 2018, **21**, 164–177.
- 303 A. Bolotsky, D. Butler, C. Dong, K. Gerace, N. R. Glavin, C. Muratore, J. A. Robinson and A. Ebrahimi, *ACS Nano*, 2019, **13**, 9781–9810.
- 304 S. Gao, L. Yang and C. D. Spataru, *Nano Lett.*, 2017, **17**, 7809–7813.
- 305 J. Liu, X. Chen, Q. Wang, M. Xiao, D. Zhong, W. Sun, G. Zhang and Z. Zhang, *Nano Lett.*, 2019, **19**, 1437–1444.
- 306 C. Ménard-Moyon, A. Bianco and K. Kalantar-Zadeh, *ACS Sens.*, 2020, **5**, 3739–3769.
- 307 S. Tongay, J. Zhou, C. Ataca, J. Liu, J. S. Kang, T. S. Matthews, L. You, J. Li, J. C. Grossman and J. Wu, *Nano Lett.*, 2013, **13**, 2831–2836.
- 308 P. T. K. Loan, W. Zhang, C. T. Lin, K. H. Wei, L. J. Li and C. H. Chen, *Adv. Mater.*, 2014, **26**, 4838–4844.
- 309 S. Pal, N. Pal, Y. Prajapati and J. Saini, in *Layered 2D Advanced Materials and Their Allied Applications*, ed. R. Inamuddin, M. I. Boddula and A. M. A. Ahamed, John Wiley & Sons, USA, 2020, **5**, pp. 103–129.
- 310 A. K. Sharma, A. K. Pandey and B. Kaur, *Mater. Sci. Semicond. Process.*, 2019, **12**, 1542.
- 311 Y. Prajapati and A. Srivastava, *Superlattice. Microst.*, 2019, **129**, 152–162.
- 312 A. Akjouj and A. Mir, *Opt. Laser Technol.*, 2020, **130**, 106306.
- 313 N. Li, T. Tang, J. Li, L. Luo, C. Li, J. Shen and J. Yao, *J. Magn. Magn. Mater.*, 2019, **484**, 445–450.
- 314 T. Wenger, G. Viola, J. Kinaret, M. Fogelström and P. Tassin, *2D Mater.*, 2017, **4**, 025103.
- 315 Z. Sun, A. Martinez and F. Wang, *Nat. Photonics*, 2016, **10**, 227–238.
- 316 M. El barghouti, A. Akjouj and A. Mir, *Opt. Laser Technol.*, 2020, **130**, 106306.
- 317 B. Luan and M. A. Kuroda, *ACS Nano*, 2020, **14**, 13137–13145.
- 318 B. Luan and R. Zhou, *ACS Nano*, 2018, **12**, 3886–3891.
- 319 X. L. Fu, F. Hou, F. R. Liu, S. W. Ren, J. T. Cao and Y. M. Liu, *Biosens. Bioelectron.*, 2019, **129**, 72–78.
- 320 J. O. Tegenfeldt, C. Prinz, H. Cao, R. L. Huang, R. H. Austin, S. Y. Chou, E. C. Cox and J. C. Sturm, *Anal. Bioanal. Chem.*, 2004, **378**, 1678–1692.
- 321 S. L. Levy and H. G. Craighead, *Chem. Soc. Rev.*, 2010, **39**, 1133–1152.
- 322 Q. Xia, K. J. Morton, R. H. Austin and S. Y. Chou, *Nano Lett.*, 2008, **8**, 3830–3833.
- 323 B. Luan and A. Aksimentiev, *Phys. Rev. E: Stat., Nonlinear, Soft Matter Phys.*, 2008, **78**, 021912.
- 324 A. J. Storm, C. Storm, J. Chen, H. Zandbergen, J.-F. Joanny and C. Dekker, *Nano Lett.*, 2005, **5**, 1193–1197.
- 325 K. Liu, J. Feng, A. Kis and A. Radenovic, *ACS Nano*, 2014, **8**, 2504–2511.
- 326 A. P. Ivanov, E. Instuli, C. M. McGilvery, G. Baldwin, D. W. McComb, T. Albrecht and J. B. Edel, *Nano Lett.*, 2011, **11**, 279–285.
- 327 J. Lagerqvist, M. Zwolak and M. Di Ventra, *Nano Lett.*, 2006, **6**, 779–782.
- 328 P. Xie, Q. Xiong, Y. Fang, Q. Qing and C. M. Lieber, *Nat. Nanotechnol.*, 2012, **7**, 119–125.
- 329 M. E. Anderson, *Methods Enzymol.*, 1985, **113**, 548–555.
- 330 A. Meister and M. E. Anderson, *Annu. Rev. Biochem.*, 1983, **52**, 711–760.
- 331 (a) B. L. Sharma and R. K. Purohit, *Semiconductor heterojunctions*, Pergamon, 2015; (b) M. Karbalaee Akbari, Z. Hai, Z. Wei, R. K. Ramachandran, C. Detavernier, M. Patel, J. Kim, F. Verpoort, H. Lu and S. Zhuiykov, *J. Mater. Chem. C*, 2019, **7**, 5584–5595.
- 332 M. Yankowitz, J. Xue, D. Cormode, J. D. Sanchez-Yamagishi, K. Watanabe, T. Taniguchi, P. Jarillo-Herrero, P. Jacquod and B. J. LeRoy, *Nat. Phys.*, 2012, **8**, 382–386.
- 333 S. M. Sze and K. K. Ng, *Physics of semiconductor devices*, John Wiley & Sons, 2006.
- 334 N. Ubrig, E. Ponomarev, J. Zultak, D. Domaretskiy, V. Zólyomi, D. Terry, J. Howarth, I. Gutiérrez-Lezama, A. Zhukov and Z. R. Kudrynskiy, *Nat. Mater.*, 2020, **19**, 299–304.
- 335 W.-T. Hsu, Z.-A. Zhao, L.-J. Li, C.-H. Chen, M.-H. Chiu, P.-S. Chang, Y.-C. Chou and W.-H. Chang, *ACS Nano*, 2014, **8**, 2951–2958.
- 336 A. Li, Q. Chen, P. Wang, Y. Gan, T. Qi, P. Wang, F. Tang, J. Z. Wu, R. Chen and L. Zhang, *Adv. Mater.*, 2019, **31**, 1805656.

- 337 P. Wang, S. Liu, W. Luo, H. Fang, F. Gong, N. Guo, Z. G. Chen, J. Zou, Y. Huang and X. Zhou, *Adv. Mater.*, 2017, **29**, 1604439.
- 338 Z. Li, J. Dong, H. Zhang, Y. Zhang, H. Wang, X. Cui and Z. Wang, *Nanoscale Adv.*, 2021, **3**, 41–72.
- 339 X. Zong, H. Hu, G. Ouyang, J. Wang, R. Shi, L. Zhang, Q. Zeng, C. Zhu, S. Chen and C. Cheng, *Light: Sci. Appl.*, 2020, **9**, 114.
- 340 R. Cheng, F. Wang, L. Yin, Z. Wang, Y. Wen, T. A. Shifa and J. He, *Nat. Electron.*, 2018, **1**, 356–361.
- 341 M. Massicotte, P. Schmidt, F. Violla, K. G. Schadler, A. Reserbat-Plantey, K. Watanabe, T. Taniguchi, K. J. Tielrooij and F. H. Koppens, *Nat. Nanotechnol.*, 2016, **11**, 42–46.
- 342 X. Duan, C. Wang, J. C. Shaw, R. Cheng, Y. Chen, H. Li, X. Wu, Y. Tang, Q. Zhang and A. Pan, *Nat. Nanotechnol.*, 2014, **9**, 1024–1030.
- 343 M. Massicotte, P. Schmidt, F. Violla, K. Watanabe, T. Taniguchi, K.-J. Tielrooij and F. H. Koppens, *Nat. Commun.*, 2016, **7**, 1–7.
- 344 X. Zhou, N. Zhou, C. Li, H. Song, Q. Zhang, X. Hu, L. Gan, H. Li, J. Lü and J. Luo, *2D Mater.*, 2017, **4**, 025048.
- 345 Q. A. Vu, J. H. Lee, V. L. Nguyen, Y. S. Shin, S. C. Lim, K. Lee, J. Heo, S. Park, K. Kim and Y. H. Lee, *Nano Lett.*, 2017, **17**, 453–459.
- 346 H. Li, L. Ye and J. Xu, *ACS Photonics*, 2017, **4**, 823–829.
- 347 M. Long, E. Liu, P. Wang, A. Gao, H. Xia, W. Luo, B. Wang, J. Zeng, Y. Fu and K. Xu, *Nano Lett.*, 2016, **16**, 2254–2259.
- 348 Y. Wen, L. Yin, P. He, Z. Wang, X. Zhang, Q. Wang, T. A. Shifa, K. Xu, F. Wang, X. Zhan, F. Wang, C. Jiang and J. He, *Nano Lett.*, 2016, **16**, 6437–6444.
- 349 Y. Deng, Z. Luo, N. J. Conrad, H. Liu, Y. Gong, S. Najmaei, P. M. Ajayan, J. Lou, X. Xu and P. D. Ye, *ACS Nano*, 2014, **8**, 8292–8299.
- 350 C.-H. Lee, G.-H. Lee, A. M. Van Der Zande, W. Chen, Y. Li, M. Han, X. Cui, G. Arefe, C. Nuckolls, T. F. Heinz, J. Guo, J. Hone and P. Kim, *Nat. Nanotechnol.*, 2014, **9**, 676–681.
- 351 M. M. Furchi, A. Pospischil, F. Libisch, J. Burgdörfer and T. Mueller, *Nano Lett.*, 2014, **14**, 4785–4791.
- 352 W. J. Yu, Y. Liu, H. Zhou, A. Yin, Z. Li, Y. Huang and X. Duan, *Nat. Nanotechnol.*, 2013, **8**, 952–958.
- 353 C.-C. Chen, Z. Li, L. Shi and S. B. Cronin, *Nano Res.*, 2015, **8**, 666–672.
- 354 Y. Li, Z. Li, C. Chi, H. Shan, L. Zheng and Z. Fang, *Adv. Sci.*, 2017, **4**, 1600430.
- 355 V. K. Sangwan and M. C. Hersam, *Nat. Nanotechnol.*, 2020, **15**, 517–528.
- 356 S. Seo, J.-J. Lee, H.-J. Lee, H. W. Lee, S. Oh, J. J. Lee, K. Heo and J.-H. Park, *ACS Appl. Electron. Mater.*, 2020, **2**, 371–388.
- 357 X. Yin, Y. Wang, T.-H. Chang, P. Zhang, J. Li, P. Xue, Y. Long, J. L. Shohet, P. M. Voyles, Z. Ma and X. Wang, *Adv. Mater.*, 2020, **32**, 2000801.
- 358 M. Velický and P. S. Toth, *Appl. Mater. Today*, 2017, **8**, 68–103.
- 359 M. Wang, S. Cai, C. Pan, C. Wang, X. Lian, Y. Zhuo, K. Xu, T. Cao, X. Pan, B. Wang, S.-J. Liang, J. J. Yang, P. Wang and F. Miao, *Nat. Electron.*, 2018, **1**, 130–136.
- 360 Q. A. Vu, Y. S. Shin, Y. R. Kim, V. L. Nguyen, W. T. Kang, H. Kim, D. H. Luong, I. M. Lee, K. Lee, D.-S. Ko, J. Heo, S. Park, Y. H. Lee and W. J. Yu, *Nat. Commun.*, 2016, **7**, 12725.
- 361 L. Sun, Y. Zhang, G. Han, G. Hwang, J. Jiang, B. Joo, K. Watanabe, T. Taniguchi, Y.-M. Kim, W. J. Yu, B.-S. Kong, R. Zhao and H. Yang, *Nat. Commun.*, 2019, **10**, 3161.
- 362 C. Liu, H. Chen, S. Wang, Q. Liu, Y.-G. Jiang, D. W. Zhang, M. Liu and P. Zhou, *Nat. Nanotechnol.*, 2020, **15**, 545–557.
- 363 C. He, J. Tang, D.-S. Shang, J. Tang, Y. Xi, S. Wang, N. Li, Q. Zhang, J.-K. Lu, Z. Wei, Q. Wang, C. Shen, J. Li, S. Shen, J. Shen, R. Yang, D. Shi, H. Wu, S. Wang and G. Zhang, *ACS Appl. Mater. Interfaces*, 2020, **12**, 11945–11954.
- 364 A. H. Castro Neto, F. Guinea, N. M. R. Peres, K. S. Novoselov and A. K. Geim, *Rev. Mod. Phys.*, 2009, **81**, 109–162.
- 365 H. Tian, X. Cao, Y. Xie, X. Yan, A. Kostelec, D. DiMarzio, C. Chang, L.-D. Zhao, W. Wu, J. Tice, J. J. Cha, J. Guo and H. Wang, *ACS Nano*, 2017, **11**, 7156–7163.
- 366 G. Cao, P. Meng, J. Chen, H. Liu, R. Bian, C. Zhu, F. Liu and Z. Liu, *Adv. Funct. Mater.*, 2020, **31**, 2005443.
- 367 X. Feng, X. Liu and K.-W. Ang, *Nanophotonics*, 2020, **9**, 1579–1599.
- 368 D. Xiang, T. Liu, J. Xu, J. Y. Tan, Z. Hu, B. Lei, Y. Zheng, J. Wu, A. H. C. Neto, L. Liu and W. Chen, *Nat. Commun.*, 2018, **9**, 2966.
- 369 S. Seo, S.-H. Jo, S. Kim, J. Shim, S. Oh, J.-H. Kim, K. Heo, J.-W. Choi, C. Choi, S. Oh, D. Kuzum, H. S. P. Wong and J.-H. Park, *Nat. Commun.*, 2018, **9**, 5106.
- 370 S. Wang, C. Chen, Z. Yu, Y. He, X. Chen, Q. Wan, Y. Shi, D. W. Zhang, H. Zhou, X. Wang and P. Zhou, *Adv. Mater.*, 2019, **31**, 1806227.
- 371 H. Xu, M. Karbalaee Akbari, F. Verpoort and S. Zhuiykov, *Nanoscale*, 2020, **12**, 20177–20188.
- 372 K. Nozaki, T. Tanabe, A. Shinya, S. Matsuo, T. Sato, H. Taniyama and M. Notomi, *Nat. Photonics*, 2010, **4**, 477–483.
- 373 D. N. Basov and M. M. Fogler, *Nat. Nanotechnol.*, 2017, **12**, 187–188.
- 374 J. He, N. Kumar, M. Z. Bellus, H.-Y. Chiu, D. He, Y. Wang and H. Zhao, *Nat. Commun.*, 2014, **5**, 5622.
- 375 X. Guo, R. Liu, D. Hu, H. Hu, Z. Wei, R. Wang, Y. Dai, Y. Cheng, K. Chen, K. Liu, G. Zhang, X. Zhu, Z. Sun, X. Yang and Q. Dai, *Adv. Mater.*, 2020, **32**, 1907105.